Improvement of the Neutron Emission Ratio Observer by an Active Cosmic Ray Shield

Clemens Herlitzius

2008

Contents

Chapter 1

Introduction and Background

1.1 Motivation - Astrophysics and the Origin of Nuclei

An important astrophysical question is how to explain the abundances of the nuclei in the Universe. The abundance of elements has been measured in different ways. Observations can be done on meteorites, cosmic rays, interstellar gas or dust, by spectroscopy of stellar objects (our sun) or by earth crust samples to mention some methods. Of course, earth crust samples have been influenced by chemical and geological effects for about 4.5 billion years. Because of the volatility of He, the noble gas is under abundant on the earth. Effects like that adulterate the relative abundance and have to be considered when abundances of different sources are compared.

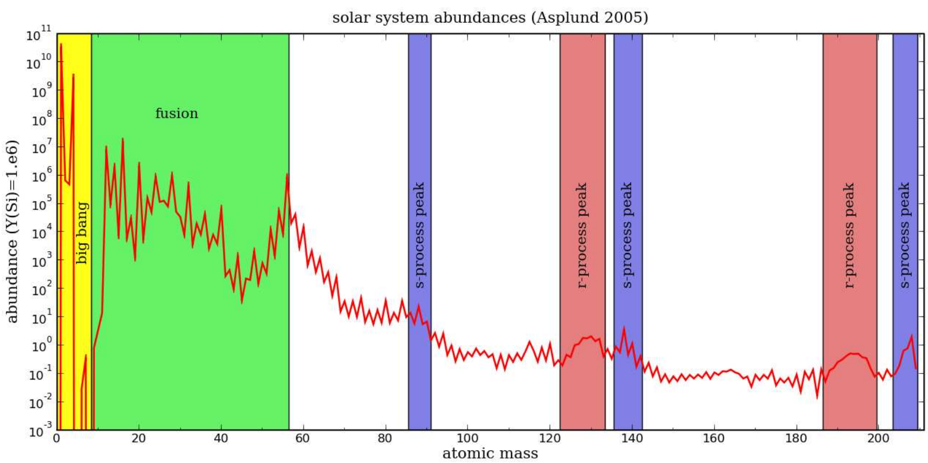

Figure 1.1: Isotopic abundance in solar system as a function of atomic mass. Normalized to 10^6 for ^{28}Si [Asp05].

Roughly 96-99% of all matter in the Universe are hydrogen and helium.

Pronounced maxima in the abundance curve can be observed for H, He and Fe. A gap between He and C shows that Li, Be and B are suppressed because no stable nuclei exist for $A = 5$ and $A = 8$. He and few Li is produced in the first minutes after Big Bang by collisions of protons with protons or heavier nuclei.

The nuclear shell model explains the structure of nuclei with shells similar to the electron shell model. In nuclear physics shells are filled with nucleons and reach a high grade of stability, when shells are closed. So called magic numbers mark the numbers of neutrons and protons for closed shells. Magic numbers of protons or neutrons are 2, 8, 20, 28, 50, 82, 126.

The smaller double-peak structure above the Fe peak in figure 1.1, which is close to magic numbers can be explained by neutron capture processes (see sub chapter 1.3 - r-/s-process), where high relative abundances at closed shells are produced. After the neutron flux stops, radioactive nuclei decay to the valley of stability. If the nuclei have been close to the valley of stability anyway (s-process), the shift of abundance to lighter nuclei is smaller and a peak very close to a magic number is the result. If the nuclei are far away from the valley of stability on the very neutron rich side (r-process), the shift of abundance is larger and the second peak on the left of the s-process peak is the result.

In astrophysics, elements heavier than He are often called metals and are most likely produced in stellar evolutionary processes. Starting with hydrogen, stars can produce elements up to iron in the different burning phases. All other elements are produced in capture processes like the r-/s-process or the p-process (see sub chapter 1.3 - r-/s-process). Conditions for n-/p-capture processes can be found for example in supernovae or explosive shell burning. Not all produced nuclei are stable, which means, that we observe an equilibrium of all processes which produce or reduce the abundance of a special nucleus.

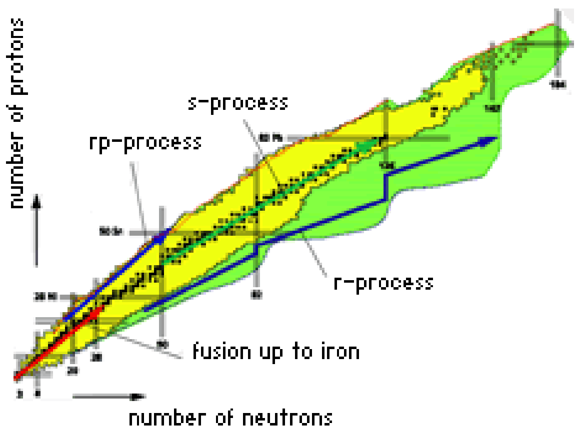

Figure 1.2: Schematic band of nuclides [Gsi08]

The colored band in figure 1.2 shows schematically the existing nuclei. Different regions of unstable nuclei take an important place in the production of heavy nuclei with $A > 60$.

1.2 Big Bang and Stellar Nucleosynthesis

Big Bang and early Universe

With the awareness of an isotropic expansion of the Universe, the isotropic CMBR (cosmic microwave background radiation), the CMB fluctuation, the ratio of baryons to photons and the abundance of nuclei, the idea of a big bang is established [Rol88]. The evolution of the Universe after the Big Bang begins with high densities, high temperatures and a perfect symmetry of matter to antimatter. With expansion, the density and temperatures decrease and symmetries are broken during phase transitions. Hadrons are composed of quarks after $10^{-6}s$ and neutrinos decouple after $1s$ which accrues the neutrino background radiation. Primordial nucleosynthesis begins in the same time range and light nuclei (^2H, ^3He, ^4He, ^7Li) are produced in the following minutes. The Universe becomes transparent for γs after $10^{12}s$, when electrons recombine with nuclides to atoms and and energy of γs is too low for a dominant interaction with particles. The decoupled γs are observed today as the CMBR. The γ energy decreases with time, because the wavelength increases with the accelerated expansion of the Universe.

This model of the early Universe and Big Bang nucleosynthesis explains the huge abundances of hydrogen and helium in the Universe. All heavier elements are produced in processes in different stages of a star's life and are found in much less amounts than hydrogen or helium.

Stellar nucleosynthesis

Even though, the Universe is relatively homogeneous and isotropic, gravity forms some structure. Particles form dust clouds, dust clouds form objects and more and more matter accumulates to heavier objects. The Jeans instability tells us, with which amount of mass a mass accumulation becomes stable. With increasing mass, matter is more and more contracted and pressure and temperature increase in the middle of the accumulation. If the mass is high enough, a star is born.

Thermonuclear fusion of hydrogen starts, when temperature is high enough to provide energy to particles to overcome the Coulomb barrier of nuclei. This is why heavier nuclei can only fuse at higher temperatures / pressures. High temperatures can only be reached by gravitational energy. That means that high temperature is related to high pressure, generated by huge masses. The minimal mass to ignite hydrogen burning is about $0.6\ M_{\mathrm{sun}}$, which corresponds to $T \approx 10^7 K$ in the core. The exothermic reactions create pressure, which balance the gravitational attraction. An equilibrium is established. When hydrogen fuel is exhausted, fusion and energy release stop, gravitational attraction exceeds and the star contracts. Pressure in the core increases until temperature is high enough to trigger the next burning phase. In this case helium burning. Again, exothermic reactions create pressure, that balances the gravitational attraction and a new equilibrium is established until helium is exhausted. Nucleosynthesis continues with fusion of heavier nuclei, if the star's mass is high enough to cause a contraction that increases the core temperature and to trigger the next burning phase [Rol88].

The released energy by fusion from hydrogen up to iron is approx. $8.8\,\frac{MeV}{nucleon}$, where more than 80% of this energy is released in fusion from H to He [Tay66]. Nucleosynthesis via fusion reactions cannot produce elements heavier than iron, because the binding energy is maximum in Fe-region and fusion reactions become endothermic for heavier elements.

H-Burning: $(T = 2 \cdot 10^7 K,\ M > 0{,}6 M_{sun})$ Since hydrogen burning is the longest period in a star's life, most observable stars are in the hydrogen burning phase. The released energy in hydrogen burning is the largest amount per nucleon in stellar nucleosynthesis. Basically the reaction for H fusion is $4p \rightarrow {}^4He + 2e^+ + 2\nu_e$. The probability for this reaction is very low, but a chain of reactions (three pp chains) produces the same result with higher probability.

$p + p \rightarrow d + e^+ + \nu_e$

$d + p \rightarrow^3 He + \gamma$

86%: ${}^3He +^3 He \rightarrow {}^4He + p + p$ (26.2 MeV)

14%: ${}^3He +^4 He \rightarrow {}^7Be + \gamma$

${}^7Be + e^- \rightarrow {}^7Li + \nu_e$

${}^7Li + p \rightarrow {}^4He + {}^4He$ (25.57MeV)

${}^7Be + p \rightarrow^8 B + \gamma$

${}^8B \rightarrow^8 Be + e^+ + \nu_e$

${}^8Be \rightarrow^4 He +^4 He$ (19.20MeV)

If the star is a so called population II star, it contains metals from elapsed cycles of former stars. In this case, metals can serve as catalysts and the so called CNO cycle (figure 1.3) can occur [Bah03].

Beyond the CNO cycle, consecutive cycles can produce also heavier nuclides. Because of the increasing Coulomb barrier, the temperature must be higher to provide enough energy. During hydrogen burning, most mass is necessary to provide the energy by gravitation to overcome the Coulomb barrier. Only 2.4% of the mass of hydrogen actually fuse to helium during the first burning phase.

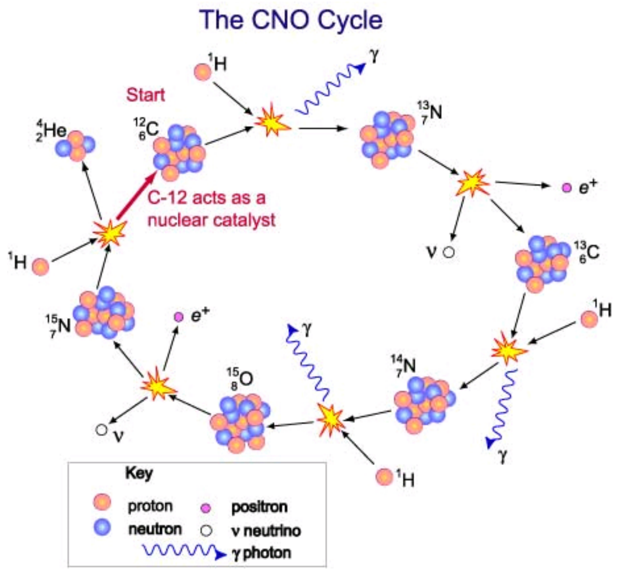

Figure 1.3: CNO cycle [Atn08]

He-Burning: **($T = 2 \cdot 10^8 K$, $M > 0.5 M_{sun}$)** After hydrogen burning, the next step would be the fusion to Li, Be or B, but the product isotopes, which can be created by two body reactions of He and H are short-lived. Therefore they decay too fast after fusion – even before the next possible burning phase. A solution to this problem would be a three particle reaction $3 \cdot ^4 He \rightarrow ^{12} C$, but the probability of a three particle reaction to occur is low. The sequence of two collisions and reactions is much more probable.

"triple-alpha reaction / Saltpeter reaction"

$\alpha + \alpha \leftrightarrow ^8 Be \; (t_{1/2} = 2.6 \cdot 10^{-16} s)$

$^8Be + \alpha \rightarrow ^{12} C + \gamma$

Generally, the first reaction has a small cross section, but it has a 0^+ resonance in the temperature range of effective helium burning. The life-time of ^8Be is short, but compared to the time for the next ^4He collision still long enough. An equilibrium between one ^8Be and two ^4He is established with a ratio of $\frac{^8Be}{^4He} \approx 10^{-9}$. But still, this small ratio provides enough ^8Be nuclei for the next step $^8Be + \alpha \rightarrow ^{12} C + \gamma$. Only, because of the so-called Hoyle resonance [Hoy53] at the requested energy, the reaction produces sufficient amounts of ^{12}C. Additional α- capture reactions, starting from ^{12}C create the isotopes ^{16}O and ^{20}Ne.

$$^{12}C + ^4 He \rightarrow ^{16} O \; , \; ^{16}O + ^4 He \rightarrow ^{20} Ne$$

^{16}O and ^{20}Ne are relatively abundant in the Universe and are created in stars with $2 < \frac{M}{M_{sun}} < 8$.

C-Burning: **($T = 6 \cdot 10^8 K$, $M > 5M_{sun}$)** For masses $M > 5M_{sun}$, additional burning phases are possible. If a star's mass is $M > 8M_{sun}$, all possible phases will be passed.

Different reactions in carbon burning have different possibilities.

$$
\begin{aligned}
&^{12}C +^{12} C \rightarrow^{24} Mg + \gamma \\
&^{12}C +^{12} C \rightarrow^{20} Ne + \alpha \\
&^{12}C +^{12} C \rightarrow^{23} Na + p \\
&^{12}C +^{12} C \rightarrow^{23} Mg + n
\end{aligned}
$$

The Q-value of the first reaction is the highest, but the probability is very small. The following two reactions occur more likely and are the main processes in C-burning. The emitted alphas and protons are captured instantly. The following reaction sequence is very important for astrophysics.

$$^{12}C(p,\gamma)^{13}N \rightarrow^{13} C + \beta^+ \rightarrow^{13} C(\alpha,n)^{16}O$$

The $^{13}C(\alpha,n)^{16}O$ is one of the main sources for free neutrons, which becomes interesting for the later n-capture processes discussed in 1.3 - r-/s-process.

O-Burning: With temperatures of about $(1.5-2) \cdot 10^9 K$, the oxygen burning starts and $^{16}O +^{16} O \rightarrow ...$ reactions become dominant. Similar to carbon burning, there are many reaction channels, but reactions with p and $2p$ production are most likely. The reactions $^{16}O +^{16} O \rightarrow^{31} P + p$ and $^{16}O +^{16} O \rightarrow^{30} Si + 2p$ occur to approx. 70%, reactions with α-production to 20%.

Ne-/Si-Burning: For later burning phases, the change from one to the next burning stage is less clearly distinguishable. Basically, neon burning is part of the silicon burning. The equilibrium of the reaction $^{20}Ne+\gamma \leftrightarrow^{16} O+\alpha$ is determined by temperature. With $T \approx 1.3 \cdot 10^9 K$, photo disintegration becomes more efficient and the α-production dominates. On the other hand, those αs are captured by silicon and heavier nuclei, and fusion continues up to Ni/Fe. During silicon burning, temperatures of $T > 3 \cdot 10^9 K$ favor the photo disintegration and additional αs are provided for capture during silicon burning. $^{28}Si+^{28}Si \rightarrow ...$ is improbable because of the high Coulomb barrier.

α-production by photo disintegration:

$$^{28}Si(\gamma,\alpha)^{24}Mg(\gamma,\alpha)^{20}Ne(\gamma,\alpha)^{16}O(\gamma,\alpha)^{12}C(\gamma,\alpha)2\alpha$$

fusion by α-capture:

$$^{28}Si(\alpha,\gamma)^{32}S(\alpha,\gamma)^{36}Ar(\alpha,\gamma)^{40}Ca(\alpha,\gamma)^{44}Ti(\alpha,\gamma)^{48}Cr(\alpha,\gamma)^{52}Fe(\alpha,\gamma)^{56}Ni$$

Fusion continues as long as the reactions are exothermic. The binding energy per nucleon has a maximum in the Fe region. Because of that, stellar fusion can only produce elements up this region. The energy released by fusion in the interior of a star prevents the collapse because of gravitational attraction. Heavier elements than Fe/Ni can only be produced by endothermic fusions. This fact and the increasing Coulomb barrier stop the stellar burning process in the Fe region and the equilibrium between gravitational attraction and pressure created by exothermically fusion collapses.

At the beginning of a star's life, the burning phases start one after another. If a star is heavy enough, it contracts and triggers the next burning stage, after the previous one is exhausted and cannot balance the equilibrium between gravitational attraction and pressure, created by exothermic fusion, anymore. Since the local temperature decreases with increasing radius of the star, outer regions provide less energy but still can burn nuclei, where fusion occurs with less temperature. Because of this effect, outer regions still produce heavier nuclei, which move to subjacent shells and fuse, until they reach the Fe/Ni core.

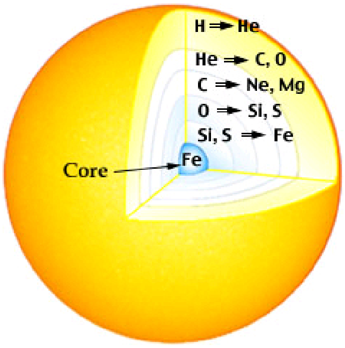

Figure 1.4: Shell burning [Sol08]

After carbon burning, the different burning phases are not clearly distinguishable anymore. A lot of reactions run parallel and compete with each other. The illustrated reactions are just the main reactions, but much more reactions and effects have influence on the stellar nucleosynthesis. [Rol88, Kra06, Wei04]

1.3 Nucleosynthesis of elements with $A > 60$

Elements with $A < 60$ are produced by charged-particle fusion. Elements with $A > 60$ cannot be produced by fusion with charged particles in an efficient way. Because for Fe/Ni the binding energy per nucleon has a maximum, fusion reactions for $A > 60$ are endothermic and in addition to that, the Coulomb barrier increases with each added proton. Heavier elements are mainly produced by slow neutron capture (s-process) and rapid neutron capture (r-process). Photo disintegration and proton capture processes are important for creation of some specific isotopes like molybdenum [Cow91]. Since theory and observation do not agree in a satisfying way, this field is active. Models are improved and modified and also more local processes are considered.

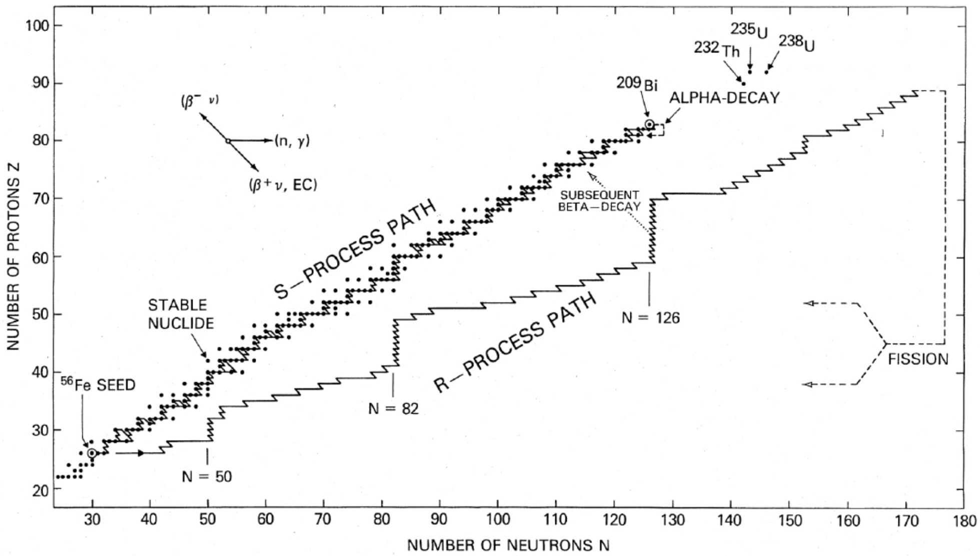

Figure 1.5: Table of nuclei with processes, which are responsible for the formation of heavy elements: paths of the r-/s-processes [Rol88]

Since all processes are based on reactions of nuclear physics, properties of nuclei are essential inputs. Half-life, mass, reaction rates, excited states, cross sections and resonances in reactions can be provided by experiments in nuclear physics.

1.3.1 Slow neutron-capture process (s-process)

Because neutrons have no charge and do not see a Coulomb barrier, neutron capture dominates the production of heavy nuclei. The neutron capture creates nuclei in the table of isotopes on the neutron rich side of valley of stability. If the average time for a neutron capture takes longer than the β decay time, we talk about the slow neutron-capture (s-process):

$$\tau_{n-capture} > \tau_{\beta-decay}$$

This time relation is the reason, why the s- process path is close to the valley of stability. During the process, the relation $\sigma \cdot N = const$ is true for the path of the main s-process, where N is the abundance of the nucleus and σ is the neutron capture cross section. Basically, a sequence of neutron captures and subsequent β decays defines the s-process path close to the valley of stability.

$$(Z, A) \xrightarrow{n} (Z, A+1) \xrightarrow{\beta} (Z+1, A+1) \xrightarrow{n} ...$$

$\tau_{n-capture}$ is inversely proportional to the neutron density and the neutron capture cross section.

In reactions produced neutrons have a lot of kinetic energy and increase their cross section by moderation in stellar plasma. When neutron capture and β decay have similar time scales, the path in the table of isotopes splits and a so called branching point is the result. Those branching points can gain access to stellar conditions at this point like temperature or neutron density.

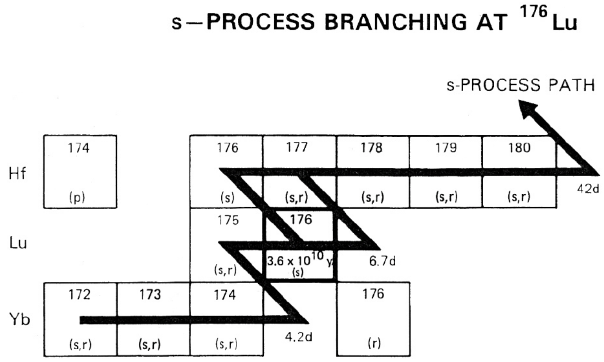

Figure 1.6: s-Process branching at ^{176}Lu [Rol88]

The neutron-capture cross sections of the nuclei influence their abundances significantly. If a nuclide has a relatively small neutron-capture cross section, the abundance of the daughter products will be higher than of a nuclide with relatively large cross section. As long as the neutron flux is available, the s-process can produce heavy nuclides. At nuclei with large n-capture cross sections, the waiting for a neutron-capture will be short and the abundance of daughter products after freeze out will be small. Nuclei with smaller n-capture cross sections have to wait longer for neutron capture, as long as the nuclide is stable enough. The s-process abundances are inversely proportional to the cross sections of mother s-process nuclei.

The phenomenological idea of the s-process is advanced, when one distinguishes between the weak component of the s-process and the main (strong) component. These components occur under different conditions. The weak component creates elements with $A \leqq 90$ and occurs in stars with $M > 15 M_{sun}$ in the He-burning and C-burning. In this environment, temperature is about $(1.8 - 3) \cdot 10^8 K$ and the reaction $^{22}Ne(\alpha, n)^{25}Mg$ releases neutrons and provides a neutron density of $n_n = (0.8 - 1.9) \cdot 10^8 \frac{1}{cm^3}$ [Kap89, Gal98].

The main (strong) component creates elements with $A \geq 90$ and gets the necessary neutron density by the reactions $^{13}C(\alpha, n)^{16}O$ and $^{22}Ne(\alpha, n)^{25}Mg$,

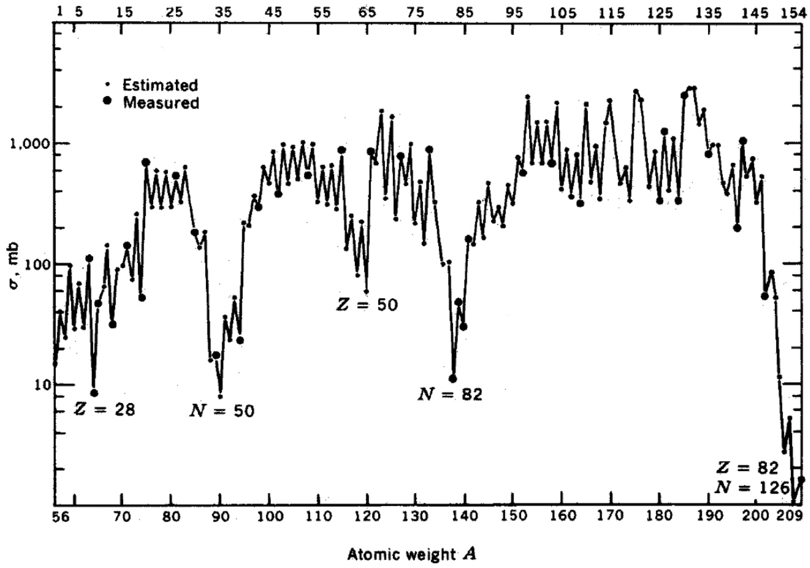

Figure 1.7: Measured and estimated neutron cross section as a function of mass of nuclei with a neutron energy of 25keV [Wei04].

where the second reaction provides only a small fraction of the neutron density at temperatures of $2.7 \cdot 10^8 K$ and is exhausted after few years. The first reaction provides a neutron density of $7 \cdot 10^7 \frac{1}{cm^3}$ for about 20000 years at $T = 9 \cdot 10^7 K$. The main component occurs during helium shell burning in low mass stars and in asymptotic giant stars.

After the neutron flux has stopped, nuclei decay by β emission to nuclei closer to the valley of stability until they reach a stable isobar. Since the path of the s-process is close to the valley of stability anyway, peaks are created close to the waiting points of neutron shells, where abundances during s-process are higher because of smaller n-capture cross sections (see figure 1.1).

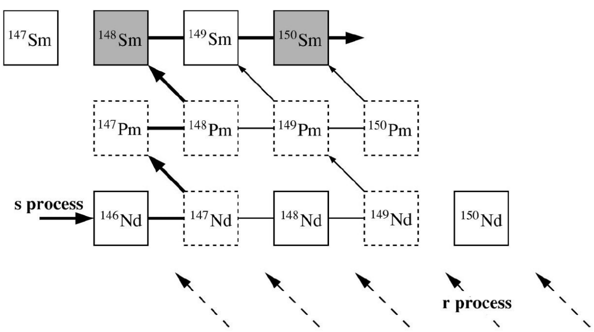

Figure 1.8: s-process branchings in the Nd-Pm-Sm region. Some elements can only be produced by s-process, because they are shielded by stable nuclei against r-process [Kap89].

1.3.2 Rapid neutron-capture process (r-process)

More than 50% of the elements heavier than iron are created by the r-process. Here, the neutron capture occurs faster than the β decay and the main r-process path is on the very neutron rich side far away from the valley of stability.

$$\tau_{n-capture} \ll \tau_{\beta-decay}$$

The historical r-process starts with seed nuclei in the iron region [Bur57]. A high neutron flux and a density of $10^{20}\frac{1}{cm^3} < n_n < 10^{30}\frac{1}{cm^3}$ result in neutron captures by the seed nuclei. Nuclei become more and more neutron rich, until photo disintegration (γ, n) and neutron capture (n, γ) establish an equilibrium and fix the r-process path on the very neutron-rich side of stability. The neutron separation energy is $S_n \approx (2-3)MeV$ for the most neutron rich nuclei in the r-process [Kra93, Cow91]. No more neutrons can be captured, before a neutron is separated by photo disintegration. The nucleus has to wait for a β decay, before more neutrons can be absorbed. With the β decay, the $\frac{neutron}{proton}$ ratio becomes smaller and the nucleus gets closer to stability. Because S_n is larger for nuclei closer to stability, the photo disintegration rate decreases and the neutron capture rate is higher. The rapid n-capture process continues up to the next equilibrium between photo disintegration and n-capture. These important points are called "waiting points" because the nucleus has to wait for a single β decay, before additional neutrons can be captured. A single β decay increases the atomic number by one and the number of nucleons is kept constant. After that, a neutron can be captured and the nucleon number is increased by one. When numbers of neutrons and/or protons reach "magic numbers" the closed shell configuration decreases the neutron capture cross section of the nucleus. At waiting points, which are related to closed shells, the sequence of a single β-decay and a single neutron capture is repeated, until neutrons for the next shell can be captured. In this ladder path, nuclei closer to the valley of stability are produced. By decreasing the neutron to proton ratio, the n-capture cross section becomes larger. The β half-life increases for nuclei closer to valley of stability. Because of the increasing neutron capture cross section closer to the valley of stability, there is a point, when multiple neutrons can be captured again and the next nuclear shell is filled with neutrons up to the (n, γ) - (γ, n) equilibrium (see figure 1.5). The waiting points at the magic shells cause the bottlenecks of the r-process.

Simplified, the abundance of a nucleus after freeze out is proportional to the β half-life of its mother nucleus in the r-process path. Primarily because of the bottlenecks, there is a minimum duration time of the r-process to build nuclei up to $A \approx 200$. Most of the nuclei in the r-process can be found at waiting points. The path between two waiting points can be passed quickly, because β half-lives are short far away from stability.

When the neutron flux stops, no more neutrons can be captured and the unstable nuclei start decay to the valley of stability by beta decay until stability is reached. During the r-process, nuclei at magic shells are very abundant. After freeze-out, abundances of isotopes are shifted by β decay to isotopes with higher atomic numbers and lower numbers of neutrons. The result is a peak left of the s-process peaks and magic numbers. The shift compared to the s-process peak can be explained with the more neutron rich path of the r-process compared to the s-process.

Neutron capture processes can also work for lighter elements than iron, but are dominant for the production of heavy elements with $A > 60$.

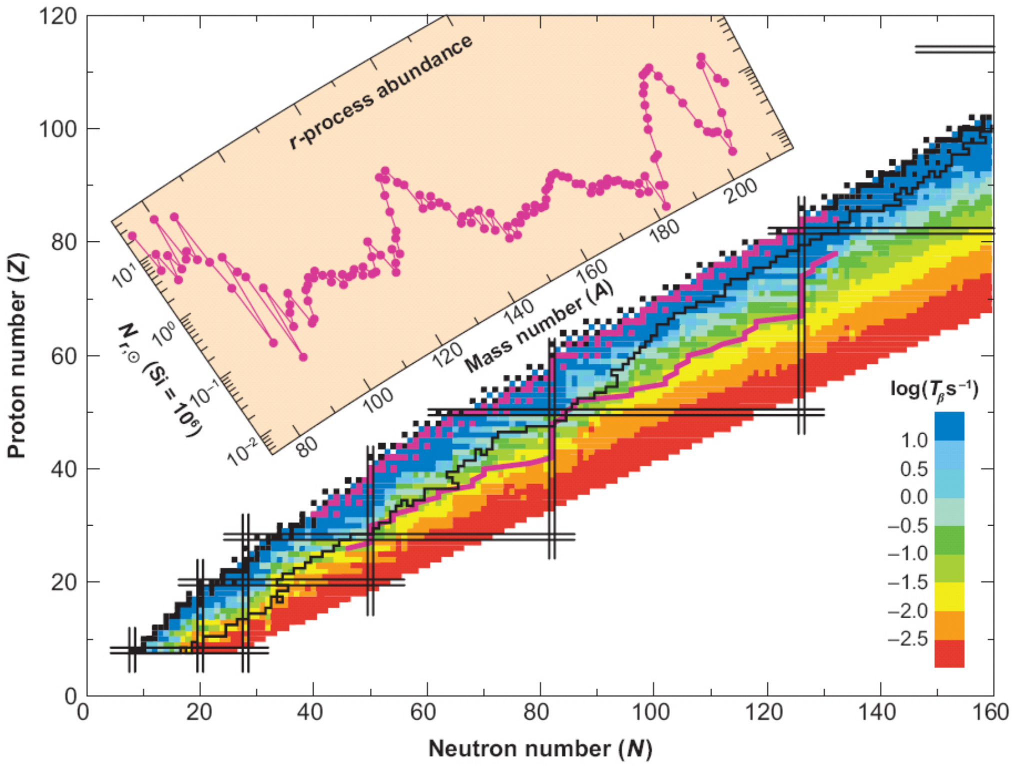

Figure 1.9: Relation of waiting points and solar abundances [Sne08].

Mandatory conditions of temperature and neutron density are provided for example in supernovae and neutron star mergers. Temperatures of about $T \approx (0.5-3) \cdot 10^9 K$ and neutron densities $n_n > 10^{20} \frac{1}{cm^3}$ are necessary for the rapid neutron-capture process. Not all r-process nuclei can be produced under the same conditions. The r-process is a dynamic process and the environment (temperature, n-density) define the path of nuclei in the r-process. The idea of the r-process is widely accepted, but a lot of details are still unknown and are part of present research. For example, the neutrino-driven wind seems to have an influence to the r-process [Woo94]. For models, experimental data like masses, neutron-capture cross sections, β half-lives and P_n-values are required.

The more experimental data are available, the better models can be improved. Since conditions in reality of r-/s-processes are different to conditions, which can be provided in experiments, it can be difficult to measure properties of specific nuclei. Anyway, properties of nuclei can be inferred by indirect measurements and data can be corrected to conditions during processes.

There is a limit for the production of heavy nuclei by neutron capture, because for $A > 200$, neutron induced fissions occur more and more likely.

Other processes than the r-/s-process also contribute to the production of heavy nuclei. Here, the p-process and the rp-process should be mentioned [Arn03, Sch98]. More detailed description of processes in nucleosynthesis can be found in references [Rol88, Kra06].

1.4 Beta- delayed neutron emission

As described in sub chapter 1.3, β decay is important for n-capture processes. Not only the s-/r-process are distinguished by the β half-life compared to neutron capture rate. During the processes, β half-lives define the path of nuclei within the process. Besides neutron flux, β half-lives influence the abundances of nuclei during the capture process and after freeze out. Together with β decay, the effect of β-delayed neutron emission changes the decay paths of nuclei and hereby the final abundances.

β decay properties of very neutron-rich nuclei can be specified by the measurements of β half-lives and delayed neutron emission probabilities (P_n-values). In the case of β-delayed neutron emission, the β-decay daughter nucleus is created in an excited state. The de-excitation to the ground state can be done in one or multiple γ emissions or – if the excitation energy is higher than the neutron separation energy S_n – by neutron emission, also followed by γ emissions to the ground state of the final nucleus.

Figure 1.10 shows the β-delayed neutron emission by the example of ^{93}Rb. The precursor (^{93}Rb) creates the emitter (^{93}Sr) by β decay. Depending on the excited state of the emitter, neutron emission and γ-de-excitation compete. Neutron emission creates the (excited) final nucleus ^{92}Sr. γ emission de-excite the emitter to the ground state. The following β decays to ^{93}Y or ^{92}Y are are not important for the explanation of the β-delayed neutron emission [Kra82].

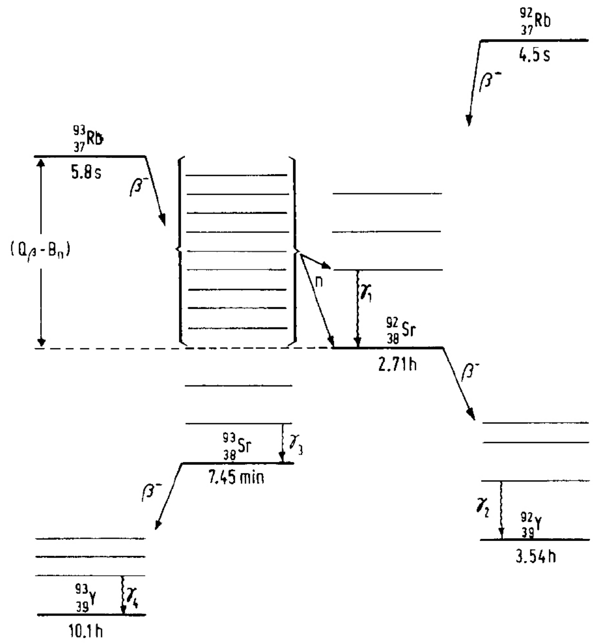

Figure 1.10: Principle characteristics of the β-delayed neutron emission process by the example of ^{93}Rb decay. Schematically, the β decay of the precursor (^{93}Rb) to the neutron-unbound states in the emitter (^{93}Sr) is shown. ^{93}Sr emits a neutron and the so called "final nucleus" (^{92}Sr) is created. The final nucleus decays by β-emission to ^{92}Y. In competition to the neutron emission, the emitter also can reach its own ground state by γ-emission. After that, the β-decay to ^{93}Y is shown. [Kra82].

The interrelation between β half-life and neutron emission probability with the β−strength function $S_\beta(E_i)$ is given schematically in [Kra84].

$$\frac{1}{T_{1/2}} = \sum_{E_i \geq 0}^{E_i \leq Q_\beta} S_\beta(E_i) \cdot f(Z, Q_\beta - E_i)$$

Q_β is the total β−decay energy (equivalent to the mass difference of mother and daughter nucleus and the emitted electron) and $f(Z, Q_\beta - E_i)$ is the Fermi function. E_i describes the energy states of the daughter states, relative to the ground state and runs in discrete steps from 0 to Q_β.

The β−delayed neutron emission probability can be described by

$$P_n = \frac{\sum_{B_n}^{Q_\beta} S_\beta(E_i) \cdot f(Z, Q_\beta - E_i)}{\sum_0^{Q_\beta} S_\beta(E_i) \cdot f(Z, Q_\beta - E_i)}$$

Since $f \propto (Q_\beta - E_i)^5$, $T_{1/2}$ is dominated by low energy resonances in $S_\beta(E_i)$ like energy levels close to the ground state. Gamow Teller or first-forbidden transitions are the most common channels for β decay. The β-delayed neutron emission probability P_n is the ratio of the integral of the β strength for states above the neutron separation energy, to all possible states in the β-decay daughter. In this model, it is assumed, that all excitations from states $E_i > B_n$ de-excite by neutron emission and γ-de-excitation from states above B_n are neglected. For a given Q_β-value, small P_n values usually correlate with short β half-lives and large P_n values correlate with long β half-lives. This is a trend, which can be used to check experimental data [Kra84].

More detailed models can be separated in two groups.

1. Physical quantities are provided by a polynomial or an algebraic expression. Empirical formulas describe the macro system and provide physical quantities. No one-particle description is possible, because average properties of β−decay are used.

2. Effective nuclear interactions are described microscopically and solved by quantum- mechanical Schrödinger or Dirac equation.

Representative for the first group of models, we take a look to the "Kratz-Hermann Formula" [Pfe01]. There are further improved formula, but this one highlights the basic idea of group 1 models. It provides a simple phenomenological expression for P_n values:

$$P_n \approx a \left(\frac{Q_\beta - S_n}{Q_\beta - C} \right)^b$$

a and b are free parameters, which can be determined by a fit of experimental data. C is the "cut-off" parameter and corresponds to the pairing-gap energy (according even/odd character of the β-decay daughter, which is the neutron emitter). The parameters a and b are determined from experimental fits, like shown in figure 1.11 for different ranges of mass.

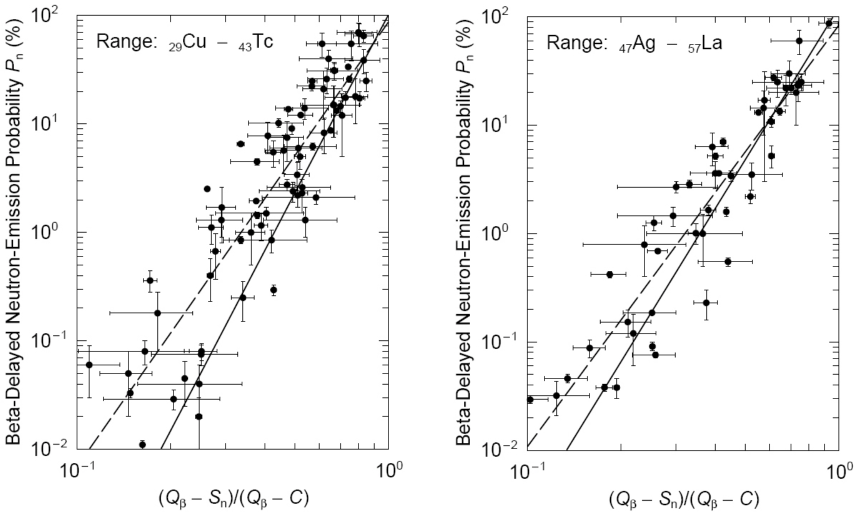

Figure 1.11: Parameter fit of experimental data [Pfe01]

P_n-values can be determined in experiments. Basically, the combination of a β counter and a neutron counter is sufficient to measure P_n-values of a special nucleus.

1.5 Neutron detection and neutron shielding

Because neutrons have no charge, they cannot be detected directly. Therefore, neutrons have to be detected indirectly, where a nuclear reaction creates charged particles, which can be observed with common methods. It is distinguished between slow neutrons and fast neutrons, because their interaction with matter is different [Bau01, Kno00, Hos05]. An overview about neutron detection and ^3He spectrometers can be found in [Kra79, Ohm87].

Slow neutrons:

Neutrons with an energy of less than $0.5\,eV$ are called slow. The energy corresponds to the cadmium cutoff and slow neutrons can be absorbed efficiently by cadmium. Neutrons are detected with nuclear conversion reactions like (n, α) or (n, p). Charged products can be detected and the neutron is identified indirectly. Compared to the Q-value of the nuclear reaction, the neutron energy is very small and cannot be resolved. The energy information of the neutron is lost.

For slow neutron detection, most likely one of the following reaction is used:

$$^{10}B + n \rightarrow ^7 Li + \alpha + 2.310MeV \qquad (excited\,state,\ 94\%)$$

$$^{10}B + n \rightarrow ^7 Li + \alpha + 2.792MeV \qquad (ground\,state,\ 6\%)$$

$$^6Li + n \rightarrow ^3 He + \alpha + 4.78MeV$$

$$^3He + n \rightarrow ^3 H + p + 0.764MeV$$

Because there are only two products in each of the reactions, the Q-value is shared discretely to both particles, according to the law of energy and momentum theorems. The $^{10}B(n, \alpha)^7Li$ reaction is used in BF_3 proportional counter tubes and the $^3He(n, p)^3H$ reaction is used in ^3He proportional counters, where ^3He is used as target and proportional gas, whereas BF_3 tubes use fluorine as proportional gas and boron as the target for the reaction. The measured energy spectrum is characterized by the wall effect (see sub chapter 2.1.3 - wall effect) and not by the detected neutron.

$^6LiI(Eu)$ crystals use the $^6Li(n, \alpha)^3He$ reaction in scintillators. A $1cm$ thick crystal is almost 100% efficient for neutron energies around the cadmium cutoff. Because of their short time response, $^6LiI(Eu)$ detectors are used for time of flight measurements – even with higher neutron energies.

Neutrons with intermediate energies:

Detectors for slow neutrons can be very efficient, because the cross section of neutrons increases strongly with low energies. Neutrons with energies in the range between eV and MeV are more difficult to detect. The idea is to moderate the neutrons until they are „slow“ and use detection methods for slow neutrons. Moderation is done in materials with high hydrogen content. Neutrons collide elastically with hydrogen nuclei and lose the energy to the moderation material, which is polyethylene or paraffin in most cases. Disadvantage is the slow response time because of the moderation time. No neutron energy can be measured.

Neutrons with high energies:

For neutrons with energies higher than several MeV, the thermalization would require a lot of time and moderator volume. Because of that, another method is used. Neutrons are scattered on light nuclei and the recoil nuclei are detected. Collisions of neutrons with hydrogen in a scintillator produce recoil protons, which deposit their energy and excite the fluorescence. The measured signal in the photomultiplier is proportional to the neutron energy loss in the scintillator. If the detector absorbs the neutron, the energy information is given.

Neutron shielding:

Low background event rates are desired in all experiments and detector systems. Charged particles can be shielded easily. Because neutrons have no charge and the cross section is very low for high energies, it is more complicated to shield detectors from external neutron sources. The idea is similar to the detection. Neutrons are moderated and with lower energies, they can react with matter, producing other particles, which can be absorbed more easily. Because of similar masses of neutrons and hydrogen, the latter is a good candidate for moderation. Elastic scattering in hydrogen containing materials like water, concrete or paraffin are used for moderation. The second step is the capture of the thermalized neutrons. Boron, Lithium or Cadmium have large cross sections for reactions with neutrons. Two component moderation/absorption materials can be used, like water with boron salt, paraffin-boron, polyethylene-boron or polyethylene-lithium.

Cosmic radiation is difficult to shield because all kinds of radiation is in any energy contained. One way is to use an active shield, which is basically another detector, which detects the cosmic shower and blocks the actual detector system with a veto for the time of the particle passage.

Neutron emission measurements at the NSCL

Data of P_n- values (see sub chapter 1.4 - β delayed neutron emission) can be determined in experiments. Basically, the combination of a β detector and a neutron detector are enough to measure P_n- values of a special nuclei.

Schematic setup:

A secondary beam of designated nuclei is produced by a production target and the separation of the products with a fragment separator. The beam of designated nuclei is routed to the experimental setup, where a nucleus is stopped in the β counting system. Veto detectors before and behind the beta counting system provide the information if and when the nucleus has been stopped. After the β decay, the neutron detector waits for an optional β-delayed neutron. β half-life and β-delayed neutron emission branching can be determined [Hos05-1].

The functionality of the neutron detector is the moderation of the neutron in polyethylene and the detection in a counter tube as described in subsection "Neutrons with intermediate energies".

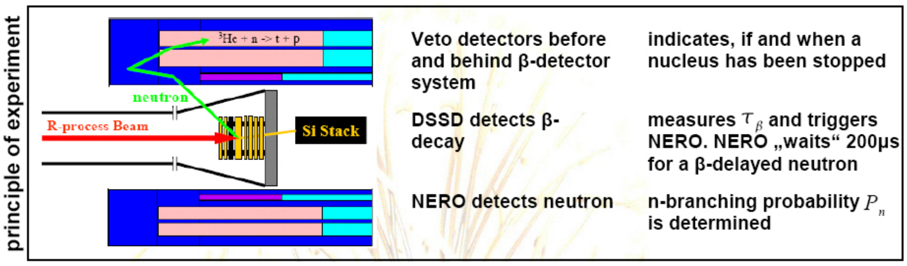

Figure 1.12: Schematic experimental setup with DSSD (doubled- sided Si strip detector) β-detecting system (green) and neutron detector NERO (blue). See sub chapter 2.1.1 for additional information.

Determining P_n-values with experimental data [Hos05]: The β-delayed neutron emission branching of a nucleus is the ratio of the number of β-delayed neutrons to the whole number of β decays (neglecting background of β-delayed neutrons of daughter nuclei). In percent:

$$P_n = \frac{N_{\beta-delayed\,neutron}}{N_{\beta\,parent}} \cdot 100$$

In the experiment, the nuclide is implanted and the β decay half-life is determined with the delay of β detection after the moment of implantation. With the decay constant λ:

$$N_{\beta\,parent} = N_{implanted}(1 - e^{-\lambda t_{corr}})$$

t_{corr} is the correlation time after the implant of the nuclide. All numbers must be corrected for background and detector efficiency. The number of β delayed neutrons is:

$$N_{\beta-delayed\,neutron} = \frac{N_{\beta-n}^{detected} - N_{\beta-n}^{background}}{\epsilon_{\beta-n}}$$

where $\epsilon_{\beta-n} = \epsilon_{neutron\,detector} \cdot \epsilon_{\beta\,detector}$ is the product of the efficiencies of the neutron detector and the β detector.

Another experimental setup is shown in [Kee57].

1.6 NSCL facility

The National Superconducting Cyclotron Laboratory is a world class facility for nuclear research in experiment and theory, established at Michigan State University in East Lansing (Michigan, USA). The NSCL facility pro-

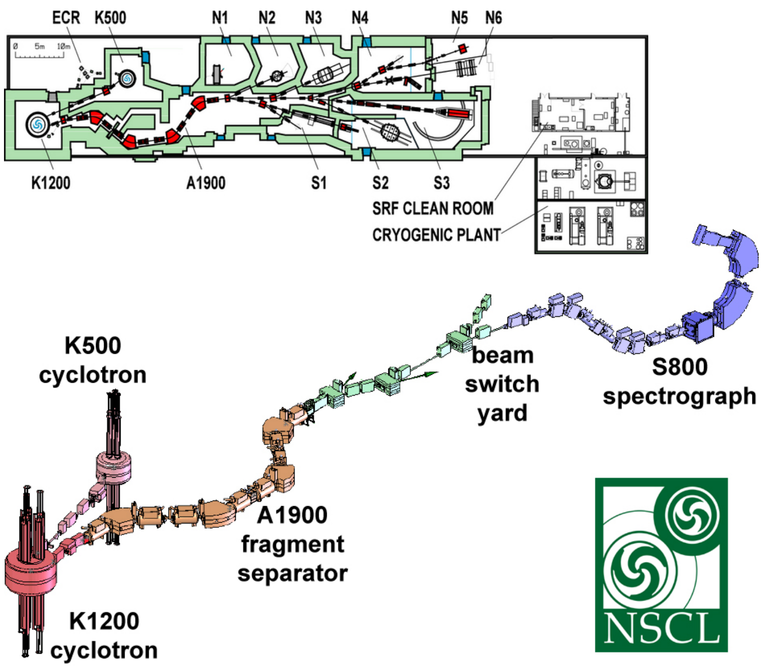

Figure 1.13: NSCL facility [Nsc08]

vides rare and unstable isotope beams, using Electron Cyclotron Resonance (ECR) ion source and two coupled superconducting cyclotrons (K500 and K1200). Energies in the range of $20-200\frac{MeV}{u}$ can be provided. After hitting a production target, the desired isotopes are filtered by the A1900 fragment separator and can be routed to different experimental vaults. Appreciable is here the S800 spectrograph, which achieves its performance with a high energy resolution and a large acceptance of particles. The K500 cyclotron has been used since 1982 and was the first superconducting cyclotron. After 1989, the new K1200 cyclotron became the main accelerator, but in 1999 both accelerators have been coupled what means more beam intensity for all elements and a higher possible beam energy. The laboratory is always in motion and improves it's structure. Until 2010 a re- accelerator and a new experimental area will be built to provide the environment for future research. Several groups work in different fields and applications of nuclear physics starting with nuclear structure, medical applications and ending in astrophysics and the question of the origin of the elements in our universe. Beyond the experimental vaults, there are also smaller laboratories, which are used by research groups to develop and test equipment and prepare experiments. All work within this diploma thesis has been done in a laboratory and not in one of the experimental vaults. Research groups are supported by specialists in the machine shop, electronic shop and other fields. Approximately 300 employees work together to enforce cutting edge research in nuclear physics. The NSCL is a national user facility and is supported by the U.S. National Science Foundation, the U.S. Department of Energy and the Michigan State University [Nsc08].

Chapter 2

Neutron Emission Ratio Observer

2.1 NERO specifications and history

NERO is the abbreviation for "Neutron Emission Ratio Observer". The neutron detector has been designed and built at the NSCL in the context to a Ph.D. thesis by Paul Thomas Hosmer [Hos05].

The design of the detector is based on the Mainz neutron detector (ref. 31 and ref. 32 in [Hos05]) and detects neutrons in an energy range of $1\,keV$ up to several MeV. There were some requirements to construct a neutron detector for the planned experiments:

1. high efficiency for a wide range of neutron energies

2. flat efficiency/energy curve

3. provide enough space for the β detector system

4. fit into existing beam line setup and environment

5. huge solid angle covering and active volume

Neutrons in the intermediate energy range can be detected with the moderation technique (1.5 - n-detection). First, the neutron is moderated in polyethylene and then detected indirectly in a proportional counter tube by a nuclear reaction with charged products. 44 BF_3 and 16 ^3He proportional counter tubes are arranged in three concentric rings around the beam line in the polyethylene block. Exact specifications can be found in 2.1.2 on the following page.

2.1.1 NERO history

For the building of NERO, different resources have been used for the proportional counter tubes. This is why three different models of tubes are used. The outer two rings are assembled with 44 Reuter-Stokes BF_3 proportional counter tubes on loan from Pacific North-West National Laboratory. The inner ring is assembled with 16 ^3He counters of two different models: Twelve tubes are manufactured by Reuter-Stokes on loan from Pacific North- West National Laboratory, the remaining 4 tubes are obtained from University of Mainz. Of course, multiple models of counter tubes within one ring has disadvantages, which is discussed later.

Earlier experiments with NERO:

In 2002, an experiment has been done by P.T. Hosmer et al. to investigate β properties of the r-process nucleus ^{78}Ni. Since ^{78}Ni is a double magic nucleus, it is very interesting for shell-model and r-process calculations. Doubly magic nuclei represent a very important species of nuclei. All in all, there are ten double magic nuclei (considering the classical nuclear shell gaps and excluding super heavy nuclei). Four of them (^{48}Ni , ^{78}Ni , ^{100}Sn , ^{132}Sn) are far away from stability [Hos05-1]. ^{78}Ni is the most neutron-rich nucleus and is particularly interesting for r-process calculations. Because of its filled neutron and proton shells, neighboring nuclei have relatively simple structures and data of ^{78}Ni allow nuclear structure theories to predict properties of them.

For the experiment, the neutron detector NERO (Neutron Emission Ratio Observer) and the NSCL β detector system DSSD (double-sided Si strip detector) were used in combination. The ^{78}Ni-nucleus was stopped in the Si stack of the DSSD system and veto detectors before and behind the system observe if, and when the nucleus is stopped. The β decay was detected with its position by 40×40 strips of the Si detector and gives the β half-life. The β decay triggers NERO and the neutron detector is awaiting the possible delayed neutron emission for a time window of 200µs.

The secondary beam of ^{78}Ni was produced by the fragmentation of $^{86}Kr^{34+}$ with $140\frac{MeV}{nucleon}$ at a beryllium target. ^{78}Ni nuclei were then separated from the cocktail of particles by the A1900 fragment separator (see beam line in figure 1.6 on page 23). The identification of the ^{78}Ni nuclei was done by a time of flight measurement versus energy loss. The total β event rate, associated with implanted nuclei has been less than $3 \cdot 10^{-2}\frac{1}{s}$. During 104 hours of beam time, only 11 ^{78}Ni are identified. This shows the necessity of high efficiency detectors and low background rates for β- and n-detection. The experiment has provided the first results for the β half-life of ^{78}Ni and other neutron-rich Ni isotopes. With the ^{78}Ni experiment, experimental data are now available for all double magic nuclei except ^{48}Ni.

2.1.2 NERO specifications

NERO is composed of polyethylene for moderation of neutrons and 60 counter tubes for indirectly detection of the moderated neutrons. The polyethylene block measures 60cm in height and width, and 80cm in length

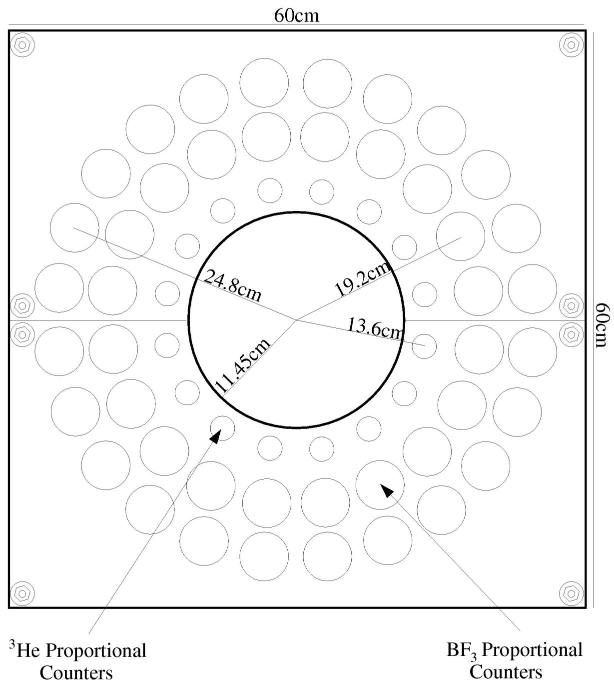

Figure 2.1: Schematic diagram of NERO

along beam line. The beam line cutout is in the center line and has a diameter of $22.9cm$. There are three different counter tubes arranged in three concentric rings around the beam line. The inner ring has a radius of $13.6cm$, the second ring $19.2cm$ and the outer ring $24.8cm$. The second (20 tubes) and the outer ring (24 tubes) are assembled with BF_3 counter tubes. The inner ring is filled with 16 ^3He counter tubes, where 12 counter tubes are borrowed from Pacific Northwest National Laboratory, and four from University of Mainz, Germany.

The polyethylene moderation block is consisting of 12 sub blocks. In beam axis, there is an upper and lower half – in side view, there are 5 vertical cuts along the beam line. This makes handling and moving the total weight of $180kg$ much more comfortable and provides a high degree of mobility and flexibility. The blocks are arranged and supported by 8 threaded rods in beam line direction. When assembling NERO, it has to be assured, that holes for tubes are aligned well. It is recommendable first to align the bottom half and fix it with the rods and then put the top half on it and also fix the alignment. During assembling, it has to be checked, if tubes can be moved into NERO easily. The holes for the tubes are not continuous but have the right length to position all tubes on their centered position in beam axis. Exception is here the inner ring (^3He), because tubes from Mainz and PNNL have different lengths, but the holes are drilled in the same depth.

In the development of NERO, the efficiency has been estimated with MCNP simulations. All materials, counter tubes and threaded rods have been considered and the arrangement and number of counter tubes is optimized.

The electronics is organized in quads named A, B, C and D. Each quad has 15 proportional tubes, a 16 channel preamplifier and a 16 channel shaper/ discriminator module. The numeration of the tube position starts in the inner ring clockwise (inner ring: tube 1-4), continues to the middle ring (tube 5-9) and then to the outer ring (tube 10-15), where the clockwise counting is always followed (see figure 2.2).

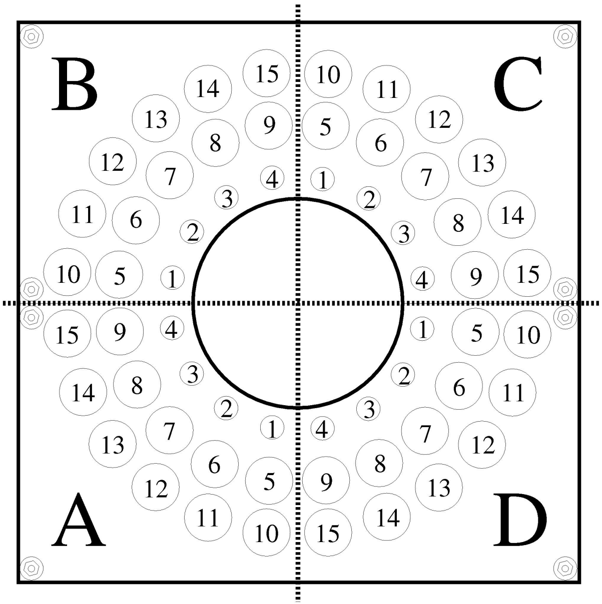

Figure 2.2: NERO tube map

The NERO detector is described as an almost 4π detector [Hos05]. Obviously, there is a hole of $22.9cm$ diameter along the beam line. In order to estimate the solid angle, some simple calculations are done. When one considers the angle β in figure 2.3 on the facing page, the polyethylene block covers 89.8% of the 4π solid angle. β is the minimum angle, where the neutron has to pass more than $18.6cm$ (straight) in polyethylene, before leaving the detector. $18.6cm$ is the smallest possible distance a neutron has to cross, when it is emitted orthogonal to the beam line in the center of the detector.

Anyway, the real active volume might be different and has been calculated in MCNP simulations before. For the experimental measurements in this thesis, there will be no solid angle corrections, since we wanted to compare with previous measurements and simulations which have considered this circumstance in the same way.

The whole detector is conceived to work with the NSCL Beta Counting System (BCS) which is an important part in the experimental mode of NERO, since the β decay triggers NERO.

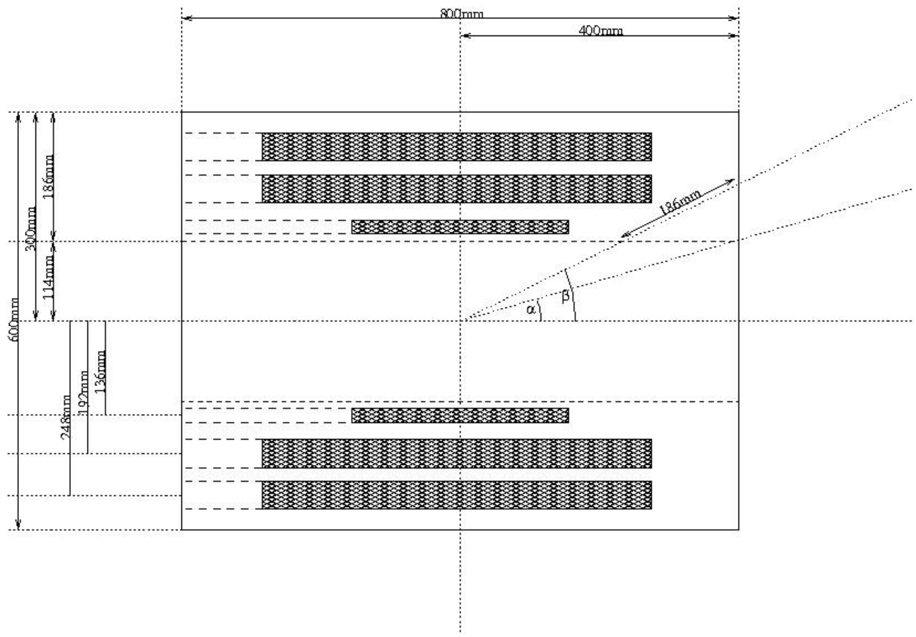

Figure 2.3: NERO schematic cut - side view

Experimental mode / standalone mode:

In experiment, the neutron detector is used in combination with the DSSD β counting system. In this case, NERO is triggered by the β decay and a time window of 200μs is opened for the detection of a β-delayed neutron. The time delay of the neutron detection is measured by a Time to Digital Converter. The TDC start is provided by the β decay, the TDC stop comes with a detected neutron.

In standalone mode, there is no external trigger, but NERO is triggered on neutrons. Since the electronics and logic take some time to process the electronic information, the stop signal for the TDC has to be delayed to assure a time delay to the start signal, which is set by the same neutron like the stop signal. Because of that, four long 34 flat ribbon cables are used to delay the stop signal of all channels of the TDC (see sub chapter 2.2). In this thesis, NERO is always used without the DSSD system in standalone mode. The only exceptions (see sub chapter 3.6) are highlighted.

2.1.3 NERO detector functionality / wall effect

Moderation and MCNP efficiency

In experimental and standalone mode, it is assumed that a neutron is emitted in the center of NERO in the middle of beam line axis. In experiment, this happens by stopping the nuclei in the silicon stack. A nucleus is stopped, followed by a β decay and some time later, a possible β-delayed neutron is emitted. In standalone/test mode, the neutron is emitted from a

^{252}Cf source, which is used to check the detector system, estimate efficiencies and measure the moderation time of NERO.

A neutron is electrically neutral, which means that interaction with matter is much less likely than for protons or charged particles in general. The cross section for scattering in the moderation material of neutrons increases with decreasing energy. Proportional tubes only can be used to detect slow neutrons ($E < 0.5eV$, see sub chapter 1.5).

In order to slow down neutrons to an energy, where they easily react in counter tubes, they have to be moderated. Similar to the moderation of neutrons in a nuclear power plant, neutrons are slowed down by collisions with particles similar masses. Materials with hydrogen are used, and because of additional physical properties, polyethylene has been used to build NERO.

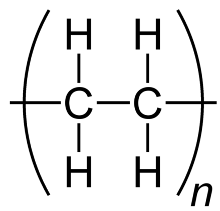

Figure 2.4: Polyethylene

The moderation time depends obviously on the rate of collisions which is given by properties of the material (e.g. density), but also varies by stochastic fluctuations. Some neutrons are moderated faster, some slower. One can expect an exponential distribution of the moderation times. The moderation time of NERO has been calculated in simulations by Giuseppe Lorusso [Lor08] and measured experimentally (see sub chapter 2.7). Neutrons with high energies need more collisions to moderate than neutrons with lower energies. Even though neutrons do not follow a direction, but change their trajectory with every collision, it is obvious, that high energy neutrons need more volume to moderate than slower neutrons. The other way around, there is a limitation of the upper limit of the sensitive energy range, just because of the volume of the moderation material.

Basically, the efficiency of the whole neutron detector depends on the ability to slow down neutrons and the allocation of the counter tubes. If a neutron is moderated and the cross section is high enough for probable nuclear reactions, it has to reach one of the gas tubes. Of course the neutron reaction cross section of hydrogen and carbon in polyethylene is smaller than for boron or ^3He, but the number, volume and position of the counter tubes have to be optimized. If a neutron reacts outside the proportional tubes by a (n, γ) reaction, it is not detected. Hence, number and volume of the counter tubes and the spacing between them and the rings must be optimized, so the moderated neutron reach the active volume of a gas tube.

All mentioned issues have been optimized by MCNP simulations and the design is mainly based on it.

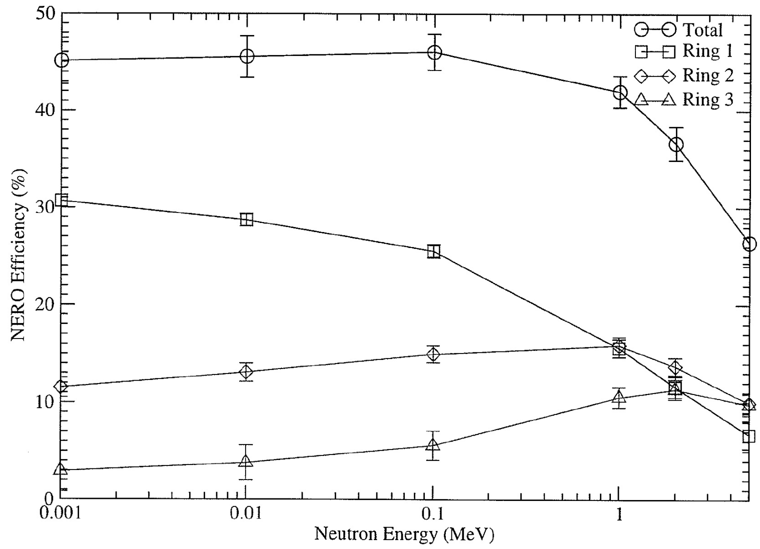

Figure 2.5: NERO efficiency vs. neutron energy MCNP simulation: Ring 1 is the inner ring with ^3He counter tubes. Ring 2 and Ring 3 are the middle and outer rings, assembled with BF_3 tubes. [Hos05]

The energy of the ^{78}Ni β-delayed emitted neutron has been predicted to be in a range of $0.1 - 1\,MeV$. Because of the wide energy range, a flat efficiency dependency on energy has to be achieved. Figure 2.5 shows the MCNP simulation efficiency curve. Rings with increasing numbers have efficiency maxima for increasing energies. This makes sense, since neutrons with higher energies need more volume to become moderated and are able to penetrate deeper into the polyethylene. Simplified, neutrons with high energies are detected preferentially in outer rings, neutrons with lower energies are detected preferentially in the inner ring. This effect is the only way to get an idea of the original energy of the neutron. An exact energy information of the neutron can not be achieved.

The sum of efficiencies of all three rings is the total efficiency of the detector. It is constant at a value of approx. 45% for $1keV$ up to $300keV$ and decreases to 42% at $1MeV$ and to 26% at $5MeV$. In the past, an efficiency calibration has been done at Nuclear Structure Laboratory at University of Notre Dame for neutron energies between 0.6 and $3.4MeV$ from resonance reactions. The efficiencies were $33.2 \pm 2.5\%$ ($0.6 \pm 0.2MeV$ neutrons), $24.4 \pm 1.3\%$ ($3.0 \pm 0.4MeV$ neutrons) and $27.6 \pm 1.5\%$ ($3.4 \pm 0.6MeV$ neutrons) [Hos05].

A quick efficiency measurement is possible with the neutron source ^{252}Cf (see sub chapter 2.4 - ^{252}Cf source). It emits neutrons with an energies up to $6MeV$ and an average energy of $2.35MeV$. Most neutrons are emitted with an energy of about $1MeV$ (see sub chapter 2.6). This way, the efficiency for neutrons from spontaneous fission of ^{252}Cf has been determined by Hosmer to be $26.4 \pm 1.5\%$. New measurements confirm this result. It is difficult to compare an efficiency measurement with non discrete neutron energies with the MCNP simulation.

Proportional tubes

NERO consists of 60 proportional counter tubes, which are embedded in the polyethylene.

After moderation of the neutron, the detection in the gas tubes is done by (n, α) and (n, p) reactions with the target gases. A general overview about neutron detection can be found in sub chapter 1.5 - neutron detection and shielding.

Reaction of the neutron in BF_3 counter tubes:

$$^{10}B + n \rightarrow ^7 Li + \alpha + 2.310MeV \qquad (excited\, state,\ 94\%)$$

$$^{10}B + n \rightarrow ^7 Li + \alpha + 2.792MeV \qquad (ground\, state,\ 6\%)$$

Reaction of the neutron in ^3He counter tubes:

$$^3He + n \rightarrow ^3 H + p + 0.764MeV$$

Since the neutron has been moderated to an energy of less than $0.5\, eV$, the deposited energy by the charged products at the anode is not related to the original energy of the neutron but to the Q-value of the (n, α), (n, p) reactions. Also the energy of less than $0.5\, eV$ is not resolvable and is neglected. ^3He and BF_3 tubes provide a characteristic energy spectrum which is affected by wall effects.

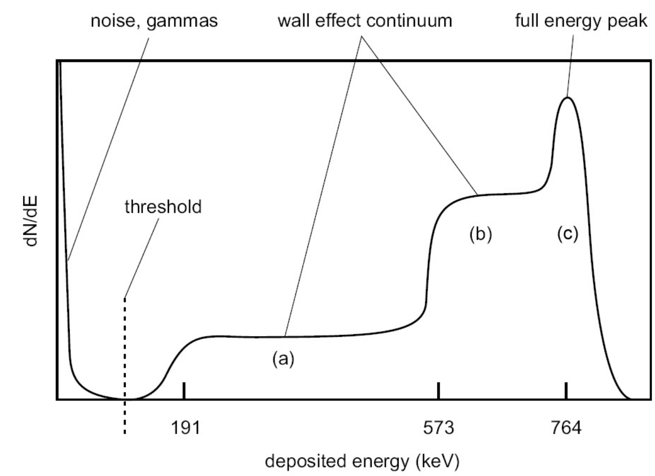

Figure 2.6: Schematic ^3He energy spectrum, characterized by wall effects [Bau01].

Figure 2.6 on the preceding page shows schematically the typical energy spectrum of a ^3He proportional counter, which can be explained by wall effects. The total energy of $764\,keV$, released in the exothermic (n, p) reaction is shared by the two products of the reaction - ^3H and proton. Since it is a two-body problem and one knows masses of both products, one can calculate the kinetic energies of each particle. ^3H gets an kinematic energy of $191\,KeV$ and the proton gets the rest of $573\,keV$.

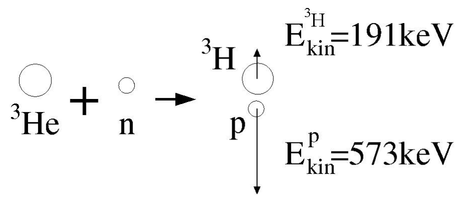

Figure 2.7: Nuclear n-reaction with ^3He.

The peak at $764\,keV$ in figure 2.6 represents the situation, that both products completely deposit their energy inside the counter tube (c). Continuum (a) represents the situation, where the ^3H particle deposits all energy in the tube and the proton only a fraction of its energy and leaves the counter gas volume. Continuum (b) represents the situation, where the proton deposits all energy in the tube and the ^3H particle only a fraction of its energy. These effects are called wall effects.

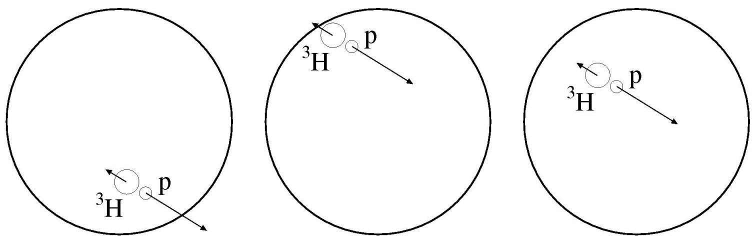

Figure 2.8: Wall effects as described in text: a) b) c)

The same effects can be observed in the BF_3 gas counters. The energy plateaus start at $0.840\,MeV$ $(1.015\,MeV)$ and $1.470\,MeV$ $(1.777\,MeV)$ and the full energy peaks are at energies of $2.310\,MeV$ and $2.792\,MeV$ for the ground state and the first excited state, respectively. Because of the branching between the ground state (94%) and the first excited state (6%), the energy spectrum is less sharp and the full energy peak has a greater width.

The noise-/γ-peak for low energies can also be observed with NERO. The effect is enforced because of the trigger logic. If one of the 60 proportional counters gets an event, the energy of all tubes is measured, but since most of the other counters do not see a neutron event in coincidence, just noise and low energy non-neutron events are measured. This issue can be solved by a threshold for the energy spectra.

Set of proportional counters, used in NERO:

Type	BF_3	^3He(PNNL)	^3He(Mainz)
manufacture	Reuter Strokes	Reuter Strokes	Reuter Strokes
model	RS-P1-1620-205	RS-P4-0814-207	RS-P4-0810-104
radius	$2.54cm$	$1.27cm$	$1.27cm$
inactive length	$55.88cm$	$43.18cm$	$26.01cm$
active length	$50.8cm$	$35.56cm$	$24.99cm$
nom. pressure	$1.18atm$	$4atm$	$5.732atm$
voltage	$2620V$	$1100V$	$1350V$
position	ring 1, ring 2	ring 1, quad D	ring 1, quad A, B, C

Table 2.1: Set of proportional tubes [Hos05]

The BF^3 gas is enriched in ^{10}B to greater than 96%. The casing is 304 Stainless Steel. The different ^3He tubes have different properties and different active lengths. This must have an influence to the efficiency of ring 1 quad D compared to other quads (see sub chapter 2.6).

The BF_3 tubes have a housing for a preamplifier attached directly to the tube. In the NERO setup, this housing is not used, but just a wire passes the signal through. Anyway, this connection can become lose. The old preamplifier housing is screwed to the counter tube. The exact alignment of tube and housing is important, since the housing has to fit into the hole in the polyethylene. The copper housing also should be closed properly and it has to be assured, that the pin fits into the counter tube connector.

Figure 2.9: Old preamp housing attached to BF_3 tubes

2.2 NERO electronic setup

As described in sub chapter 2.1.2, NERO is used in experiments in combination with the DSSD β detector system, which triggers NERO. For testing, NERO can be used in standalone mode, where NERO is not triggered externally by β decay, but self-triggered on neutrons. Only few hardware modifications are necessary to switch from experimental mode to standalone mode. The electronic diagram for standalone mode can be found in appendix 5.6.

Hardware Setup for NERO in standalone mode:

It is mentioned in sub chapter 2.1.2, that the detector is organized in quads. This organization is reflected in the first part of the electronics. Each quad has 15 proportional counter tubes, where the first four of numeration are ^3He gas tubes, and the remaining 11 tubes are BF_3 tubes. The tubes of each quad are connected to one preamplifier box by HV cables (RG-58 for BF_3 and RG-158 for ^3He). Because BF_3 and ^3He tubes are biased with different voltages, different plugs are used to avoid an interchange and possible damage to ^3He tubes. The HV supply for BF_3 and ^3He is provided by two HV sources for each preamplifier box and is split internally to the different channels (see sub chapter 2.2.1). The signals of the tubes are amplified and routed via 34-wire flat ribbon cables to one of the four PICO shaper / discriminator modules (see sub chapter 2.2.2). The shaped signal is routed to one of the two 32ch C.A.E.N ADCs (see sub chapter 2.2.5). The 15 discriminator signals provide the stop signals in the 64ch C.A.E.N TDC (see sub chapter 2.2.4). The flat ribbon cable from the discriminator to the TDC is split and connected to one of the two 32ch SIS scalers.

This setup is the same for all quads. The two 32ch ADCs measure the energy for all 60 tubes separately. The 64ch TDC works in multi-hit mode and processes all 60 tubes in parallel. The two 32ch scalers just count the discriminator signals for each tube separately. The discriminators provide four OR outputs of 16 channels, each. The ORs of the quads are merged, using a Fan In Fan Out and provide the so called "Master Gate", which is the basis of the NERO standalone trigger system.

A logical AND in the trigger logic guarantees, that all informations are processed in a controlled way and the computer finished the readout and the clearing of the informations in the modules before the next event is processed.

The "Master Gate" is connected to the AND input, and the output of the AND is the so called "Master Gate Live". Another input of the AND is the looped back inverted signal of the busy LATCH2. It is set by the Master Gate Live and blocks the AND until it is reset by the computer and the readout of the previous event is processed. LATCH2 also sets a bit in the I/O-Register and informs the computer, that an event is being processed. The gate of LATCH3 starts the TDC time measurement and keeps it sensitive for $200\mu s$. The use of the signal from LATCH3 for the TDC start is only necessary in standalone mode. In experimental mode, the β detector provides the TDC start signal. NERO LATCH3 also sets a timeout bit in the I/O-Register, when no TDC gate is pending.

The second hardware difference between standalone mode and experimental mode is the standalone LATCH1, which is also set by the AND output and reset by a trigger acknowledge bit by the computer. LATCH1 sets a bit in the I/O-Register, which is read out by the computer to adjust the timing with the software.

Last but not least, the ADCs are gated by the Master Gate Live signal, which is adjusted in time delay and length to provide an adequate gate.

Because of the self-triggering, the stop signal of the TDC must be delayed for all 60 channels to provide enough time to the logic to start the TDC gate. This is done by four long flat ribbon cables (see sub chapter 2.2.4).

The electronic modules (shaper / discriminator) and also the preamplifier boxes, which process the data for different quads have a 16ch architecture. Since only 15 channels per quad are needed, one channel per quad is in spare. All in all, the multichannel modules provide 64 channels for 60 tubes. In the case of the scalers, the residual channels are used to monitor the rates in the Master Gate and Master Gate Live.

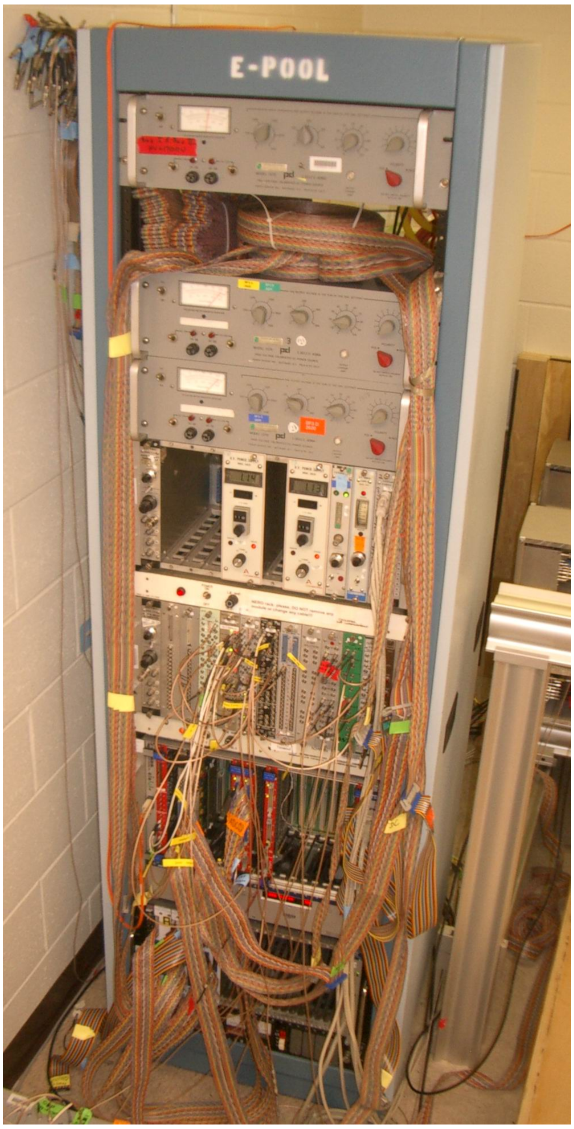

Figure 2.10: Electronic crate

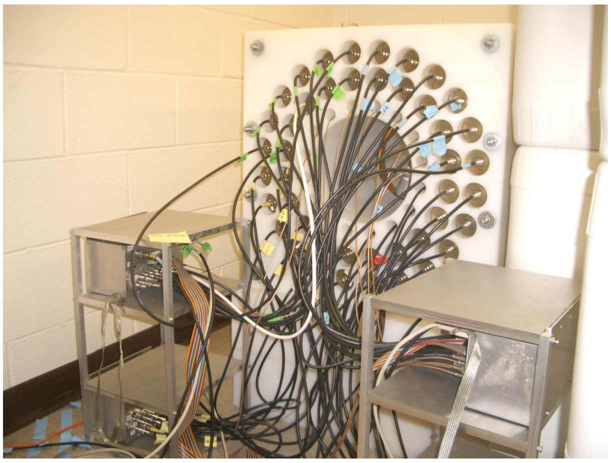

Figure 2.11: NERO and preamplifier boxes.

The four PICO shaper / discriminator are CAMAC modules, placed in the crate at the bottom of the rack (see figure 2.10). In the VME module about the CAMAC crate, an I/O-Register, two 32ch ADCs, a 32ch QDC (see sub chapter 3.3) and the 64ch TDC are mounted. An additional module allows communication and control between VME and CAMAC crate. The NIM crate is the housing for the logic modules and the modules for the active cosmic ray shield (see sub chapter 3). The modules in the NIM crate are: quad Gate & Delay generator, quad Latch, quad AND logic, quad Fan In Fan Out, 16ch ECL-NIM-ECL converter, quad 2-way splitter, NIM delay box ($8 \cdot 10ns$, $8 \cdot 20ns$), quad fast amplifier (green NSCL), quad CFD. The last four modules are only added for electronics of the active cosmic ray shield (see chapter 3). A second NIM crate above the logic crate is base for four high voltage supplies for the ^3He tubes, grouped in quad A, B, C and D. An additional module provides a $\pm 6V$ power supply for the preamplifier boxes (see sub chapter 2.2.1). The two gray adjacent high voltage supplies with two outputs each, bias the BF_3 tubes in quad A, B (upper HV module) and C, D (lower HV module). The HV module at the top of the rack is used for the scintillators of the active cosmic ray shield. On top of the BF_3 HV supplies, four long 34ch flat ribbon cables provide the necessary delay for the TDC stop signals.

Hardware Setup for NERO in experimental mode

For the change to the experimental mode, only few connections in the logic have to be changed. NERO LATCH3 is set and reset externally by the β-decay signal and not by the Master Gate Live. In addition to that, the AND is extended with an input from NERO LATCH3. This assures that only NERO events are accepted, which are correlated with a β-decay. Standalone LATCH1 is still used for trigger acknowledge, but is embedded in the DSSD trigger.

2.2.1 Preamplifier boxes / High Voltage supply

Each of the four preamplifier boxes has two functions. First, it splits and routes the high voltage for BF_3 and ^3He tubes to the according channels (channel 1-4: ^3He, channel 5-16: BF_3). Second, the charge at the anode is collected and measured, the signal preamplified and provided to the data acquisition. The box is the housing for a board, designed and fabricated at the NSCL with 16 Cremat CR-101D miniature charge sensitive preamplifier chips, which are specifically designed for nuclear detection instrumentation.

The box has three inputs (HV_{BF_3}, $HV_{^3He}$ and power supply for the Cremat chips), 16 HV connections to the tubes and one 16ch output to the shaper.

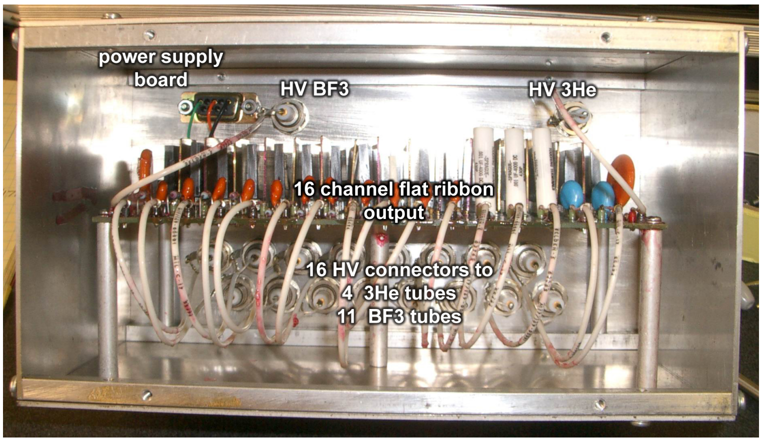

Figure 2.12: Inside of a preamplifier box

The board is supplied by a voltage of $\pm 9V$. Because the NIM module provides only $\pm 6V$, the voltage is converted in a small custom made box, which transforms 4x $\pm 6V$ to 4x $\pm 9V$.

If one signal channel is dead, and the defect is located in a preamplifier box, the Cremat chips can be exchanged, since they are just plugged in and not soldered. Between the preamplifier chips is a copper shield for cooling. In order to find a potential error, a cable from the tube can be routed to the spare channel to check if the problem can be located. The inside of the preamplifier boxes should be clean and all connectors have to be well attached to the box. In addition to that, each preamplifier box has to be grounded to avoid electronic noise.

All four preamplifier boxes have an identical structure, but produce noise in different quantities. Quad A produces as much noise / background as quad B, C and D together, but the issue could not be eliminated (see sub chapter 2.5).

The high voltage supplies for BF_3 and ^3He are provided by several modules. Two „High Voltage calibrated DC power sources“ with two outputs (Power Designs Inc. Westbury, N.Y., model 1570, 1...3012V, 40mA) provide the voltage for the BF_3 tubes in quad A / B and C / D. The ^3He tubes are biased by four modules (see table 2.2).

group	type, model	value
quad A	Cranberra, Model 3002D	1.13
quad B	Cranberra, Model 3002D	1.13
quad C	Tennelec, TC947	5.26
quad D	Cranberra, Model 3105	1.33

Table 2.2: HV modules with settings for ^3He

The number in the last row of table 2.2 represents the value, the HV module has to be set to in order to provide the desired voltage. In case of quad C and quad D this number is not indicating the provided voltage in kV. The desired voltages for the different counter tubes can be found in table 2.1.

2.2.2 Electronics: Pico Systems Shaper / Discriminator

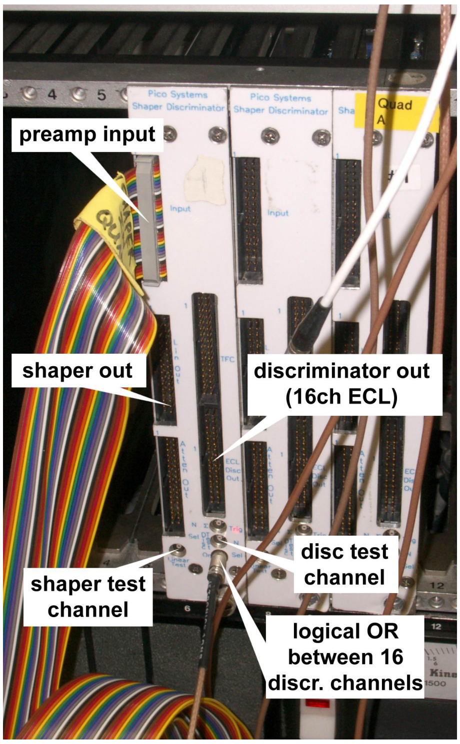

Figure 2.13: Pico Systems shaper / discriminator with labeled used connectors.

The 16 channel Pico Systems shaper / discriminator combines two modules. The CAMAC module occupies two slots. The left half shapes and amplifies the signal and provides several outputs. Internally, the signal is passed to the CFD discriminator on the right half of the module, which produces the logic impulse. The module is controlled and all settings are done by computer via a VME / CAMAC bus. The inputs and outputs, which have been used are labeled in the figure 2.13.

Shaper:

The signal from the preamplifier is prepared by the shaper for further processing in ADC or CFD. The gain of each channel can be set in "shaper_init _NERO.dat" in the readout directory (see figure 2.14). In addition to that, any of the 16 channels can be routed to the lemo test output. Internally, the module can be customized to the experimental requirements. Resistors and capacities for each channel are plugged in and can be replaced easily. The NERO setup uses the configuration in table 2.3 of the shaper:

position	R
R06	$1k\Omega$
R07	106Ω
R08	255Ω
R11	26.4Ω
R12	390Ω

position	capacity label
C01	K5K 233
C02	K5U 105 M
C03	K2J 270
C04	681J COG 63
C05	68J COG 63
C06	BC 101

Table 2.3: Resistors and capacities in the shaper unit

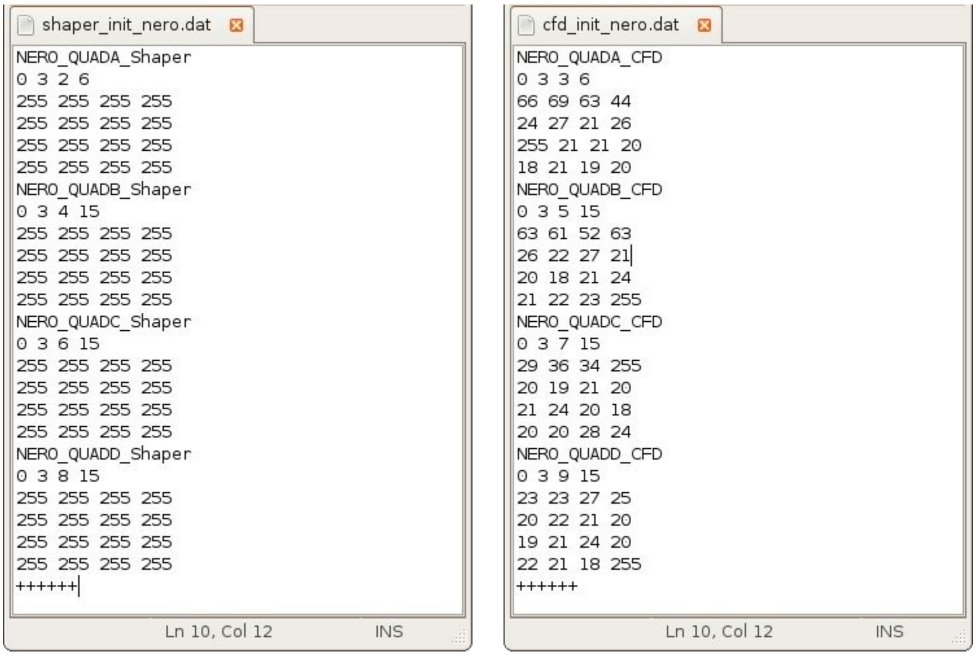

shaper_init_nero.dat

```
NERO_QUADA_Shaper
0 3 2 6
255 255 255 255
255 255 255 255
255 255 255 255
255 255 255 255
NERO_QUADB_Shaper
0 3 4 15
255 255 255 255
255 255 255 255
255 255 255 255
255 255 255 255
NERO_QUADC_Shaper
0 3 6 15
255 255 255 255
255 255 255 255
255 255 255 255
255 255 255 255
NERO_QUADD_Shaper
0 3 8 15
255 255 255 255
255 255 255 255
255 255 255 255
255 255 255 255
++++++
```

Ln 10, Col 12 INS

cfd_init_nero.dat

```
NERO_QUADA_CFD
0 3 3 6
66 69 63 44
24 27 21 26
255 21 21 20
18 21 19 20
NERO_QUADB_CFD
0 3 5 15
63 61 52 63
26 22 27 21
20 18 21 24
21 22 23 255
NERO_QUADC_CFD
0 3 7 15
29 36 34 255
20 19 21 20
21 24 20 18
20 20 28 24
NERO_QUADD_CFD
0 3 9 15
23 23 27 25
20 22 21 20
19 21 24 20
22 21 18 255
++++++
```

Ln 10, Col 12 INS

Figure 2.14: Initialization files of shaper (left) / discriminator (right)

The first four numbers of each block in the initialization files (figure 2.14) define crate (0), branch (3), slot (2=shaper, 3=CFD) and the test output channel (6). The following 16 values set the gain (shaper) or threshold (CFD) for different channels and can be set between 0 and 255. In figure 2.14 (left), channel 6 is routed to the test output of shaper A. The CFD initialization file "cfd_init_NERO.dat" (figure 2.14 (right)) is also located in the readout directory.

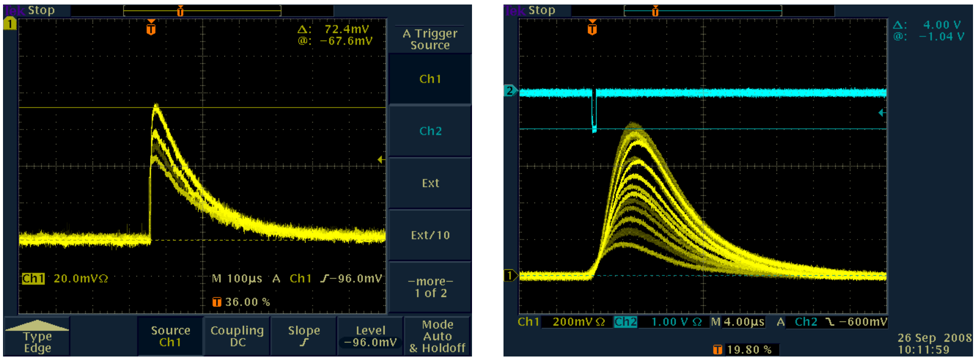

Figure 2.15: Signals after preamplifier (left) and after shaper (right) for a ^3He tube.

The left screen of the scope in figure 2.15 shows signals from the preamplifier of tube A1 (^3He counter). The right picture shows signals of the same channel after shaping. The signal is amplified by a factor of approx. 10 and the shape is smooth. The shaped signal is routed to the ADC where the charge is measured.

The amplitude of BF_3 signals is generally smaller, but the shaper amplification factor is in the same range. The difference is given by the properties of the counter tubes, where gas, pressure and dimensions are different.

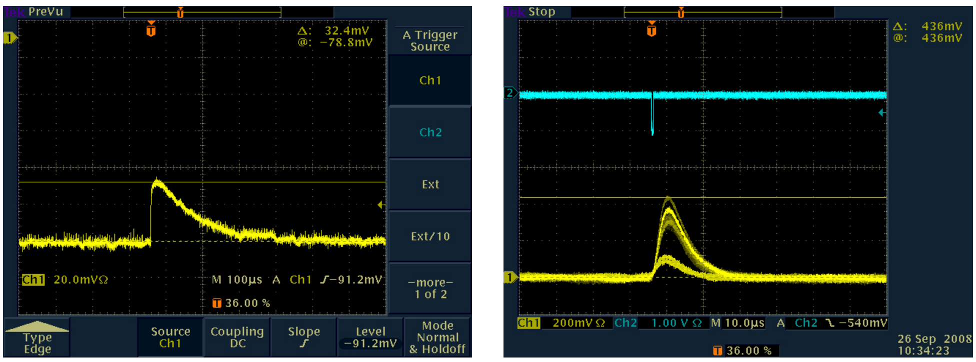

Figure 2.16: Signal after preamp (left) and after shaper (right) for a BF_3 tube.

Discriminator:

The constant fraction discriminator receives the signals internally from the shaper. The test output channel is selected similar to the shaper in the "cfd_init _NERO.dat" file (figure 2.14). Setting the thresholds for each channels is a very time consuming procedure and is explained at the end of this chapter in 2.2.6. The NIM "OR" output (see figure 2.13) is the OR of all 16 CFD channels and provides (after all four quads are merged) the Master Gate. The ECL signals of the 16 channel "discriminator out" are delayed and provide the stop signal in the TDC. Also the discriminator can be modified internally by replacing resistors and capacities. The NERO configuration is given in table 2.4.

position	resistor
R12	390Ω

position	capacity
C01	682 (BC)
C06	473 (M)
C07	K5J 471
C08	K2J 770
C21	BC 102

Table 2.4: Resistors and capacities in the discriminator unit

If a shaper / discriminator channel seems to be dead, it is worth to check the replaceable units. For more information see the module documentation in reference [Pic08].

CAMAC

Basically, CAMAC is a reliable system, but one malfunction could be ascribed to the CAMAC crate. All discriminators were producing logic signals, even when no input cable from the preamplifier was connected. If one of the four shaper/ discriminator had been removed, the malfunction disappeared. After the CAMAC crate had been replaced, all discriminators worked correct again.

2.2.3 Electronics: C.A.E.N. Mod V262 - I/O-Register

The interface between VME / CAMAC bus and computer is provided by a SBS Technologies Inc. module. It is plugged into the first VME slot and and has only one fiber glass cable jack at the front, which connects the computer. Three LED indicate the operating status of the module. The VME and CAMAC bus can be used to write settings to the different modules or readout their memory.

The I/O-Register is a nice way to read or set NIM and ECL level outputs in order to use them as a time alignment between hardware and software.

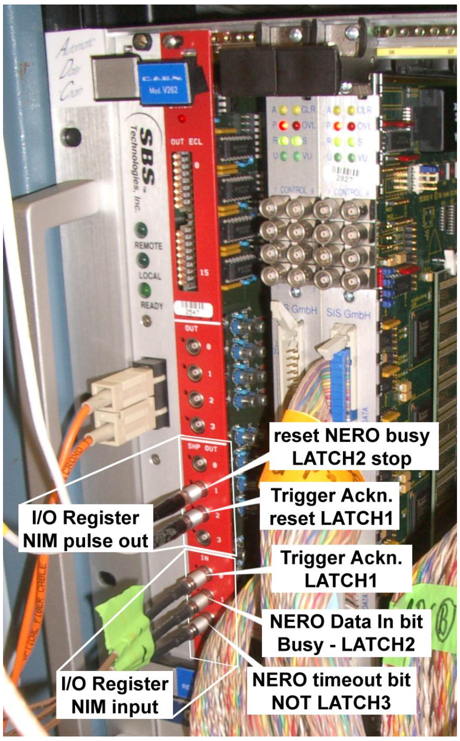

Figure 2.17: I/O-Register C.A.E.N. Mod V262

For example the NERO Busy LATCH2 sets a bit in I/O VME IN1, which can be read out in the software and used for “if”- decisions and for time adjustments in the data readout procedure. On the other hand, the NERO Busy LATCH2 is reset by SHP1 NIM output of the I/O-Register. This pulse is sent after the readout is finished. Until LATCH2 is reset, the Master Gate Live is blocked and it is assured, that data readout is finished and the modules are cleared, before the next event is allowed. The readout code can be found in

nerotest/Standalone/readout/NEROSegment.cpp

(see sub chapter 2.3.2). The module is initialized with the command:

m_PIOREGISTER = new CaenIO(BASEVMEIO, CRATENUM1);

Where *m_PIOREGISTER* is the pointer, which is used in the program code to call functions and operations for this module. *BASEVMEIO* is defined as the base address of the I/O-Register, which is basically given by the slot number in the VME crate. *CRATENUM1* is the number of the crate, but as the NERO setup uses only one crate, this value does not change.

command	action
m_PIOREGISTER->ClearAll();	clears all settings of I/O- Register
m_PIOREGISTER->ReadInput(1);	reads, if NIM signals is true at input IN 1
m_PIOREGISTER->SetLevel(1);	sets a NIM signal at the output SHP OUT 1
m_PIOREGISTER->ClearLevel(1);	clears the NIM output signal at SHP OUT 1

These few commands give an idea, how to handle the I/O-Register. SHP OUT can be used for the hardware logic. The NERO setup uses NIM inputs IN 0-2 and the NIM outputs 1 and 2, but the module is much more powerful. It can read four NIM level inputs and generate four NIM pulses and 16 ECL levels.

2.2.4 Electronics: C.A.E.N. VME V767 - 64ch TDC

The NERO Setup uses a C.A.E.N. 64 channel general purpose multi-hit Time to Digital Converter Mod.V767A to measure the time delay between β decay of the stopped nucleus and the detection of a possibly delayed emitted neutron. Because of the variable moderation time, no direct physical information in the time delay of the detection of the β-delayed neutron emission can be achieved.

In standalone mode, NERO is triggered by neutrons. Because of that, start and stop signals of the TDC are related by a fixed delay which is defined by the length of the four 16ch flat ribbon cables between discriminator and TDC stop (delay$\approx$ 0.4µs). Basically, one expects all events in the same bin in the time spectra. Exceptions are events, which hit the 200µs window in coincidence to the first event. The time window of 200µs is given by the moderation time (see sub chapter 2.7). The start gate is produced by the NIM trigger logic and a gate generator. The start gate has to be converted to ECL, before it is routed to the TDC start input, because the TDC works with ECL signals.

If a ^{252}Cf neutron source is used, each fission event emits up to 6 neutrons (see sub chapter 2.4) in coincidence. Since the moderation time varies, the neutrons can be detected one after the other. The first one will start the NERO trigger system and open the TDC gate for 200µs. After the hardware delay of 0.4µs, the same event produces a stop signal in the corresponding TDC channel. The other neutrons, which are more delayed because of the varying moderation time, probably will be detected in different tubes and produce stop signals in one of the other channels. Because the TDC is used in multi- hit mode, several stop signals can be recorded, even in the same channel.

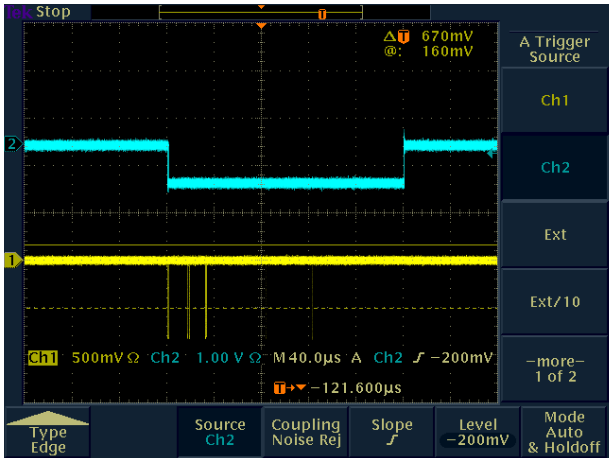

Figure 2.18: TDC gate (blue) and stop signals (yellow)

At the beginning of this work, a time calibration was performed to check the TDC, because time spectra were looking strange. Finally it turned out, that defect connectors and cables were the cause of all troubles. Reflexions in the delay cables produced an immense number of stop signals.

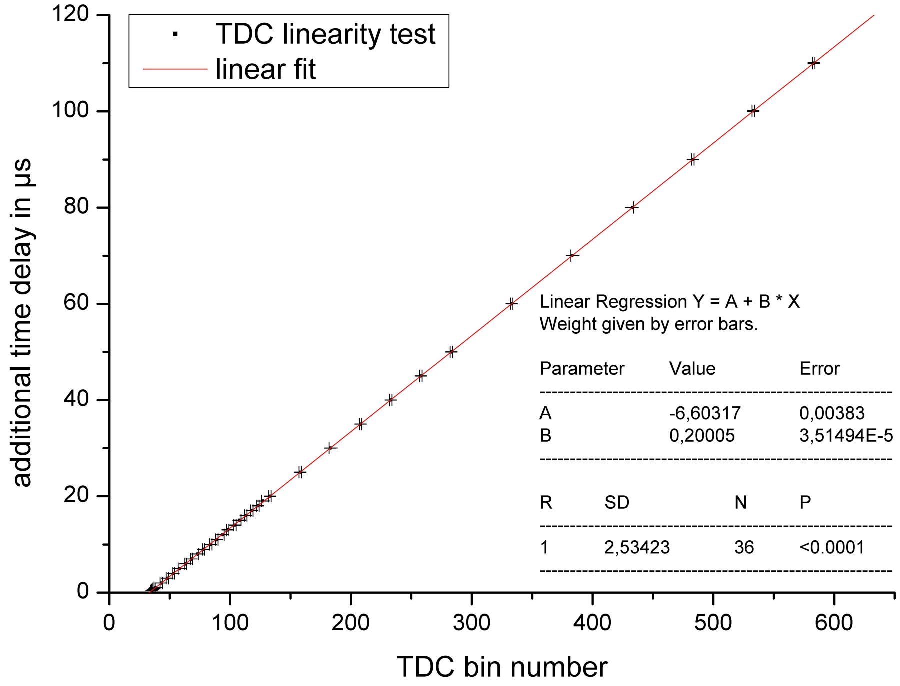

Figure 2.19: TDC linearity test

The linear fit in figure 2.19 specifies the width of one TDC bin to $(0,20005 \pm 3 \cdot 10^{-5})$ µs. The measurement of additional time delay is created in one channel (A7) with a delay generator. The additional time delay is measured with a function of the oscilloscope, so the error in reading is mini-

# of cables	bin # in TDC spectrum
1	2
2(+converter)	3
3	4
4(+converter)	4

Table 2.5: TDC test: number of delay cables and according TDC bin.

mized. The error is adjusted to the according scale range of the oscilloscope. The offset of 6.6 µs can be explained with additional electronics the signal has to pass. Because of that, another test has been done, to make sure that the delay of the stop signal is adequate and does not reach the TDC before the 200 µs window is provided. The four available flat ribbon delay cables are used serial to double, triple and quadruplicate the delay time in the connection between discriminator and TDC. Because of the connectors in between the cables, the polarity is changed when using an even number of cables. In this case, a short converter cable is added. The data acquisition is stopped before a cable is added. The test shows, that the self-trigger stop signal can be moved to higher bin numbers in the TDC time spectrum. One cable has approximately a delay of 0.13µs. This explains, why the change from three to four cables does not affect the hit bin in the TDC spectrum, since a bin has the width of 0.2 µs (see table 2.5).

A typical TDC time spectrum of a ^{252}Cf run in NERO standalone mode is shown in figure 2.20.

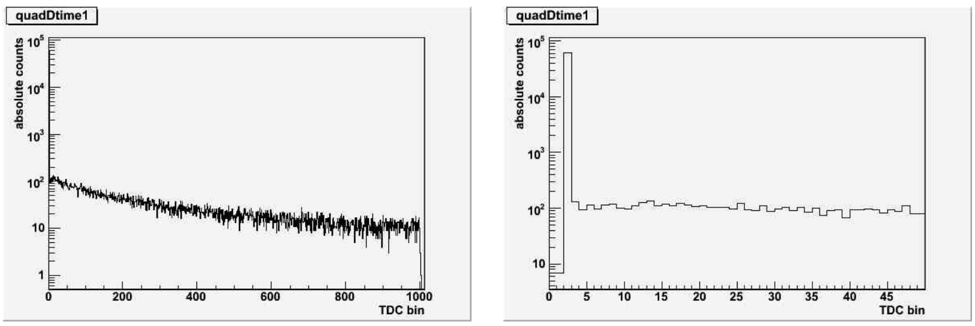

Figure 2.20: TDC time spectrum of a run with the ^{252}Cf source.

The left histogram in figure 2.20 shows the same data of TDC channel D1, like the right one, but is zoomed in. Bin 2 is the delayed start signal. Because of the multi-hit mode of the TDC, neutrons with longer moderation times from the same fission event are also recorded in higher bin numbers. In this case, the TDC probably has been started by another channel, but a neutron with a longer moderation time has been detected by the tube from which the data originate. In the left figure, a falling slope is observed, which can be explained with the moderation time (see sub chapter 2.7).

2.2.5 Electronics: C.A.E.N. Mod. V785 - ADC

Two 32- channel C.A.E.N. Analog-Digital-Converter Mod. V785 are used in the NERO setup to measure the deposit charge in the tubes. The signal is preamplified and shaped, before it is routed to the ADC. The common gate is provided by the NERO trigger logic and opens all channels for determining the charge within the gate width. Even, if only one proportional counter detects a neutron, all other 59 tubes are read, even if their signals (noise & low energy γs) are below threshold. There is one general gate, which is looped through the first ADC module to the second one. In addition to the correct software integration, some hardware settings can be done on board of the module. The signals from quad A and quad B are processed in $ADC_{VME\,slot\,9}$ and quad C and quad D in $ADC_{VME\,slot\,10}$.

The minimum gate-to-peak delay is $250\,ns$. The gate width has been set to approx. $39\,\mu s$. For comparison of energy spectra, the gate width should not be changed. If it has to be changed, the energy spectra might change.

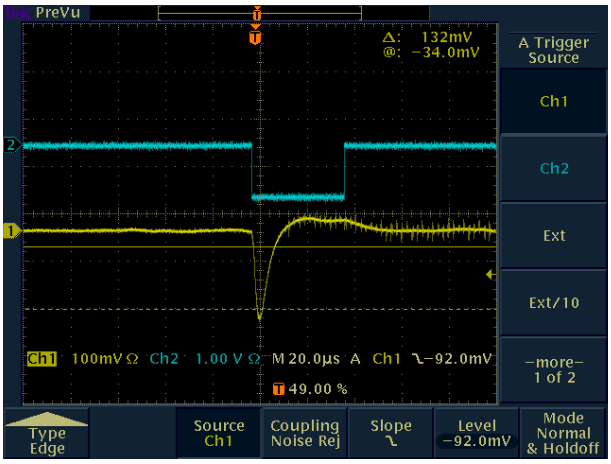

Figure 2.21: ADC gate and signal

The raw energy spectra for BF_3 and ^3He are shown in figure 2.22. Each quad (different rows) is represented by a ^3He (left column) and a BF_3 (right column) spectrum to highlight differences in gas types and quads.

^3He BF_3

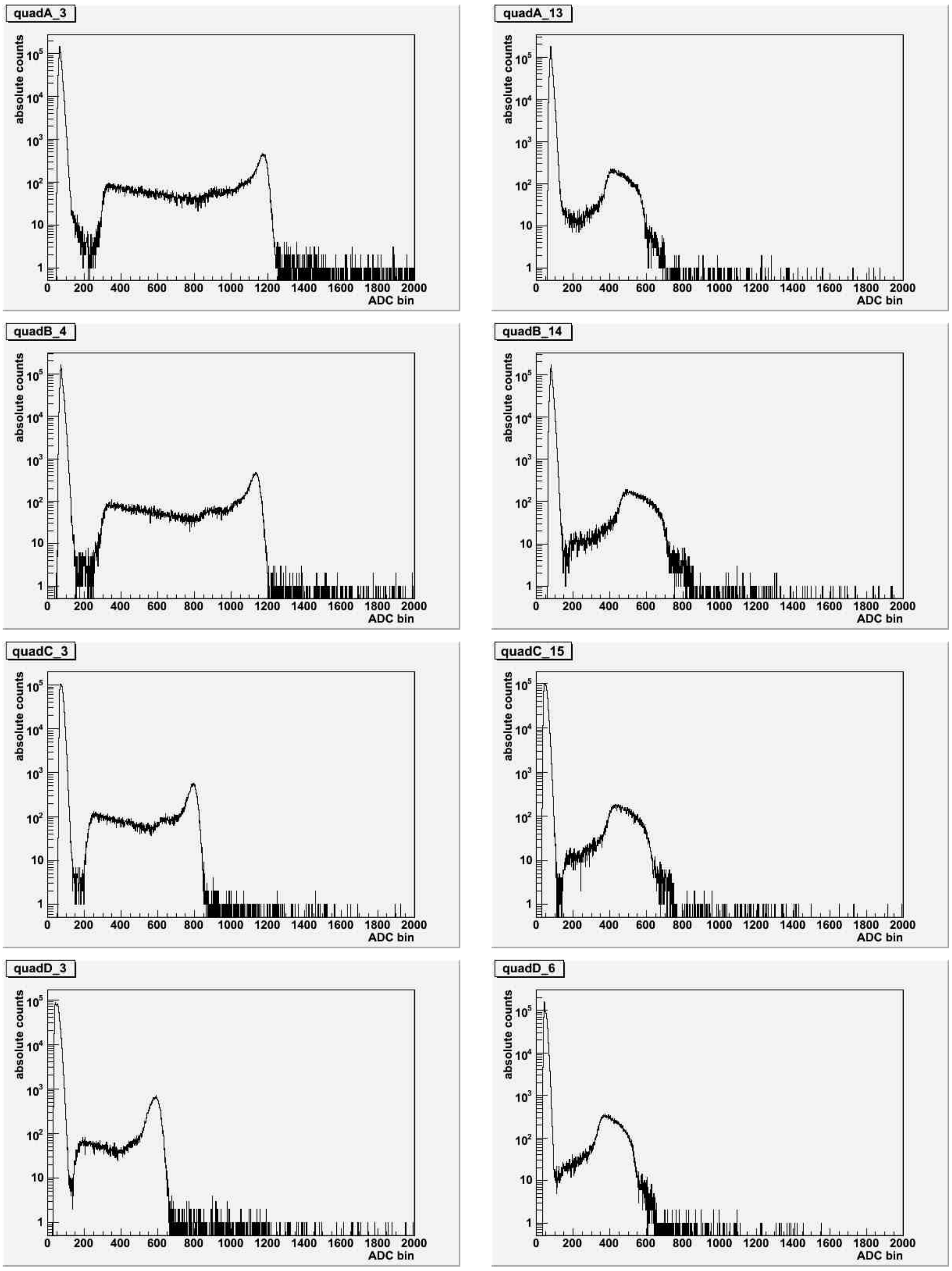

Figure 2.22: ADC raw spectra for a run with the ^{252}Cf source: ^3He (left) and BF_3 (right)

As figure 2.22 shows, there are differences between counter tube types and quads. Basically, in the energy spectra of ^3He tubes (see figure 2.22 (left)), the wall effect is better identifiable and noise / γ peak and neutron energy range is distinguished clearly. Also a nice peak of the maximum energy (hole energy of nuclear reaction is deposit in the counter tube) is identifiable.

Since the reaction of the neutron with ^{10}B ends in an excited state (6%) and the ground state (94%), one expects the full energy peak much broader and less sharp in figure 2.22 (right). The energy range of the neutron events can be identified in ^3He and BF_3 spectra. The change over from low energy noise/γs to neutron events is in the BF_3 spectra more difficult to distinguish than in the ^3He spectra. Events with a higher energy than the neutron energy range, are probably $\gamma + n$ pile-up events, or electronic noise (see sub chapter 2.5 - NERO background). The position of the maximum peak depends on different things. ^3He tubes in quad D are another type than those in quad A, B and C. Also the use of different high voltage sources (and values) can make an effect. Differences in gas purity and pressure are also an issue. Normally, one could compensate those effects with the gain in the shaper, but since all gains of shaper channels are set to maximum value (see sub chapter 2.2.2) this is not possible. On the other hand, it is not possible to increase the gap between noise peak and neutrons, anyway. The ADCs give a good information about the signals, and also about the background and noise. The noise/γ peak for low energy is an effect of the trigger logic. Because of the trigger logic, the CFD thresholds do not effect the energy spectra directly. Only counts, which are triggered by the tube itself are affected. If the CFD threshold is increased for one channel and it is looked to the raw data of the according ADC spectrum, it is possible to cut the neutron range which is created by the tube itself, but not suppress the low energy peak, triggered by other tubes.

2.2.6 Adjust NERO settings

After ADC gates are set properly (see sub chapter 2.2.5 - ADC), the most complex and time consuming settings are the CFD thresholds for all 60 channels. Basically, there are two ways to set the CFD thresholds.

1. Triggering the logic only to one counter tube. The best way to do this is to disconnect all discriminator ORs and connect the Master Gate with the discriminator test output of the observed channel. The channel of the discriminator test out can be set as described in 2.2.2. The noise peak, created by the trigger of other tubes will disappear and the threshold for the observed channel can be set without the influence of events in other tubes.

2. The TDC is started by an event in one of the 60 tubes. The delayed stop signal is only recorded in the corresponding TDC channel of the tube where the event is registered with a defined delay to the start signal. Because of that, the TDC provides the information, which ADC channel contains the energy information of the trigger signal. The electronics are read out event by event, where „event“ means the trigger of the logic and the following 200µs. The TDC operates in

multi-hit mode and is sensitive to stop signals during the following 200µs. The buffer, which is transferred to the computer contains the ADC information of all channels for the point of the detected start signal. Energies of signals in the following 200µs cannot be recorded by the ADC, but are registered in the TDC as a stop signal. SpecTcl (see sub chapter 2.3.5 – SpecTcl) is the NSCL data acquisition software and provides the function of gates. If the ADC energy spectrum is gated by the according TDC time spectrum of stop signals, one can observe the energy in each channel without triggers of other channels. Because the time delay of the triggering stop signal is known, it is possible to gate the ADC spectrum only on events, where this channel has triggered NERO. This procedure makes it possible to display the cut of the CFD threshold in each channel.

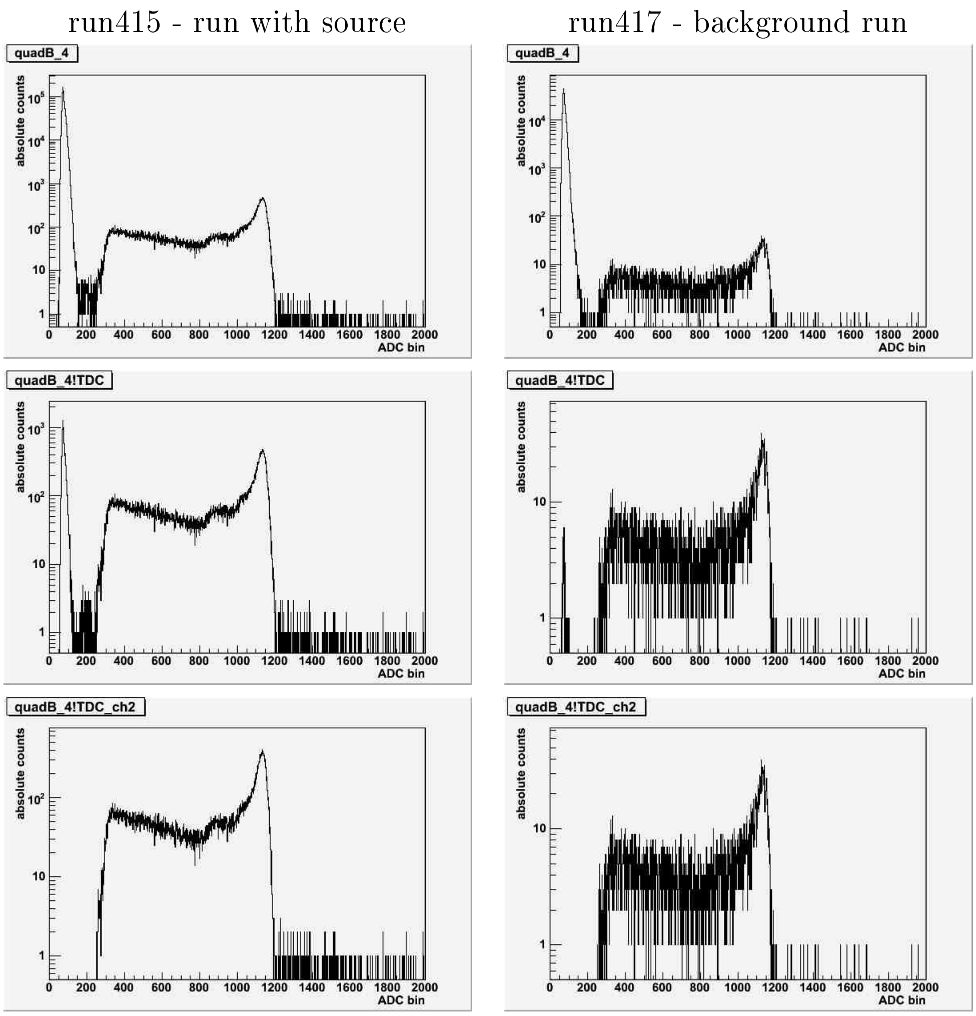

Figure 2.23: ADC spectra with source (left column) and background (right column), without gates (first row), gated by TDC_all (second row), gated by TDC_bin2 (third row)

For testing, method 1 has been used, but since method 2 has the advantage that it can be worked parallel with all channels, it is much more time efficient for setting the CFD thresholds. It is a task of multiple steps, because settings have to be checked, thresholds optimized and checked again until all thresholds are set satisfactorily.

Figure 2.23 shows ADC spectra with the different gates. Spectra in the third row show only events, which are triggered by the displayed channel.

2.3 DAQ / Software

2.3.1 Data Acquisition NSCL

The VME crate is connected via a fiber glass cable to a linux machine. The server (name: spdaq28) is part of the NSCL computer and network system. It can be reached from any place in the NSCL or from outside via Secure Shell protocol. The following programs and script languages are used:

- For the exchange of data between computer (spdaq28) and VME crate, the NSCL "Readout" software is used. Commands can be sent to the VME bus and data transferred to the computer.
- SpecTcl [Spe08] visuals experimental data in histograms and allows to analyze data with gates and other features.
- Tcl is a script language to manage data and procedures within SpecTcl.
- To monitor the rate and counts of the scaler modules, the NSCL scaler program is used.
- root [Roo08] is used for offline analysis of data. Plots and fits are done in root.
- bufdump [Buf08] is a program, which shows the data stream from the VME crate to the computer.

The lab computer is the important interface between experimental hardware and computer system of the NSCL. Anyway, the stored experimental data in NSCL is centralized. All mentioned programs are available in a common version and have to be adapted to the experimental requirements. The NSCL bluebook [Blu08] provides a lot of information how to modify the hardware and the software.

2.3.2 Readout

The Readout software provides the interface between the hardware (Crate, VME-modules,...) and the computer data acquisition. It works independently and separate from other programs, but it makes data accessible for other programs like SpecTcl. The NSCL Readout can operate in shell mode or in a GUI mode. The shell mode provides all basic functions like the starting or the stoping of a run. The GUI mode is more user friendly. Runs can be timed, recorded to the stage area and the data volume is monitored. Output messages are displayed and provide information about the status.

The ReadoutShell configuration file is stored in directory "/stagearea" with the name ".readoutconfig" and contains all necessary configurations.

The actual code of the readout program is found in "NEROSegment.cpp" in the readout directory. This code manages the buffer stream and the interaction with the hardware. All module functions can be controlled and timing of readout can be organized (see sub chapter 2.17 – I/O-Register). Available functions are provided in the "NSCL Device support software" documentation [Nsc08-1].

In addition to that, the data in the modules are read out and formed to the buffer stream, and afterward modules are cleared. The code also resets the NERO busy LATCH2 and the NERO standalone LATCH1 by setting bits in the I/O-Register. Those interventions into the hardware trigger logic assure the controlled data readout from all modules. Text outputs in the code appear in the output message window (see figure 2.24).

At the beginning of every run, the CFD thresholds and shaper gains are loaded from the init files (see sub chapter 2.2.2) and transferred to the modules.

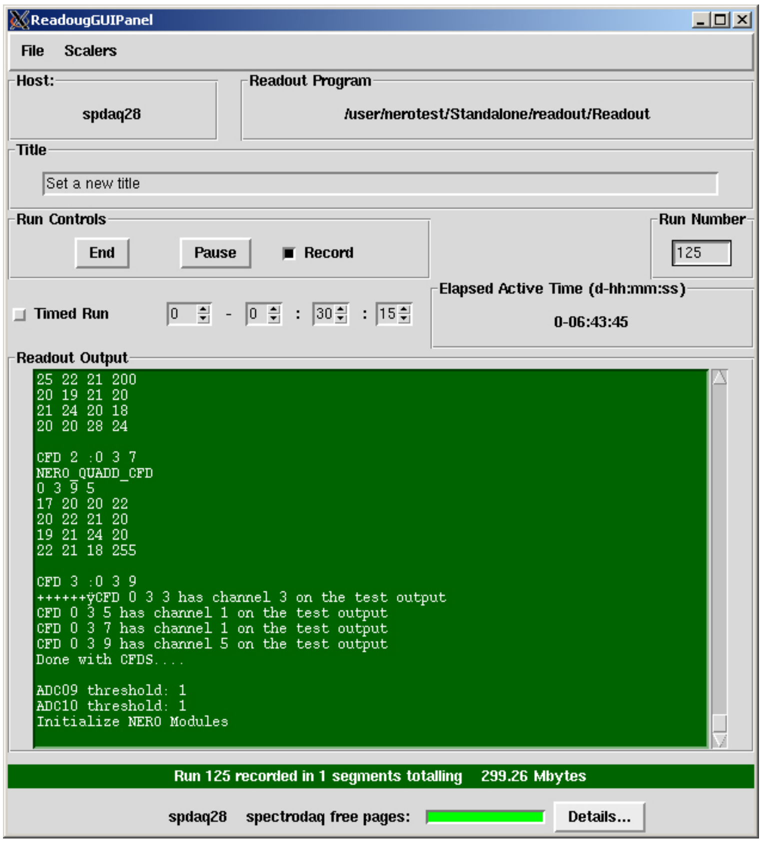

Figure 2.24: Readout GUI: The Readout program is responsible for sending and receiving data to VME / CAMAC bus and the control of the modules.

2.3.3 Buffer stream & bufdump

Bufdump

Bufdump is a program which dumps the buffer stream in real time to the screen. The console version just displays the running event stream. The program is located in "/usr/opt/daq/8.0/bin/bufdump".

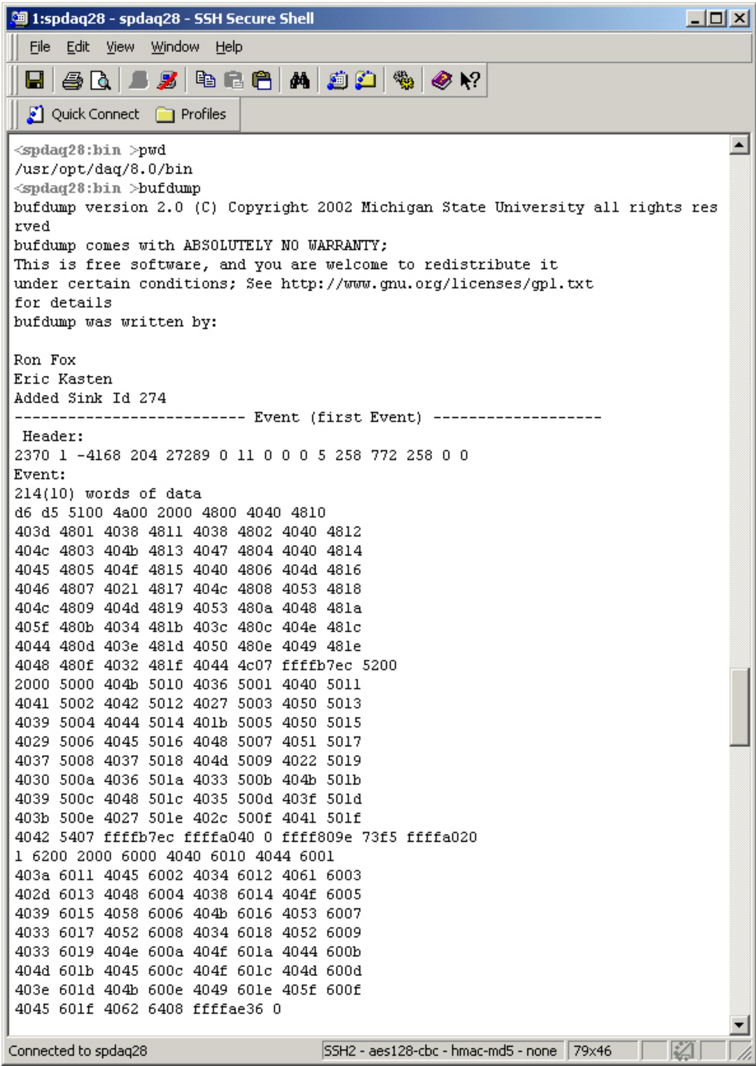

Figure 2.25: Bufdump in console

The program is very helpful, when the event stream is organized in the readout code. The structure must be defined well, so that other programs can read the stream in real time or from a record. A more convenient bufdump version is provided in the GUI version. It is located in "/usr/opt/utilities/current/bin/bufdump" and provides also filter and search functions.

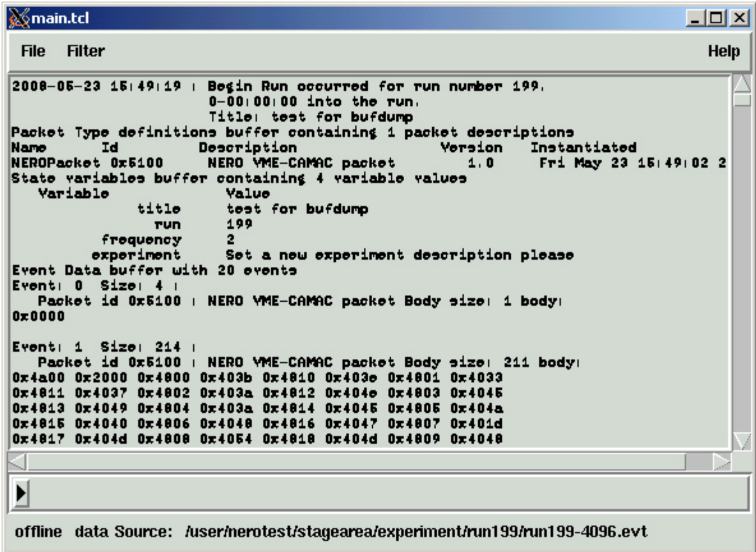

Figure 2.26: Bufdump GUI version with additional features

Buffer structure

Since Readout and the analysis programs are strictly separated, the buffer stream has to be organized in a defined structure to provide a common interface to other programs. This structure can be designed in “NEROSegment.cpp” (see sub chapter 2.3.2 – Readout). With the provided functions [Nsc08-1], words can be read and written in the VME modules. Since a QDC is added to the existing electronics (see sub chapter 3.3 - Active cosmic ray shield - electronics), the buffer stream had to be extended.

Data can be read from a VME module and put into the buffer stream. Data is provided in words (in NERO setup 2x16bit words), encoded in hex numbers with 4 characters. Depending, which module is looked at, the words are encoded in different ways. After the hex number is broken down to binary number system, each of the 32 bits has its meaning.

The buffer is organized in header and event. The event contains the data from the modules. Data of each module in the buffer are also introduced with a header, which contains information about the geographical address, the crate number and the number of converted channels. The actual data follows the header and is finished with an End-Of-Block (EOB) word, which contains an event counter.

As an example, the structure of 2x16bit words of the ADC is shown. The first five bits contain the geographical address of the module (related to slot number). The following three bits highlight, which kind of word is handled and how the remaining bits are organized.

type of word	
code	type
0 1 0	header word
0 0 0	data word
1 0 0	EOB word

Table 2.6: Type of word

31	30	29	28	27	26	25	24	23	22	21	20	19	18	17	16
GEO address					type of word			crate number							
15	14	13	12	11	10	9	8	7	6	5	4	3	2	1	0
0	0	number of converted channel						x	x	x	x	x	x	x	x

Table 2.7: *ADC Header:* Bits [23,16] contain the crate number, [13,8] the number of converted channels in the data block. This information provides the length of the data block [Cae08].

31	30	29	28	27	26	25	24	23	22	21	20	19	18	17	16
GEO address					type of word			0	0	0	channel				
15	14	13	12	11	10	9	8	7	6	5	4	3	2	1	0
x	x	ut	of	ADC data											

Table 2.8: *ADC Data word:* Bits [20,16] contain the number of the ADC channel, where the data is coming from. Bit 13 is the under threshold bit. It is set when the energy is below the internal threshold of the ADC. Bit 14 is the overflow bit. It is set when the energy is too high to be measured by the ADC. Bit [11,0] contain the actual energy information [Cae08].

31	30	29	28	27	26	25	24	23	22	21	20	19	18	17	16
GEO address					type of word			event counter							
15	14	13	12	11	10	9	8	7	6	5	4	3	2	1	0
event counter															

Table 2.9: *ADC EOB:* Bits [23,0] provide the number of the event counter [Cae08].

A single buffer output looks like the following (console output of bufdump):

—————————— Event (first Event) ——————————-
Header: 3960 1 -10726 197 308 0 27 0 0 0 5 258 772 258 0 0
Event: 146(10) words of data
92 91 51004a00 20004800 403a 4810
4045 4801 4035 4811 4040 4802 403e 4812
4057 4803 4044 4813 4051 4804 403f 4814
404d 4805 4048 4815 4048 4806 4046 4816
4050 4807 401e 4817 4057 4808 4053 4818
4056 4809 4046 4819 405a 480a 4041 481a
406a 480b 4034 481b 4044 480c 4047 481c
4050 480d 4037 481d 4058 480e 4044 481e
4052 480f 402c 481f 40444c00 1fef 5200
2000 5000 405f 5010 4048 5001 404e 5011
4051 5002 4055 5012 403d 5003 4062 5013
404a 5004 4058 5014 402a 5005 405c 5015
4036 5006 4054 5016 405a 5007 405c 5017
4043 5008 403a 5018 4060 5009 402f 5019
403c 500a 4044 501a 4041 500b 4058 501b
4046 500c 4055 501c 4044 500d 404c 501d
4046 500e 403c 501e 403e 500f 4041 501f
404c 5400 1fef ffff a040 0 94 3810 ffff a020
1 0

After the buffer header, the stream continues with the packet header.

- 92 (hex) represents the total number of words in the event data.
- 91 (hex) represents the total number of words in the packet. Since only one packet is used in this event, it is just one count less than the total number of words in the whole event.
- 5100 is the packet ID. In order to keep data acquisition organized, this packet ID is assigned by NSCL [NSC08-2].

After the packet header, the first data block from a module follows with the header information “4a00 2000” (magenta). As an example, this header is broken down to bin number system and can be interpreted as shown in table 2.10.

31	30	29	28	27	26	25	24	23	22	21	20	19	18	17	16
GEO address					type of word			crate number							
0	1	0	0	1	1	0	0	0	0	0	0	0	0	0	0
slot=9					header word			create=0							

15	14	13	12	11	10	9	8	7	6	5	4	3	2	1	0
0	0	Number of converted channels						x	x	x	x	x	x	x	x
0	0	1	0	0	0	0	0	0	0	0	0	0	0	0	0
0	0	converted channels=32						x	x	x	x	x	x	x	x

Table 2.10: Example 4a00 (top) 2000 (bottom): First row is bit#, second row is the meaning, third row is the word in binary system, fourth row is the converted information.

VME slot 9 contains one of the two 32ch ADCs, where quad A and quad B are connected to. Energy information for all 32 channels is following in the green marked data block of the next 32·2 16 bit words. The hex numbers can be encoded analog with the data word map. The sequence of the channels is alternating: ch0, ch16, ch1, ch17, ... ch15, ch31. The first ADC block ends with the EOF word “4c00 1fef”(magenta). Decoding the information gives the counts of events (=8175 in this case). The second ADC data block (blue: quad C and quad D) is following analogical and is embraced by header and EOF (magenta). Similar to the ADC, the TDC data are embraced by header and EOF (red). A map can be found in the TDC manual [Cae08-1]. The whole buffer event ends with “a” “0”. If a module is read which provides no data, the whole block of the module is substituted by the word “0”.

2.3.4 Scaler

Two 32- channel SIS VME scaler type 3820 [Sis08] are used to monitor the event rate of each tube in real time. The scaler program can be started with the command “/user/nerotest/Standalone/scalers/nerogoscaler”. Since the scalers are connected directly to the 16ch discriminator ECL outputs, the displayed numbers do not include dead time by trigger logic. In total 64 scaler channels are available. Only 60 channels are used by the NERO tubes, so the 4 remaining channels can be used to monitor rates of Master Gate, Master Gate live and coincidences in the scintillators of the active cosmic ray shield (see chapter 3). A special adapter cable allows to loop-in the additional channels to the 16- channel connectors. Because the scaler processes only ECL signals, the NIM signals from trigger logic are converted to ECL. If a run is recorded by the readout software, a scaler file is saved to the scaler directory. It contains start-/end-time and date of the run, runtime and scaler data. The scaler program must be started to save the scaler data to the file. The scaler data serve as a quick reference, if NERO works satisfactory.

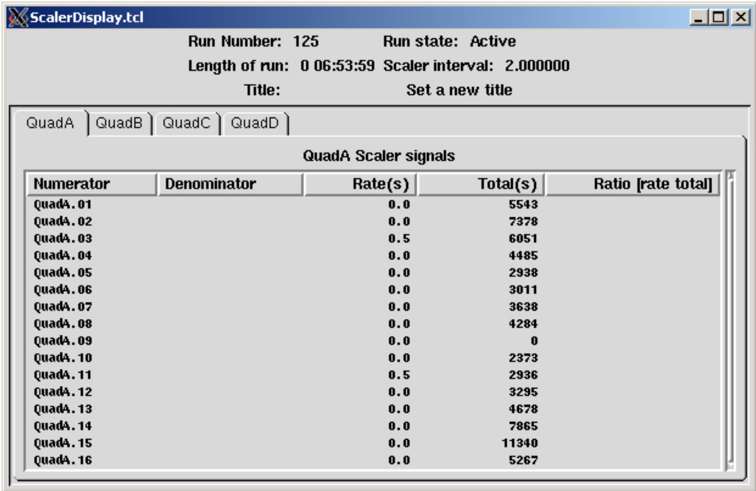

Figure 2.27: Scaler GUI

2.3.5 SpecTcl & TkCon

SpecTcl is a powerful NSCL analyzing tool and is started with the command "/user/nerotest/Standalone/specTcl/SpecTcl". The program is attached online or to recorded data. Different spectra can be displayed and gated on other data. SpecTcl starts with four windows [Spe08].

SpecTcl	Control window. Attaching and clearing spectra. (figure 2.28)
TreeParameter	definition of spectra and gates (figure 2.30)
Xamine	display of spectra (figure 2.29)
TKCon	console to run specific commands or scripts (figure 2.31)

The use of SpecTcl in its basic functions is self-explanatory. Spectra and variables have to be defined and the buffer structure implemented. Parameters are declared in the file "Parameters.h" and the buffer structure is encoded in "Unpacker.cpp". After editing, a new executable SpecTcl file has to be compiled.

Xamine can display multiple spectra at once. Automatic data update function, zoom, gates and integrate functions with user defined borders are available features. All settings can be saved and reloaded. The TreeParameter window allows then to create spectra from variables (which are filled with buffer data), or create gated histograms with existing gates. All settings can be saved to a file and also edited in a common editor, that might be more convenient.

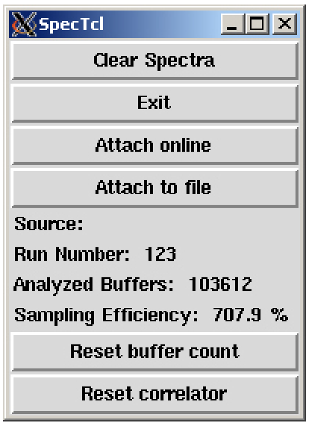

Figure 2.28: SpecTcl: The analysis program can be attached to an online run or to recorded data.

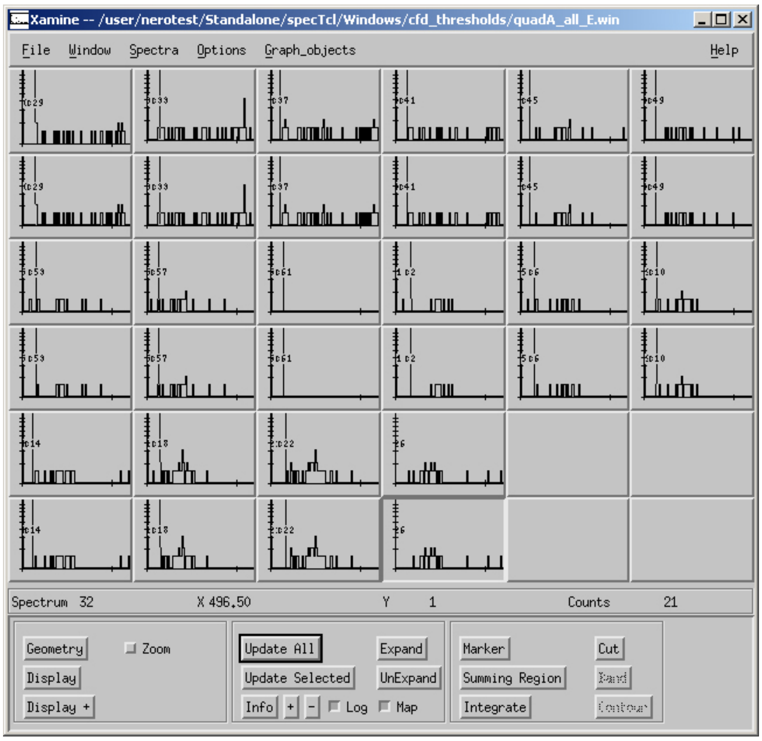

Figure 2.29: Xamine: Multiple spectra can be displayed. The displayed spectra in this figure have no importance.

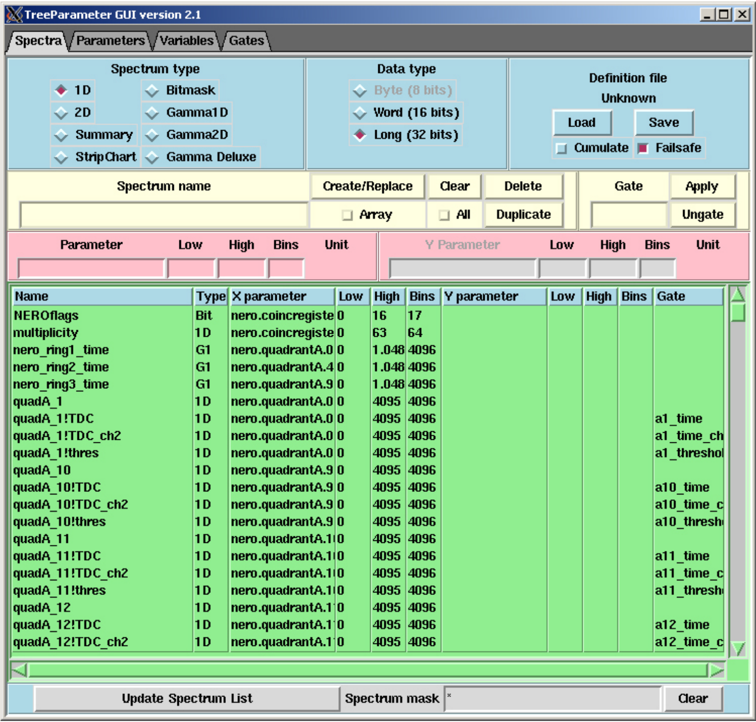

Figure 2.30: TreeParameter: Parameters, spectra and gates can be organized.

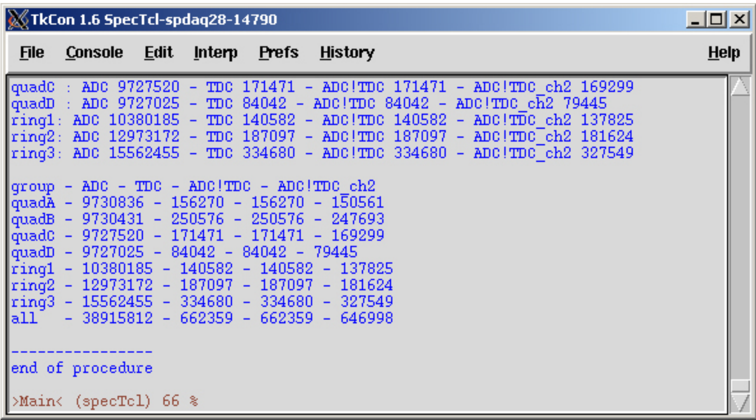

Figure 2.31: TKCon: Tcl scripts and commands can be executed.

Tcl scripts in SpecTcl:

SpecTcl is based on the script language tcl. The TKCon console (figure 2.31) allows to load tcl-scripts or give direct commands. Basically all operations, which can be done with one of the other windows can be substituted by a command in the TKCon window. Since raw data of runs require much storage space and take a lot of time to load, some tcl-scripts have been programed which save all available spectra to ASCII files. Because of that, it is possible to document almost any run, which is done during this Diploma thesis with a minimized use of storage. With a small sequence of tcl commands, a separated directory is created with all available histograms of the loaded run. Each spectrum is saved to a separate file and can be read by root. In addition to that a file is created with a summery of information like integrals of special groups (quads, rings) of spectra. The scripts are located in "/user/nerotest/Standalone/specTcl/TclScripts/" and their use is explained in the according readme files.

2.3.6 Root

Root is an object oriented program environment for different requirements of experimental physics and is developed by CERN. Main missions are data acquisition and analysis [Roo08]. The program language is compatible to c++, which makes the learning process easy. There are also plenty tutorials available which highlight the basic functions much better than the official root Internet presence [Roo08-1]. Several scripts are programed to plot background data, correct data, calculate efficiencies and fit histograms. Most scripts can be used for different runs without modification, as long as the spectra are saved to ASCII files using tcl-scripts (see sub chapter 2.31 – SpecTcl).

2.4 ^{252}Cf source

For the tests of NERO a ^{252}Cf source was used. The NSCL source with the ship# Z7153 is calibrated and had an activity of 50µCi at the 11/19/1990. The ^{252}Cf itself is mounted on a fission foil holder and is quite handy. The active diameter of the foil is $5mm$ and is covered with 50µg Au. ^{252}Cf decays by α emission (96.91%) and spontaneous fission (3.09%). The half-life over all decays is 2.645 years [Kno00]. The emitted neutrons come with the fission process.

Fission products of ^{252}Cf

The peaks of the asymmetric mass distribution of the fission products are in the range from ^{105}Rh – ^{113}Ag (fission yield>3%) and ^{135}Xe – ^{147}Nd (fission yield>3%) [Ner60].

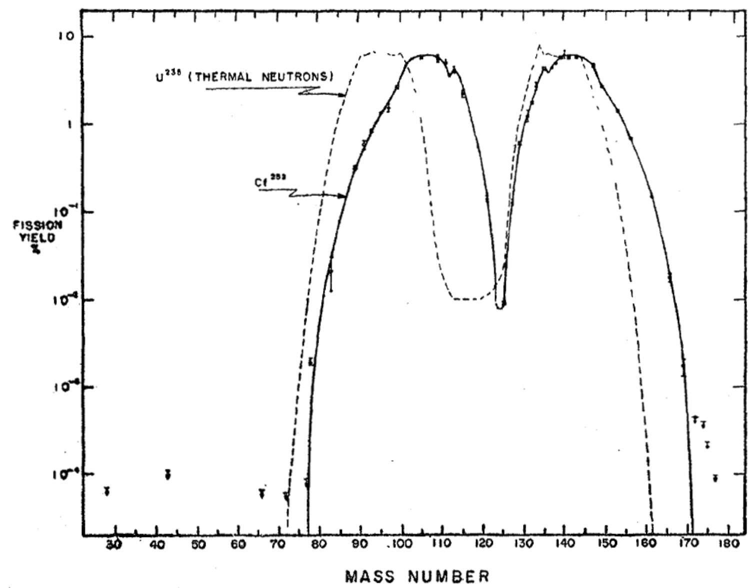

Figure 2.32: Measured spontaneous fission yield as a function of mass number products of ^{252}Cf in comparison to ^{238}U [Ner60].

The fission products are interesting, since excited states can emit γs after neutron emission to reach the ground state. These γs are correlated to the neutron emission and can be used for moderation time measurements with γs as a start and neutrons as a stop signal.

Every fission event produces up to six neutrons and 3.7676 ± 0.0047 neutrons on average [Rei08]. The neutron energy spectrum is shown in figure 2.33.

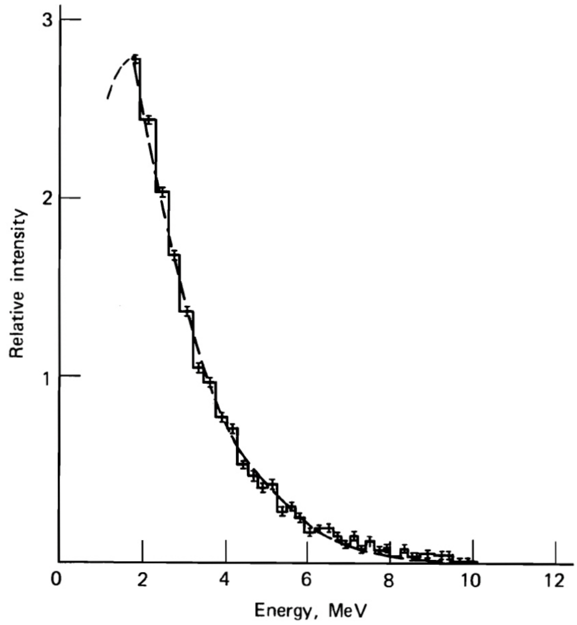

Figure 2.33: Measured ^{252}Cf neutron energy spectrum from spontaneous fission [Kno00].

The neutrons have an average energy of $2.1\,MeV$, but the most probable energy is $0.7\,MeV$ [Mar99]. The calibrated ^{252}Cf source is used for the efficiency measurements of the NERO detector. Since the efficiency is dependent on the energy of the neutrons, the neutron energy spectrum of ^{252}Cf has to be considered.

The present neutron emission rate can be calculated by the equation of an exponential decay. No error for the activity of the used source is specified. Hence an uncertainty of 5% is assumed [Hos05]. The neutron activity is given by:

$$A_{neutron} = A_0\,[1/s] \cdot 3.77\,\frac{neutrons}{fission} \cdot 0.039\,\frac{fission}{1} \cdot e^{\frac{-ln2 \cdot t}{t_{1/2}}}$$

With each fission event, prompt γs are emitted. The total gamma energy is about $6.95 \pm 0.3\,MeV$. The average number of gammas is 7.98 ± 0.4 with an average energy of $0.87 \pm 0.02\,MeV$ [Val99].

The prompt gamma multiplicity distribution can be described with different models and is shown in figure 2.34.

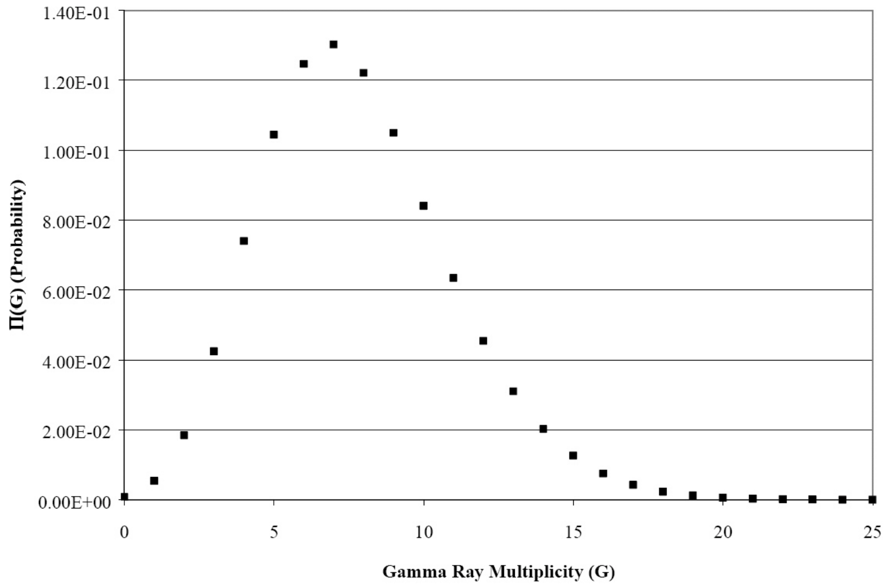

Figure 2.34: ^{252}Cf - γ multiplicity [Val99].

In addition to the γ activity induced by fissions, the γ spectrum of ^{252}Cf is characterized by the daughter products of the α-decay sequence, which dominates the decay of ^{252}Cf. Several peaks can be assigned to nuclei.

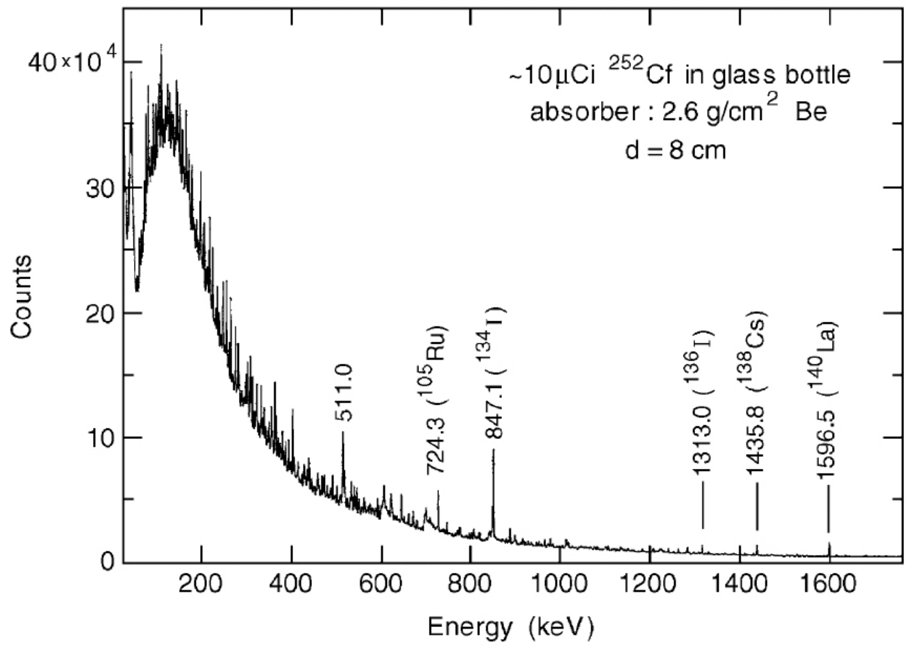

Figure 2.35: γ- ray spectrum of ^{252}Cf measured with a Ge detector by Ahmad et al. [Ahm03].

2.5 NERO background

The experiment with NERO in 2002 has shown [Hos05-1], that the rate of stopped nuclei of interest, is very low. Therefore, it is essential to keep the background rate as low as possible. NERO has been calibrated at the Notre Dame Nuclear Structure Laboratory. A background rate of $15 - 20\,s^{-1}$ has been measured, when the detector was shielded by water jugs. Later in the NSCL vault, no water jugs have been used, but the background rate without water shielding was as low as $5\,s^{-1}$ [Hos05].

After the mentioned experiment at the NSCL [Hos05-1], NERO has been moved to lab108 and shielded by water jacks from one side. Basically two rows of water canisters separate NERO from the rest of the room.

Figure 2.36: At the beginning of this thesis: NERO is shielded by two ranks of water canisters. The detector is located behind the white water canisters.

Water does not stop neutrons. It just moderates and scatters them. Neutrons hit the hydrogen nuclei of the water molecule and loose energy by these collisions. Shielding against neutrons is only possible, if they are moderated and captured. Materials with large neutron capture cross sections are necessary to capture neutrons, after they are moderated. In the past, boron carbide has been used to shield NERO but no positive effect has been observed.

During the work of this thesis, two research groups were in lab 108 and both handled ^{252}Cf sources. The presence of the other source can be detected with NERO.

The first section of this chapter just considers the scaler rates which monitor the CFD signals from each tube. With neutron sources of both groups in the source safe and water shielding, the NERO background rate is around $20 - 25\,s^{-1}$. Without any sources in lab 108 or its neighboring rooms, the background rate decreases to $5 - 10\,s^{-1}$.

The effect of water shielding could be observed, when five additional canisters were placed between the sources of both groups and NERO. The rate decreased to $10\,s^{-1}$. The neutrons are scattered and the direct irradiation is reduced. But it is not possible to shield NERO with 7 rows of water canisters in any direction.

With the preparation of the active cosmic ray shield, some equipment in the laboratory has been removed because of limited space. During this process, all water canisters have been removed from the lab. Without water shielding and after reassembling NERO, the background rate increased up to $40\,s^{-1}$, when both neutron sources were present in the room. In figure 2.37 (run277) it can be observed, on which side of NERO the sources are located, when rates of each tube positions are compared (see figure 2.2).

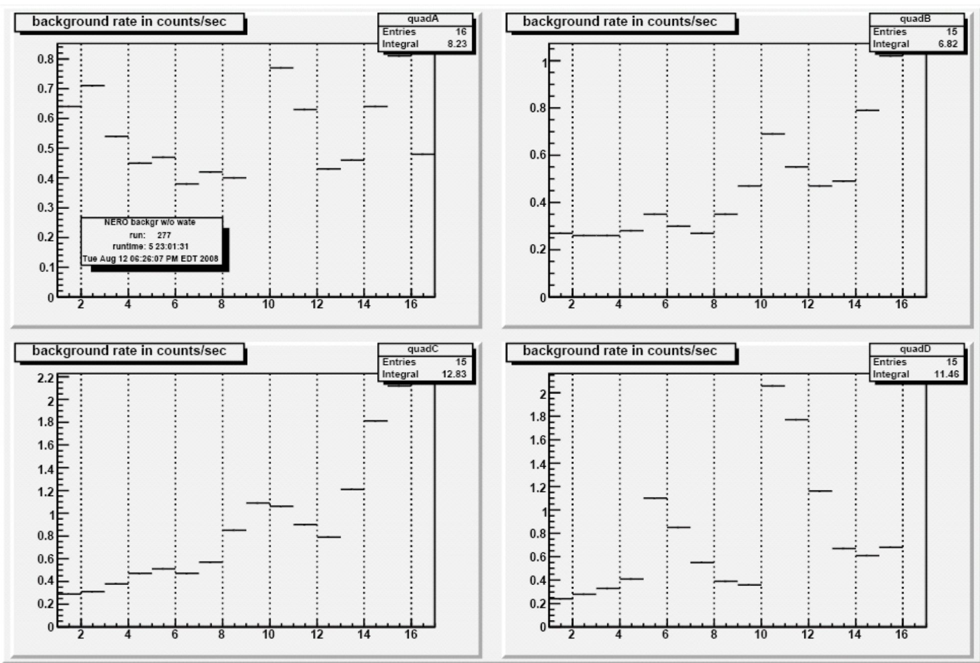

Figure 2.37: Run277: $rate = 39.34 \pm 0.03\frac{1}{s}$. The scaler data show the background rates for different quads and tubes after removing water canisters from the lab and with both neutron sources in the room. Tube A9 is routed to channel A16. Obviously, quad C and quad D face the ^{252}Cf sources. The tube positions C12 - C15 and D13 - D10 are the closest positions to the sources. Errors are smaller than the last digit.

Besides the environmental influence to NERO like natural radiation, cosmic showers or radiation sources in the laboratory, which cause events in the detector, there are also some other sources of background. The scalers just count the logical signals from the CFDs for all 60 tubes. On one side, there are noisy electronic parts in the setup. For example, quad A has a higher background rate than quad B, quad C and quad D together. That can be ascribed to the preamplifier box and/or the high voltage power supply of quad A. Figure 2.38 shows scaler data of background with minimized environmental influence, which means that all sources have been removed from lab108.

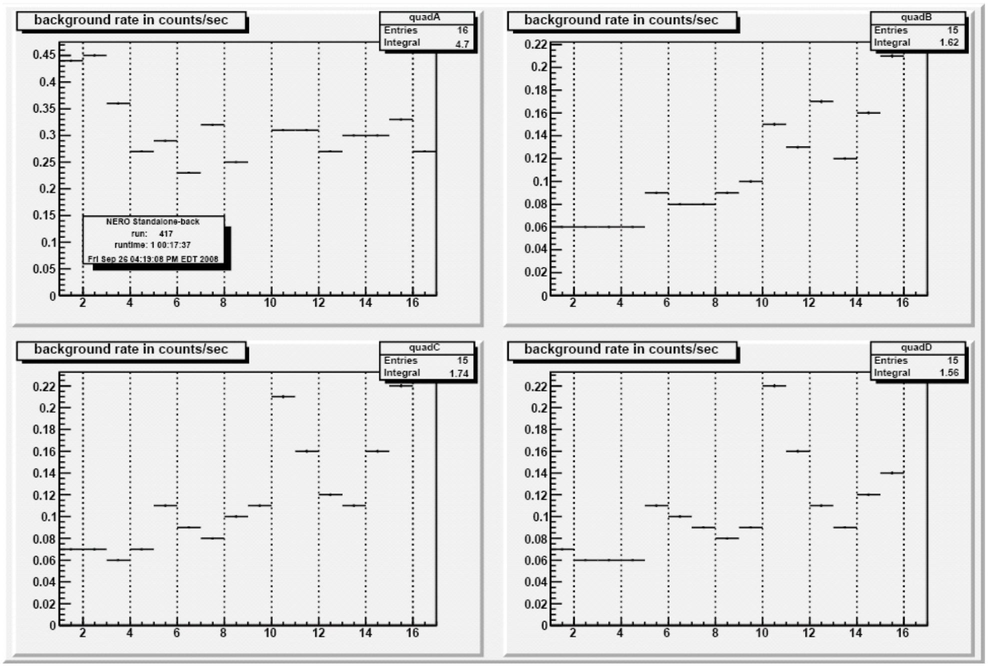

Figure 2.38: Run417: $rate = 9.62 \pm 0.01\frac{1}{s}$. Background run without the water shielding and the neutron sources in the lab. Tube A9 is routed to channel A16. The scaler rate for quad A is almost as high as the sum of quads B, C and D.

Neutron events caused by environment and other background / noise can be identified in the energy spectra. Because of the wall effects, energies of neutron events are in a defined range. Events with energies outside of this range cannot be caused by neutrons. On physical side, $n + \gamma$-pile up events might be candidates.

Rates of background and noise around $10\,s^{-1}$ are common rates for the NERO detector in the standalone mode.

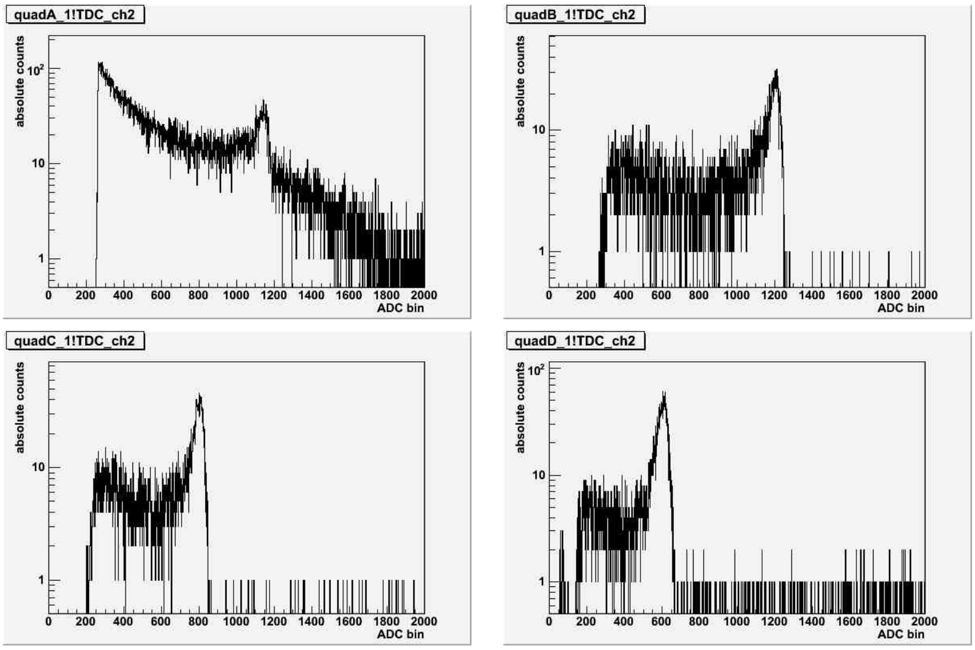

Figure 2.39: Run417: Background energy spectra of ^4He-tubes, gated on the self-trigger bin in the TDC. Tube A1 (top, left), tube B1 (top, right), tube C1 (bottom, left), tube D1 (bottom, right) are shown.

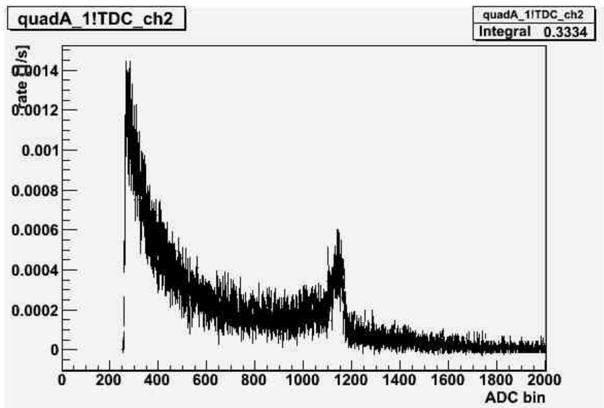

Figure 2.40: Run417: Energy spectrum gated on self-trigger bin of TDC of tube A1 (^3He) with linear axis. Quad A energy spectra show a noise underground.

Figure 2.39 shows the background energy spectra of channel A1, B1, C1 and D1 (all ^3He). The energy range of neutron events can be identified in all four spectra. Most events in B1, C1 and D1 are caused by real neutron detection. Few events with higher energies might be caused by $n + \gamma$-pile up events. Tube B1 and tube C1 are the same model, whereas D1 is a different model of ^3He counter (see table 2.1). The energy spectrum of A1 is different. The integral of the spectrum is much higher and also events with higher energies are more numerous. When comparing the spectrum from the tube A1 with the other spectra, it looks like the sum of real neutron events and an exponential slope of noise underground. Figure 2.40 shows the histogram of channel A1 with linear y-axis.

Just the fact, that the spectra of other quads do not show the same exponential underground demonstrates that there is probably no physical cause of this shape. Low energy charged particles would be stopped in the ceilings of the building. If there are particles with higher energies, all tubes should detect them. This shape can only be explained with electronic noise. Quad A is the quad with the most noise – especially in the ^3He counters. For comparison, figure 2.41 shows the energy spectra of BF_3 counters. The energy spectra of this detector type do not look as nice as the ^3He counters in general (see sub chapter 2.1.3 - counter tubes).

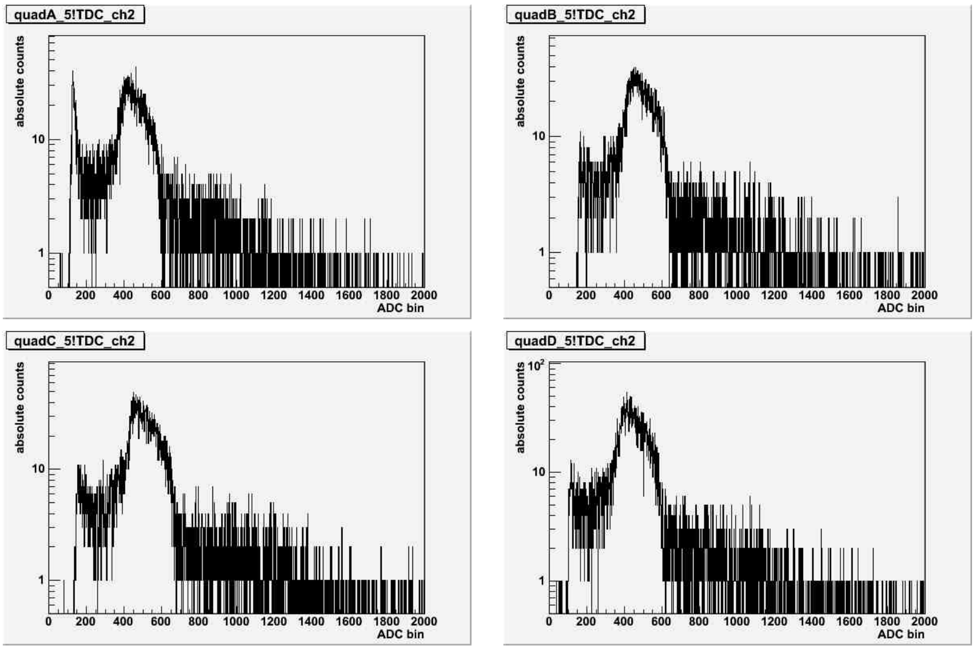

Figure 2.41: Run417: Background energy spectra of BF_3 tubes.

It also has been observed, that noise can induce signals in neighboring channels. Probably that happens, when the grounding is not clean. Nevertheless there are always issues, which can be improved like cables and connectors. One shortened channel in a broken flat ribbon cable caused a rate of about 30000 $\frac{1}{s}$ in all channels.

Basically, absolute background rates of 10 s^{-1} can be achieved, but to obtain lower rates it takes a lot of time to tune NERO. The lowest measured background rate of NERO between January and September has been around 5 s^{-1} (run122, 04/29/2008).

In preparation of the active cosmic ray shield, NERO has been lifted on a rack to provide space under NERO for a scintillator. After reassembling of NERO, the rate had increased to about 10 s^{-1}.

There were different efforts to reduce noisy channels, and not all of them have been successful. Fixing connectors and cables helped to reduce the background rate in individual channels (reflections). Changing tube positions or connect a tube to another preamplifier box helped to figure out where the search for the source of noise has to be continued. Exchanging two quads in the shaper input exchanged the complete shape of the background scaler plots for the noisy quad A. Of course the CFD thresholds are different, but nevertheless this is a hint to the location of the noise source in quad A. Somewhere between counter tubes and shaper input. The preamplifier box of quad A is probably the source of the noise.

As described in sub chapter 2.2.1, the preamplifier circuits are just plugged in and can easily be replaced. Few circuits are in spare, so the broken ones can be replaced. At the beginning, some channels were dead and have been routed to the spare channel 16. A relict of this acting is tube A9, which is routed to channel A16. This has to be considered, when it is looked to scaler data in figure 2.37.

Since TDC and scalers are connected with the same cables, the TDC records the same noise, like the scalers. If cables or connectors are broken, reflections can occur and multiply the rate in the scaler and the TDC. In the TDC time spectra, the delay of the reflections can cause an alternating structure.

2.6 NERO efficiency

In order to estimate the efficiency of NERO, a calibrated ^{252}Cf neutron source (see sub chapter 2.4 – ^{252}Cf source) is used. Of course, the neutron efficiency depends on the energy of the neutrons, which have to be measured.

For an efficiency measurement, a background run and a run with the ^{252}Cf source in NERO were done. The covered solid angle by the detector changes, when the source is moved along the beam axis in NERO. This is reflected by the efficiency measurements, depending on the ^{252}Cf position in NERO. Hence the source should be located in the middle of NERO to achieve best efficiency. Since the scaler data show the real number of events, channel by channel, these rates are used to determine the efficiency. The scaler data of the run with the source are background corrected to determine the efficiency. This is done by a root script, which calculates the efficiency for every channel, quad, ring and the whole detector.

The efficiency is calculated, depending on the position of the ^{252}Cf source along the beam line axis in NERO. The detector has a length of $80cm$, so the center is in $40cm$ distance to the front plane.

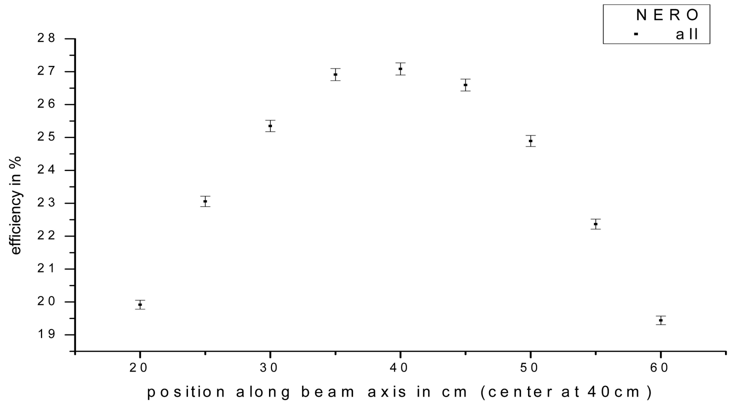

Figure 2.42: Absolute NERO efficiency for different positions of the ^{252}Cf source along the beam axis. Center at $40cm$.

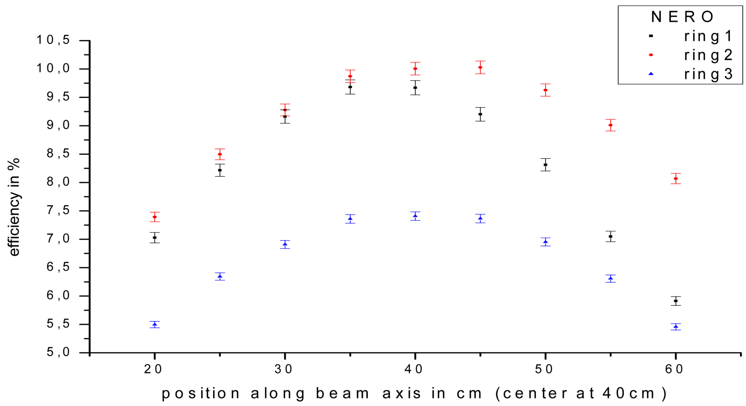

Figure 2.43: NERO efficiency for different positions of the ^{252}Cf source along beam axis grouped by rings. Center at $40cm$.

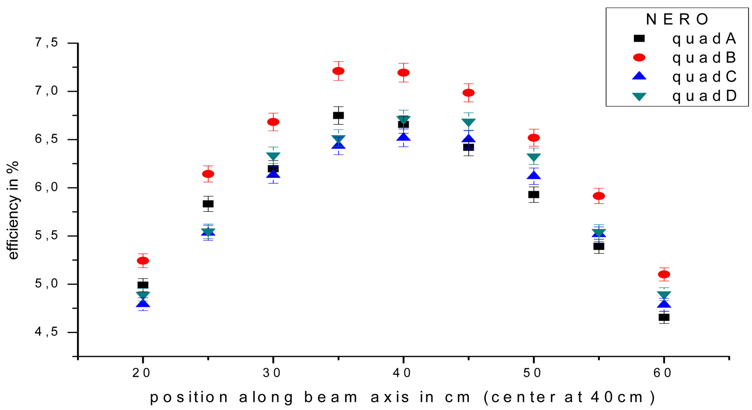

Figure 2.44: NERO efficiency for different positions of the ^{252}Cf source along beam axis grouped by quads. Center at $40cm$.

As expected, figure 2.42 shows the total efficiency maximum value of 27.08 ± 0.19 % at $40cm$ along the beam axis. The asymmetry can be analyzed, when looking to the efficiency, grouped in rings (see figure 2.43) and quads (see figure 2.44). Ring 1 (^3He tubes) decreases more than other rings in efficiency for larger distances to the front plane. But on the other hand, the efficiency of ring 2 is higher for larger distances. ^3He counter tubes are shorter, and have to be pulled into the borehole with the cable, or carefully with a stick. Since these measurements have been done at the beginning of the work with NERO, where the detector has not been reassembled yet, it is possible, that the tubes were not in their correct positions in beam axis. But even with this uncertainty, effects are balanced and the maximum of efficiency is in the middle position of the beam line axis in the detector.

To monitor the condition of the detector, efficiency measurements are done after major works at the NERO detector and are done as quoted in table 2.11.

date	efficiency [%]
Ph.D. Thesis Hosmer	26.4 ± 1.5
04/08/2008	27.08 ± 0.19
04/18/2008	27.90 ± 0.19
04/29/2008	27.73 ± 0.19
05/06/2008	27.70 ± 0.19
06/05/2008	27.46 ± 0.19
07/17/2008	27.55 ± 0.19
09/27/2008	27.88 ± 0.19

Table 2.11: NERO efficiencies

The first value is taken from [Hos05] for comparison. For the errors, the activity error in 1990 of the ^{252}Cf source was estimated to 5% [Hos05]. All other errors are estimated from literature (see sub chapter 2.4). Since no error calculation can be followed for the value by Hosmer, it cannot be explained, why the dimension of errors differs by one order of magnitude. But in any case, it is found that the efficiency is almost constant with a weak increasing drift. The latest data from 09/27/2008 are shown in table 2.12.

group	efficiency [%]
NERO all	27.878 ± 0.189
quad A	6.904 ± 0.094
quad B	7.287 ± 0.098
quad C	7.192 ± 0.097
quad D	6.496 ± 0.088
ring 1 (^3He)	10.427 ± 0.131
ring 2(BF_3)	10.038 ± 0.113
ring 3 (BF_3)	7.413 ± 0.076

Table 2.12: NERO efficiency 09/27/2008

The efficiency of quad D is the smallest, compared to other quads. This might be an effect of the shorter active volume of the ^3He counter tubes (see sub chapter 2.1.3 – counter tubes). It is also interesting, that the inner ring 1 (^3He) has the highest absolute efficiency. As described in 2.1.3, this gives an idea of the energy spectrum of the detected neutrons from the ^{252}Cf source. Low energy neutrons are moderated preferentially in shorter times and distances in polyethylene, than high energy neutrons. Simplified, neutrons of low energy are preferentially detected in the inner ring and neutrons of higher energy in the outer rings. The efficiency of quad A is also a little bit lower. This might come from the higher background rate.

In principle, the efficiency of the detector is given by its design. Number and distances of tubes, materials and components used affect the efficiency mainly. Of course, changing tubes or improving the electronics has an influence on the detector, too. Because of that, the efficiency and background of the NERO detector is monitored during exchanges of components or reassembling. Before reassembling the $60 \cdot 60 \cdot 80cm$ polyethylene detector on a rack for the active cosmic ray shield, it was located on a polyethylene platform of approx. $27cm$ height and the same area like the detector ($60{\cdot}80cm^2$). Of course that (and also other materials in the lab like water) can moderate and back-scatter neutrons, too. The polyethylene platform is removed after 05/07/2008. The water canisters are removed after 08/07/2008. No significant change in efficiency has been observed (see table 2.11).

2.7 NERO neutron moderation time measurement

As a consequence of the neutron emission by the ^{252}Cf source, coincident γs are emitted (see sub chapter 2.4 ^{252}Cf - source). The principle of NERO is to moderate neutrons in one step, and to detect the products of nuclear reactions of evidence in the counter tubes in a second step. In experiment, it must be known how much time passes between emission and detection of the neutron. Because of that, one is interested to measure the moderation time.

In addition to the experimental interest, the moderation time has to be known for considerations of the active cosmic ray shield (see chapter 3). The idea is to detect charged particles and γs of cosmic showers, which also contain neutrons that produce a neutron background in NERO. In order to know for which time the veto has to block the neutron detector, the moderation time of the neutrons must be known. Of course, energies are different (between cosmic neutrons and ^{252}Cf fission neutrons), but this is discussed in chapter 3.

For a time measurement, a start and a stop signal are needed. Since there are more γs detected than (by moderation) delayed neutrons, one still wants to use the NERO neutron detection as a start signal to decrease background in the measurement. The γs are detected fast with a scintillator. The neutrons are detected after the varying moderation time with NERO. Each fission event creates up to 20 γs with a total energy of $6.95 \pm 0.3\,MeV$ and an average energy of $0.87 \pm 0.02\,MeV$. An average number of 7.98 ± 0.4 γs is emitted with every fission event (see sub chapter 2.4 - ^{252}Cf and [Val99]). To realize the intention to use neutrons as start and γs as stop, the signal from the scintillator has to be delayed for clearly more than the moderation time. The respective setup is shown in figure 2.46.

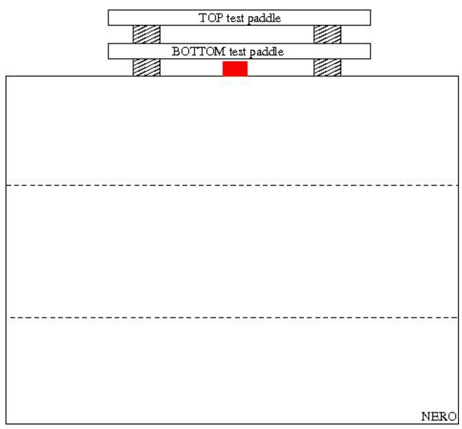

Figure 2.45: Run249. Arrangement for moderation time measurement. ^{252}Cf- source on top of NERO. Only one scintillator is used to provide the γ stop signals to the TDC.

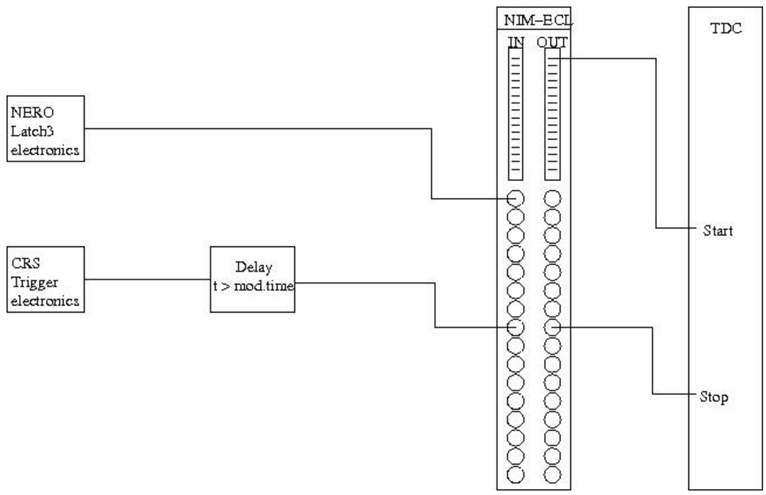

Figure 2.46: Setup for moderation time measurement. ^{252}Cf- source on top of NERO.

The NERO standalone mode has been modified slightly. The 60ch TDC stop signals are removed and the scintillator's CFD signal is looped into one TDC stop input. The electronics of the scintillator are explained in sub chapter 3.3. The scintillator's CFD signal is delayed with a Gate&Delay generator for about 400µs. Because the TDC works with ECL signals, the TDC start gate and the stop signal have to be converted in an ECL-NIM-ECL converter. The schematic setup is shown in figure 2.46. The measured time spectrum shows the moderation time inverted. If a moderation time is short, the measured time in the TDC will be long. If a moderation time is long, the TDC will measure a short time (see figure 2.47 for illustration).

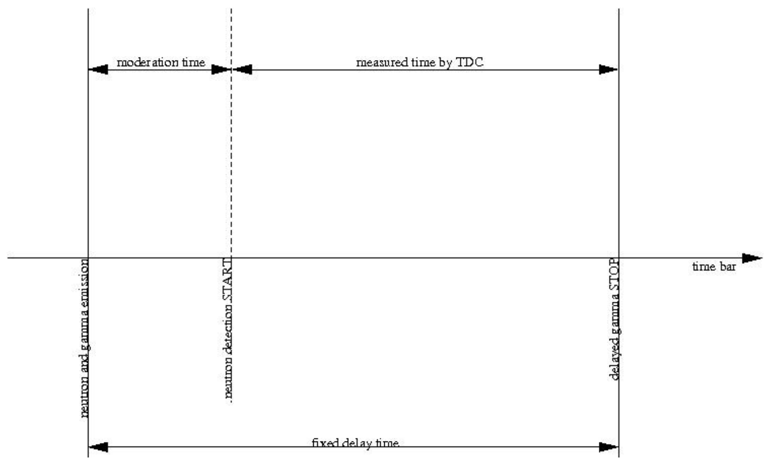

Figure 2.47: Measurement of moderation time: The TDC measures a time, which is given by $t_{TDC} = t_{fixed\,delay\,of\,\gamma s} - t_{moderation-time}$.

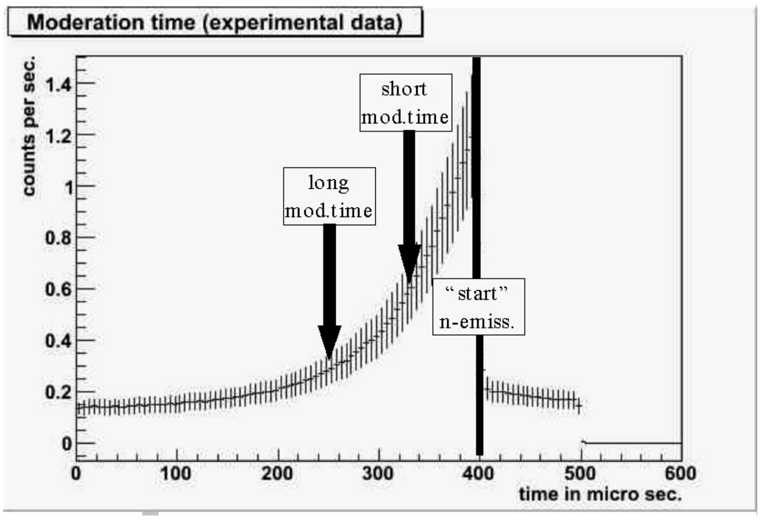

Figure 2.48: Moderation time measurement in run249 - experimental data. As described in figure 2.47, the TDC measures the moderation time indirect.

The cutoff after 500 µs in the histogram of figure 2.48 is created by the TDC gate. This has been adjusted for this measurement to 500 µs, which corresponds to TDC bin 2500, where each TDC bin has a width of about 0.2 µs (see sub chapter 2.2.4). In the histograms, a bin width of 5 µs has been set. The drop after 400 µs is related to the delay of the γ stop signal. The offset between 400 µs and 500 µs is neutron background, which is not related to the neutron emission of the ^{252}Cf- source. The same offset can be found for very short TDC times (corresponding to long moderation times).

The shape of the histogram is fitted with an exponential function.This makes sense, since collisions between neutrons and hydrogen in the moderator are a statistical process and the probability of each collision has to be multiplied.

The relative amount of moderated neutrons is given by the ratio of the sub-area to the total area under the exponential function. The offset has to be discarded, because the γ- background is not related to the neutron emission and would distort the ratio.

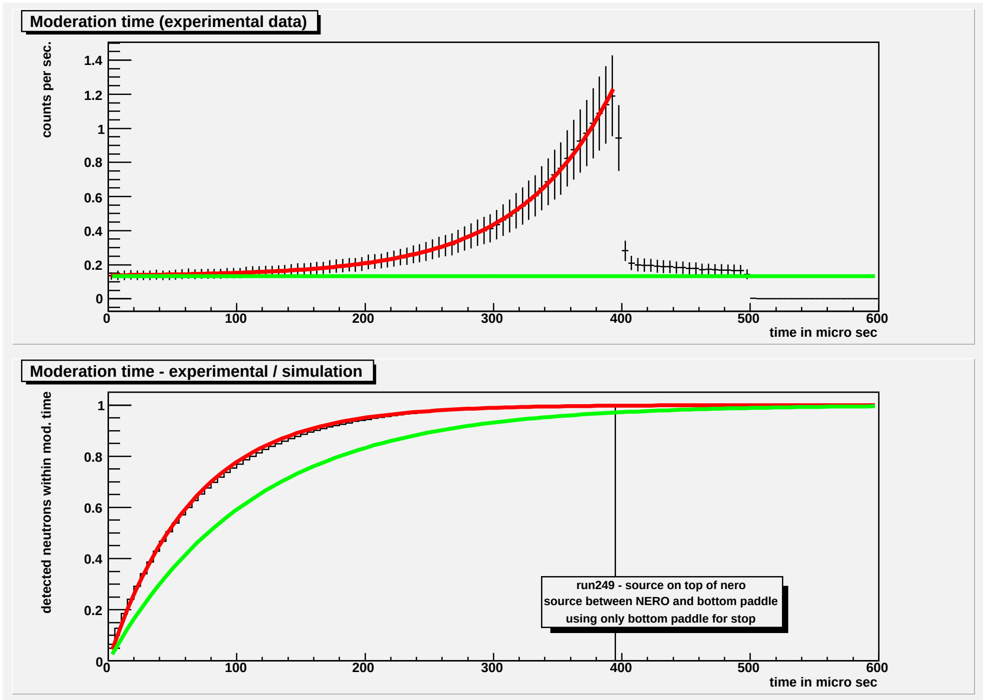

Figure 2.49: Run249 (source on top of NERO): Comparison experiment / MCNP simulation. Top: experimental data with exponential fit and offset. Bottom: relative amount of moderated neutrons vs. time in experiment (red/black) and MCNP simulation (green)

Fit function for the experimental data:

$$f(x) = [0] + [1] \cdot e^{\frac{t}{[2]}}$$

with the parameter for the experimental fit:

NAME	VALUE	ERROR	UNIT
[0]	0.133	$7.486 \cdot 10^{-3}$	1
[1]	$4.74 \cdot 10^{-3}$	$1.68 \cdot 10^{-3}$	1
[2]	72.20	5.43	μs

According to a decay function, we can calculate the half-life of the moderation time, which means, that after $t_{1/2}$ half of the neutrons are moderated and detected.

$$\lambda = \frac{1}{[2]}$$

$$t_{1/2} = \frac{ln2}{\lambda} = ln2 \cdot [2]$$

The half-life for the moderation was found to be $t_{1/2\,mod-time} = 50.05 \pm 3.77\ \mu s$. Figure 2.49 (bottom) shows the normalized integral data from experimental data (black), experimental fit (red) and MCNP simulation (green) by Giuseppe Lorusso [Lor08]. The MCNP simulation data predict the moderation half-life time to be $t_{1/2\,mod-time} = 77,59 \pm 5,75\,\mu s$. The simulation also takes into account, that the source is centered on top of NERO.

	exp. fit		MCNP fit	
time [µs]	*mod.*	$\Delta mod.$	*mod.*	$\Delta mod.$
50	49.97%	3.76%	36.02%	4.43%
100	74.97%	1.88%	59.07%	2.83
120	81.03%	1.43%	65.77%	2.37%
140	85.62%	1.08%	71.37%	1.98%
150	87.48%	0.94%	73.82%	1.81%
160	89.10%	0.82%	76.05%	1.66%
180	91.73%	0.62%	79.97%	1.39%
200	93.73%	0.47%	83.25%	1.16%
220	95.25%	0.36%	85.99%	0.97%
250	96.87%	0.36%	85.99%	0.97%
300	98.43%	0.12%	93.14%	0.47%
350	99.22%	0.06%	95.61%	0.30%
400	99.61%	0.03%	97.19%	0.19%

Table 2.13: Relative amount of moderated neutrons, estimated by experiment and MCNP simulation after special times.

NERO's experimental setup allows 200 µs for moderation of the neutrons (TDC gate width). The experimental data show, that 93.73% of the neutrons are moderated after that time, unlike the MCNP simulation, where only 83.25% are moderated. The difference can be explained with the setup for the time measurement and the ^{252}Cf source, which emits multiple neutrons with each fission event. The simultaneously emitted neutrons need different times to be moderated, but the measurement will use the neutron with the shortest moderation time to start the TDC. Because of that, the measured moderation time is underestimated in this setup. The MCNP simulation runs with the emission of only one neutron. There are two ways to correct this discrepancy.

1. Modify the MCNP simulation and create conditions of multiple neutron emission with the multiplicity distribution of the ^{252}Cf source. Use the shortest moderation time to simulate the measured moderation time.

2. Gate the experimental data on the neutron multiplicity. This is a possibility to see the dependence of the measured moderation time to the neutron multiplicity in the event. This has been tested, but since

only three quads were connected to the TDC (one quad is removed to connect the γ stop), the multiplicity was not detected correctly. Because of this, no data are presented, but the trend of decreasing measured moderation times with increasing number of multiplicity seems to be true.

Even though the systematical underestimation of the measured moderation half-life speaks for the prediction of the MCNP simulation, it should be mentioned that for such simulations, huge volumes of moderation material might be an issue in general [Lor08].

Because the moderation time depends on the relative position of the source to the moderator; and in a real experiment, the neutrons are emitted in the center of NERO, a second measurement is done with the same electronic setup, but the following assembly. Because the solid angle of the γ- detection is worse, higher background in the γ stop signals is expected.

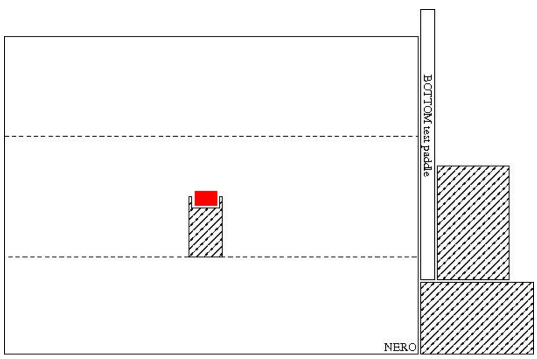

Figure 2.50: Run250. Arrangement for moderation time measurement. ^{252}Cf- source inside of NERO. The scintillator covers the hole of the beam line cut out on one side of the detector.

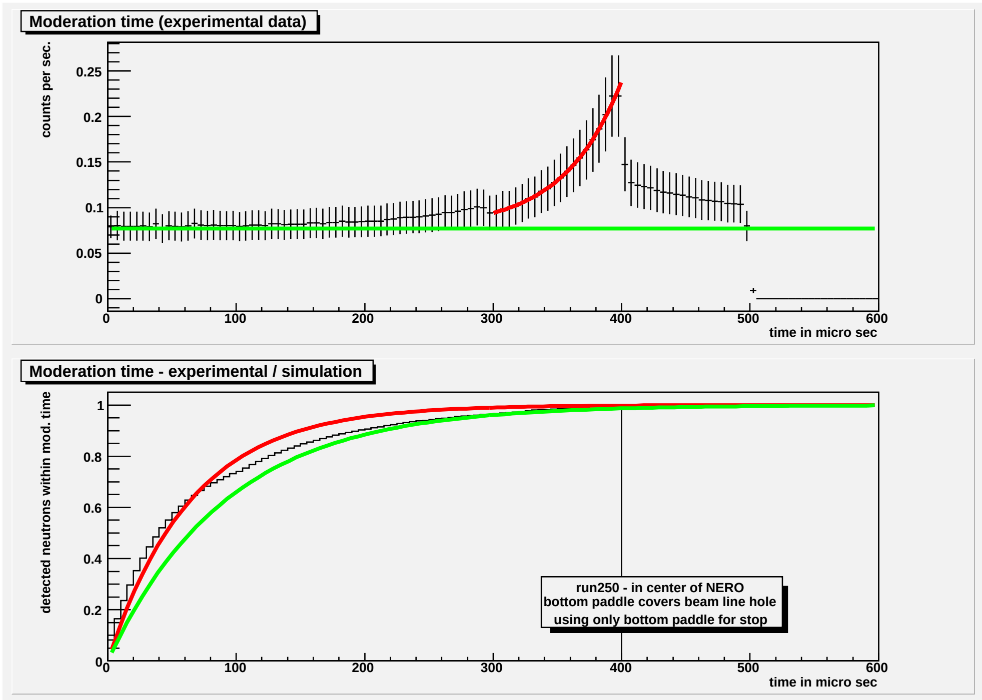

Figure 2.51: Run250 (source inside NERO): Comparison experiment/MCNP simulation: Top: experimental data with exponential fit and offset. Bottom: relative amount of moderated neutrons vs. time in experiment (red/black) and MCNP simulation (green).

	exp. fit		MCNP fit	
time [µs]	*mod.*	Δ*mod.*	*mod.*	Δ*mod.*
50	65.79%	20.38%	41.69%	2.69%
100	88.30%	6.97%	66.00%	1.57%
120	92.38%	4.54%	72.60%	1.26%
140	95.04%	2.98%	77.92%	1.02%
150	96.00%	2.38%	80.18%	0.91%
160	96.77%	1.92%	82.20%	0.82%
180	97.90%	1.25%	85.66%	0.66%
200	98.63%	0.82%	88.44%	0.53%
220	99.11%	0.53%	90.68%	0.43%
250	99.53%	0.28%	93.26%	0.31%
300	99.84%	0.10%	96.07%	0.18%
350	99.95%	0.03%	97.71%	0.11%
400	99.98%	0.01%	98.66%	0.06%

Table 2.14: Ratio of moderated neutrons after special times: run250

Figure 2.51 (top) shows the experimental data. The relative background is higher, because the solid angle of the γ detection is worse. Another issue is a bump after approx. 100µs in the time spectrum. It is probably an artificial effect and has nothing to do with the physics of the moderation of the neutrons. This is why the experimental fit only considers the data of the first 100µs. The moderation half-life time is 32.3 ± 19.2 µs (experimental fit) and 64.25±2.97µs (simulation fit). The huge error for the experimental fit can be explained with the error bars of the bins. As expected, the moderation half-life, which is calculated from experimental data and from MCNP simulation get shorter because NERO is designed for neutron emission in its center. The discrepancy between experiment and MCNP simulation is ascribed to the multiplicity in neutron emission of ^{252}Cf.

It has also been tried to use γs as start and neutrons as stop signals to eliminate the multiplicity issue, but the γ background was too high.

In another setup, the source was located on top of NERO between two scintillators for γ detection, where both scintillator signals in coincidence were used for the TDC stop signal.

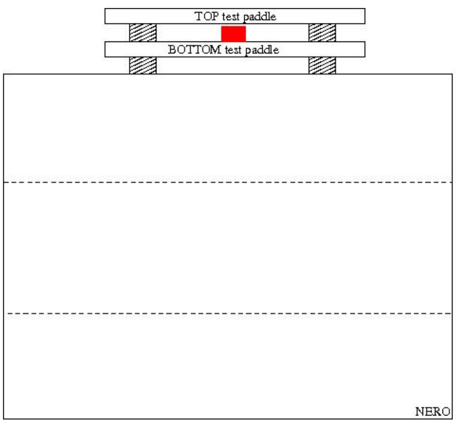

Figure 2.52: Run252. Arrangement for moderation time measurement. The ^{252}Cf source sits on top of NERO between two scintillators. Coincidence in the scintillators provide the TDC stop signal.

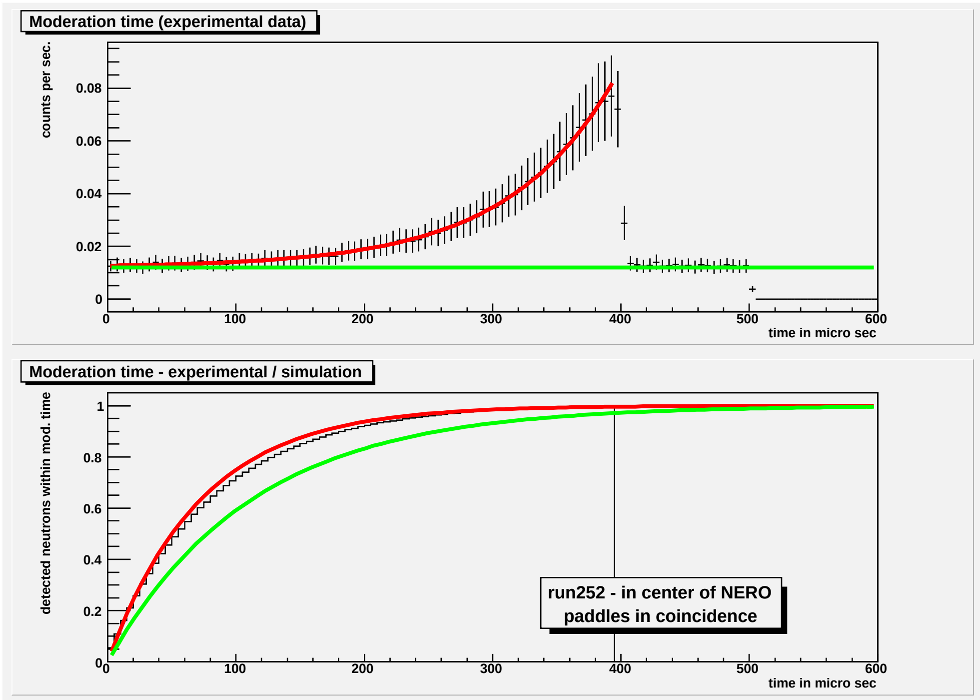

Figure 2.53: Run255 (source on top of NERO between two paddles): Two paddles in coincidence provide the TDC stop signal. Comparison experiment / MCNP simulation: Top: experimental data with exponential fit and offset. Bottom: relative amount of moderated neutrons vs. time in experiment (red/black) and MCNP simulation (green).

The experimental fit gives a moderation half-life time of $57.52 \pm 5.37\,\mu s$, which is slightly more than in setup 2.48, but still within the errors of both measurements. The discrepancy to the moderation time predicted by the MCNP simulation ($t_{1/2\,mod-time} = 77,59 \pm 5,75\,\mu s$) is explained with the ^{252}Cf neutron multiplicity.

The experimentally measured moderation times show, that the TDC gate width of $200\,\mu s$ is a reasonable time and a good agreement between relative amount of moderated neutrons and dead time of the neutron detector.

Chapter 3

Active Cosmic Ray Shield for NERO

3.1 Cosmic Rays: origin, energies

In order to suppress events in a detector system, which are caused by cosmic radiation, the types and the energies of the particles, which penetrate the experiment must be known.

3.1.1 Primary cosmic rays

Particles, which are produced and accelerated in sources within the Milky Way have to pass an average area density of $6\frac{g}{cm^2}$ before they reach the earth's atmosphere. Most of the charged particles of the primary cosmic radiation are protons (approx. 85%) and α- particles (approx. 12%). Heavier elements with $Z > 3$ contribute only to 3%. Only few electrons are in the cosmic radiation. The abundances of the primary cosmic radiation are shown in figure 3.1. In this figure, a high abundance of hydrogen and of helium and also of iron can be observed. Elements with lower mass than iron are produced by spallation of heavier elements. That becomes clear, when you compare the abundance of Li, Be and B in primary cosmic radiation with the abundance in the solar system. The odd/odd even/even effect can also be observed. A wide range of energy is covered by the particles, where high energy particles are more unlikely.

The knee at about $10^{15}eV$ in figure 3.2 can be explained by the escape speed in the Milky Way. The magnetic field of the Milky Way ($B = 10^{-10}T$) is much weaker than the magnetic field of the earth. Particles with energies $E > 10^{15}eV$ reach a radius larger than the dimension of the Milky Way and can leave the Galaxy. Another reason might be the maximum acceleration of particles in supernovae, which is also reached around $E \approx 10^{15}eV$ [Gru00]. Energies of particles, which exceed $10^{19}eV$ (beyond the ankle) are probably a contribution of extragalactic sources. It is expected, that there are no

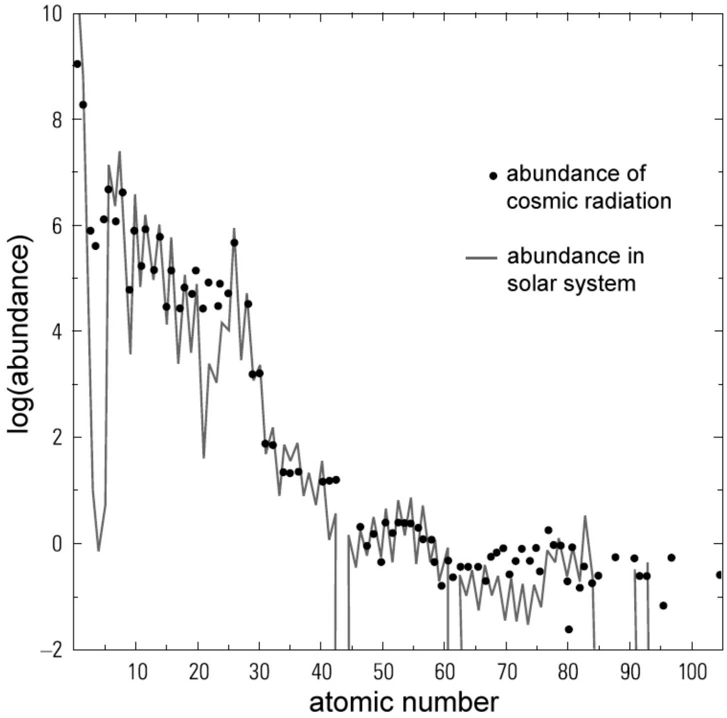

Figure 3.1: Abundances of the primary charged cosmic radiation in comparison to the solar abundances [Gru00].

particles with energies $E > 6 \cdot 10^{20} eV$, because primary protons create pions in reactions with the black body γs.

3.1.2 Secondary cosmic rays

Different influences affect the primary cosmic radiation and define, if a particle reaches the earth or not. Magnetic fields of the sun (created by the solar wind: low energy particles p/e^{-}) and of the earth modify the intensity of the particle flux. If a particle's trajectory will hit the earth, the particle has to pass the atmosphere with an area density of about $1000 \frac{g}{cm^2}$ (orthogonal to the earth's surface). Obviously, the area density increases for trajectories with zenith angles $\neq 0°$ because the distance in the atmosphere increases, too. There is a $cos^{\mathbf{2}}$ relation between zenith angle and particle rate [Sch03]. Reactions of the particles with nuclei in the atmosphere produce electromagnetic and hadron cascades. The average area density, which causes a reaction is different for e/m and hadron particles. For γs and electrons, $26.66 \frac{g}{cm^2}$ are necessary, which corresponds to 27 interactions within the thickness of the atmosphere. The average area density for a hadron interaction is about $90 \frac{g}{cm^2}$, which corresponds to 11 interactions within the atmosphere. The two different kinds of showers do not only differ in their average number of interactions, but also in their reactions and lateral

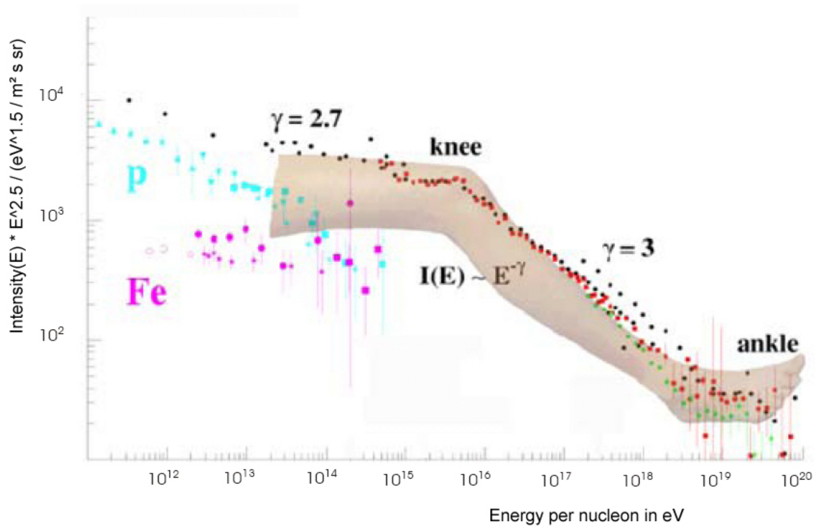

Figure 3.2: Energy spectrum of charged primary cosmic particles [Sch03].

propagation (see figure 3.3).

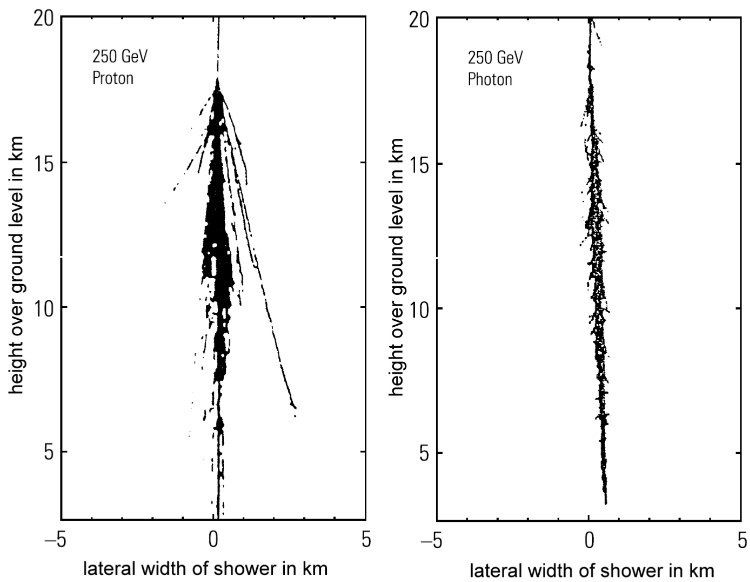

Figure 3.3: Lateral propagation for hadron and e/m showers with 250GeV [Gru00].

Since a wide range of energy is available, a lot of reactions are conceivable in the atmosphere.

$$
\begin{array}{ccc}
p+n \rightarrow p+n+\pi^0 & p+n \rightarrow p+p+\pi^- & p+n \rightarrow n+n+\pi^+ \\
p+p \rightarrow p+p+\pi^0+\pi^0 & p+p \rightarrow p+n+\pi^+ & p+p \rightarrow n+n+\pi^+ +\pi^+
\end{array}
$$

The products (neutrons and protons) react again. The pions decay to muons and γs:

$$\pi^+ \rightarrow \mu^+ + \nu_\mu \quad \pi^- \rightarrow \mu^- + \overline{\nu_\mu} \quad \pi^0 \rightarrow \gamma + \gamma$$

and the muons decay to electrons and neutrinos.

$$\mu^+ \rightarrow e^+ + \overline{\nu_\mu} + \nu_e \quad \mu^- \rightarrow e^- + \nu_\mu + \overline{\nu_e}$$

Radiation at ground level

Basically, particles with low energies do not reach the ground level. Figure 3.4 shows the flux intensity of different particles, depending of the height and area density.

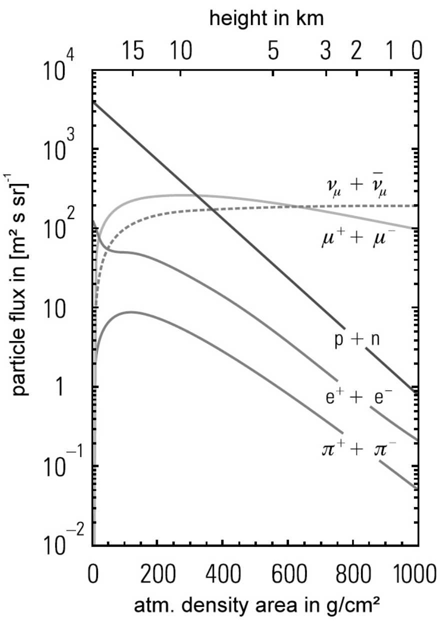

Figure 3.4: Particle flux intensities for different particles with energies > $1\,GeV$ [Gru00].

Three components of a shower can be distinguished.

1. *Hadron component.* Lateral propagation (see sub chapter 3.3) creates the core of the shower and is composed of protons, α-particles and neutrons. The contribution at ground level depends on the energy of the primary particle and is about 1%.

2. *Electromagnetic component.* It is composed of photons and electrons. The lateral propagation (see figure 3.3) is also relatively small and particles concentrate to the core of the shower. The contribution of this component at ground level is about 20%.

3. *Muon component.* Muons are created by decay of charged pions. Approximately 80% of the cosmic particles at ground level are muons. This component has the highest lateral propagation.

In addition to the three components, there is also a neutrino component, but since the cross section of neutrinos is very low, no neutrino induced background can be detected with a neutron detector like NERO or the used scintillators for the active cosmic ray shield. The neutron background in NERO is caused by neutrons, which are induced in matter on ground level or close to it. Only very view neutrons from the hadron component (which contributes only 1%, anyway) produce signals in NERO.

3.2 Idea: Active Cosmic Ray Shield

Neutrons created by cosmic ray reactions, which are moderated and detected in NERO cannot be distinguished from events created by experimental reactions. Because of this, the idea of adding an active cosmic ray shield to NERO is considered. The basic idea is quite simple. If a passive shielding is not possible, the actual detector is blocked in the moment, when an external particle passes the detector. As described in sub chapter 1.5, passive shielding for neutrons is complicated and any combination of moderator and n-capture material is limited by a neutron energy. The veto signal is provided by coincidences of two scintillators, which detect charged particles and γs above and below NERO. This way the information, if a shower (possibly including and inducing neutrons) passes NERO is provided. An important question is the correlation of neutrons caused by cosmics to the rest of a shower. Runtimes and lateral propagation might be different.

The schematic setup for the active cosmic ray shield and NERO is shown in figure 3.5.

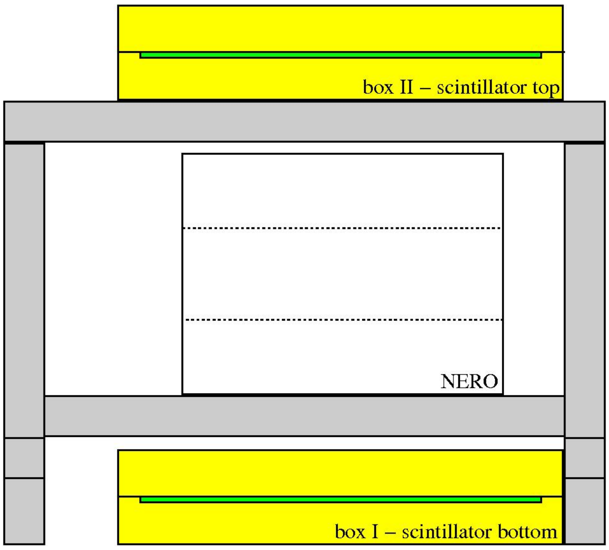

Figure 3.5: Schematic assembly of the active cosmic ray shield for NERO. The scintillators (green) are assembled in light tight wooden boxes (yellow), which are positioned above and below NERO. A frame (gray) is the support structure for the NERO detector and the box above NERO. The box below NERO sits on the floor.

In this setup, the scintillators have been attached in two wooden boxes, which provide support and a light tight closure. (see sub chapter 3.4 for details). Box I sits on the floor below NERO and box II sits about 1.10 m above the floor with NERO placed in between both boxes. The distance between the two scintillators should be as small as possible in order to maximize the solid angle of the coincidence system. Each scintillator covers an area of $1 \cdot 1m^2$ centered over the area of NERO. The idea of the active cosmic ray shield is pointed out in the diagram in figure 3.6.

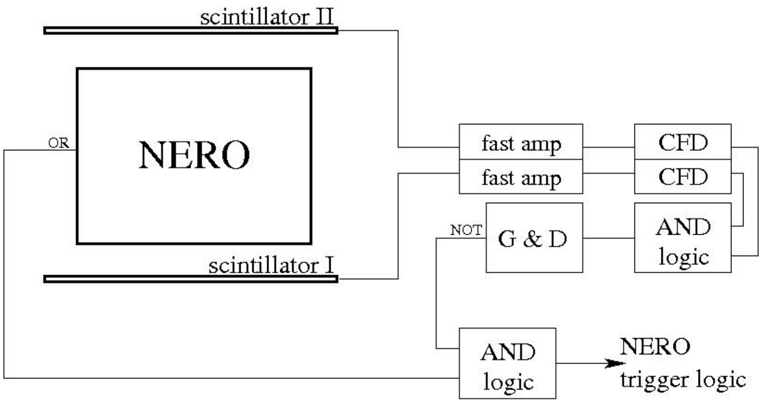

Figure 3.6: Basic electronic diagram of the active cosmic ray shield.

If there is a coincidence between scintillator II and I, the NERO Master Gate Live is blocked. The period of the blocking time is set with a gate and delay generator. The diagram shows the hardware veto setup to make the idea clear. The same effect can be reached, when the scintillators coincidences are read out by the computer and the anti-coincidence of NERO with the scintillators is ensured by software.

3.3 Electronics of the Active Cosmic Ray Shield (CRS)

The electronics have been installed before the actual scintillators from Mainz arrived (see sub chapter 3.4). Smaller test paddles (approx. $30 \cdot 45 cm^2$) were used to investigate the correct implementation of hardware and readout by the computer. The following components were added to the electronic rack of NERO:

- *HV supply:* Power Designs Inc. Westbury, N.Y. Palo Alto Calif. Model 1570, 1-3012V, 40mA, 2ch High Voltage calibrated DC Power source
- *fast amplifier:* quad fast amplifier manufactured by NSCL, one input / three outputs (amplification factor of 2.69±0.07 for a rectangle signal. No documentation available)
- *CFD:* quad CFD Tennelec TC 455
- *QDC:* 32ch QDC C.A.E.N. 792 [Cae08-2]

In addition to the above mentioned modules, some logic units and delay boxes were used to adjust timing and set logics.

Implementation of C.A.E.N. QDC module 792

In order to understand the features of the scintillators, to set CFD thresholds and to take energy spectra from the cosmic radiation, a QDC has been included to the electronics. The C.A.E.N Mod.V792 module is a 32ch QDC. This model has no connector for automatic geographical address allocation in the VME crate. Therefore, this is done by four rotary switches on the module plane. The same address has to be used in the readout code "Unpacker.cpp" to initialize the module. The base address is the start address of a module specific range. Modules with the connector for the automatic geographical address allocation will receive a slot-depending address range. In order to avoid conflicts with other modules, the address has to be chosen with care. The module is initialized in the readout code.

```
m_pVMEADC10 = new CAENcard(VMEADC10_N, CRATENUM1);
m_pVMEQDC12 = new CAENcard(VMEQDC12_N, CRATENUM1, false, VMEQDC12);
```

The two lines show the different initialization of modules with and without automatic geographical address allocation. The first line initializes an ADC module with this feature. Slot number and crate number are defined in the variables VMEADC10_N (= 10) and CRATENUM1 (=0). The second line initializes the QDC for the scintillators. The slot number is defined, but is not used, because of the third boolean value "false" (=no automatic geographical address feature). The base address is submitted in the variable VMEQDC12 (=0x0c000000) and has to be out of the address range of any another modules in the VME bus.

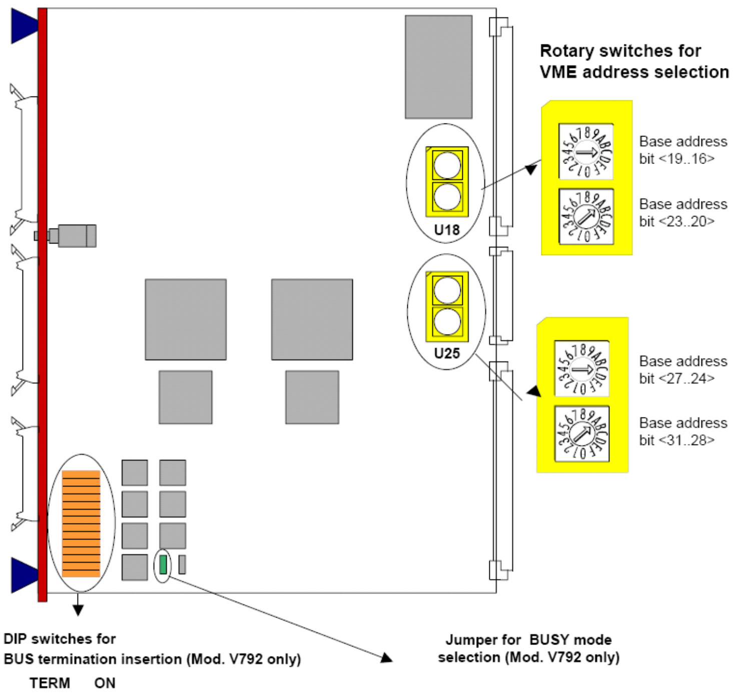

Figure 3.7: Schematic side view of the QDC. The first four digits of the base address are set with the four rotary switches.

Figure 3.7 shows the schematic side view of the QDC module. In addition to the rotary switches for the base address, settings can be chosen with DIP switches and jumpers. See C.A.E.N. documentation for details [Cae08-2].

Threshold and Pedestal:

Thresholds of each QDC channel can be set in the "NEROSegment.cpp" code in the initialization part of the QDC with the command

m_pVMEQDC12->setThreshold(QDC-channel,value);

where *value* is a number between 0 and 255. The command

m_pVMEQDC12->setPedestalCurrent(value);

sets the pedestal current for the whole unit, where *value* is a number between 0 and 255 (see [Cae08-2]). The pedestal current multiplied with the time width of the QDC gate is the charge, which is measured when no signal is pending. The result is the so called pedestal peak in the spectra, when the QDC is triggered, but no actual signal is pending. Because only ch0 and ch1 are used, all other channels have no input and the spectra of those unused channels only show the pedestal peak. For shorter QDC gates, the pedestal current can be lowered to shift the pedestal peak out of the range of interesting energy data. The pedestal is set to a value of 60 and the thresholds are set as low as possible (=0), because all the data have to be displayed in such a way that the CFD thresholds can be set and a hardware veto be tested. The QDC gate must precede the signal by more than 15ns. The scope screen in figure 3.8 shows the gate width and the signal of ch1 (scintillator II / top box). QDC gate width and pedestal current should not be modified after the energy calibration, or the calibration has to be repeated.

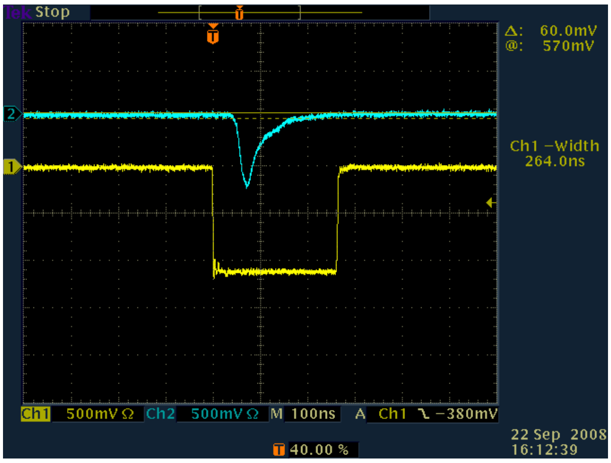

Figure 3.8: Signal and QDC gate for ch1 (scintillator II / top box). The signal is amplified, before it es routed to the QDC.

With the lowest CFD threshold and QDC threshold=0 an underflow is generated, which means that events with a very low energy are put independent of their real charge in one bin (pedestal channel) (in QDC ch00, this is bin64; in QDC ch01, this is bin59).

Estimate of minimal charge deposit of signals for the measurement by the QDC and linearity of the QDC

In order to estimate the minimum charge deposit which can be measured by the QDC, the setup in figure 3.9 is used.

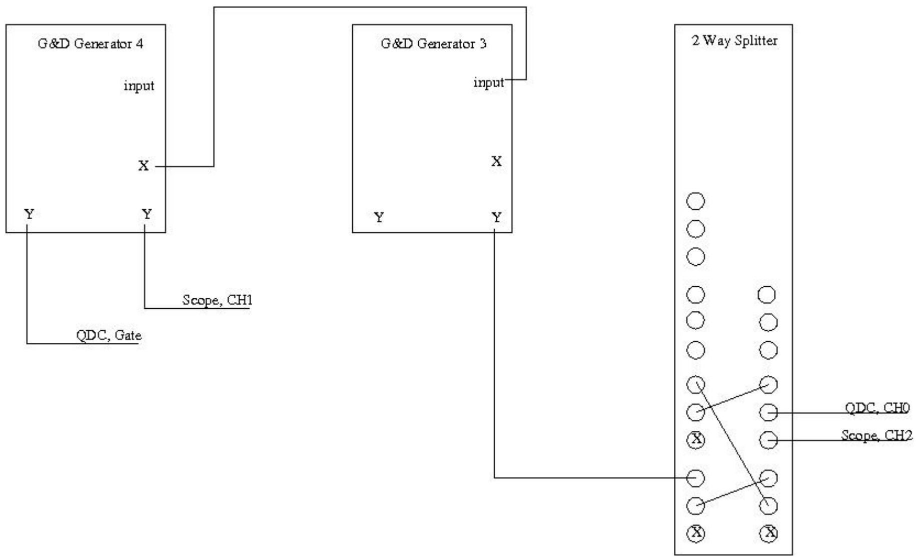

Figure 3.9: Splitter to attenuate signals for minimal charge deposit measurement

The input to Gate&Delay Generator 4 is connected to the NIM signal of one CFD (see figure 3.9). Any NIM signal would be fine, also from a pulse generator. In the Y output, the QDC gate is generated. Delay and width are adjusted with the G&D generator 4. One of the Y outputs is connected to the QDC (gate), the other one to the scope. The X output is not adjustable in width and delay, but is connected to G&D generator 3 and will be the artificially produced charge signal to be measured, which can be manipulated by adjusting width and amplitude. The measured charge is given by the signal width multiplied with the amplitude and divided by 50Ω [Cae08-2].

$$Q = \frac{U_{signal} \cdot t_{width}}{R}$$

The amplitude of the signal is adjusted, by using a 2-way splitter and by connecting terminators. Different numbers of splits create different attenuations. The last splitter output is connected to the QDC signal input and the scope. It is important not to unplug the scope, because this has the same influence to the signal as removing a terminator.

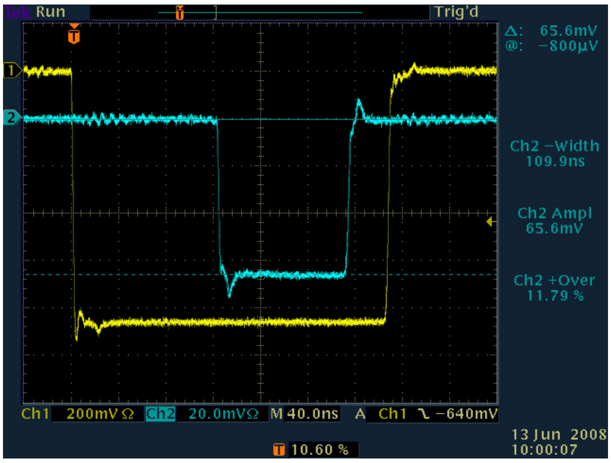

Figure 3.10: Measurement of QDC linearity and minimum charge which can be measured by the QDC: QDC gate (yellow) and artificial created charge (blue). Both signals are created with G&D generators and the charge in the blue signal can be varied.

In all adjustments, the width of the signal is measured by an automatic scope feature. The amplitude is measured by delta cursors (upper right in figure 3.10) and does not change when varying the width of the signal. The change of the amplitude becomes necessary, since the width of the signal is limited by the gate, but a wide range of charge has to be covered.

Once, a charge is set, the mono-charge signals will create a small peak in the QDC spectrum. Twenty signals with different known charges were created and each peak position was located and plotted in figure 3.11. QDC Ch00 and Ch01 are analyzed with this method. The plotted data show the linearity and the minimal charge deposit for both channels can be estimated.

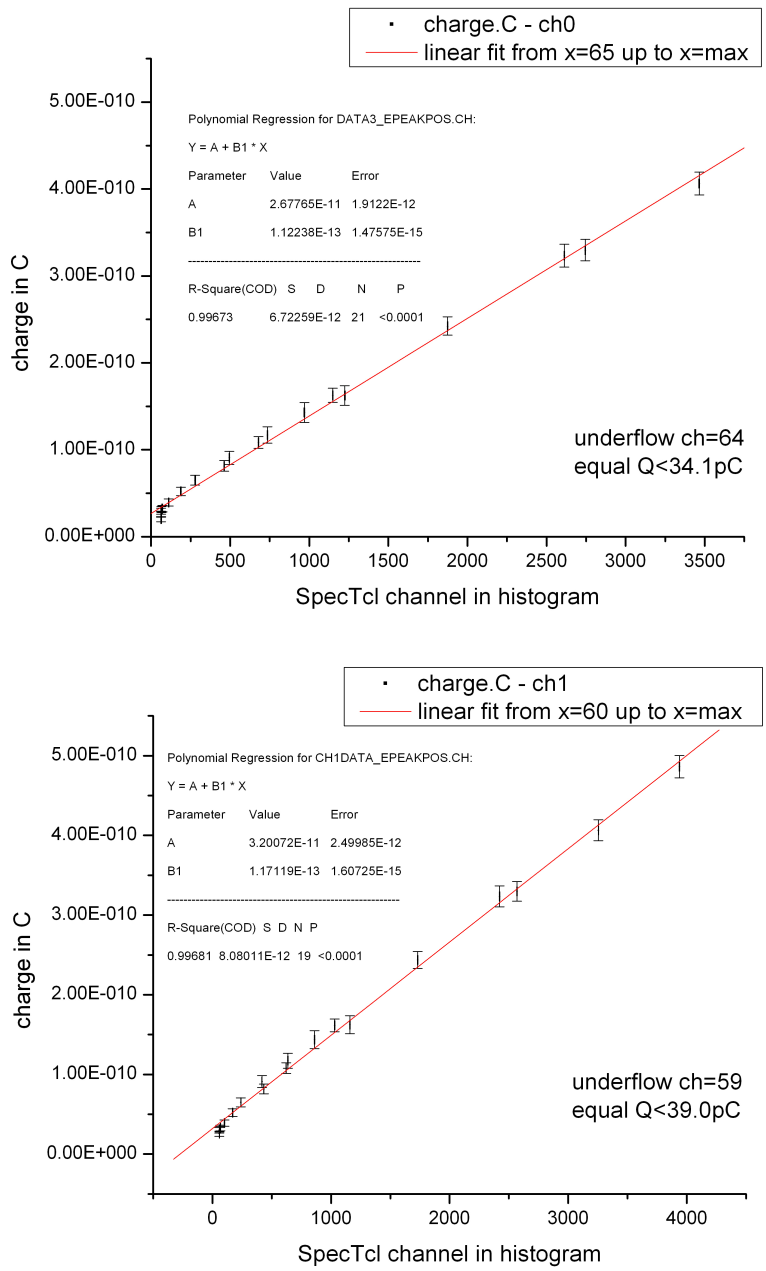

Figure 3.11: Underflow bins and linearity of QDC ch0 (top) and ch1 (bottom).

The linearity is given in both channels (see figure 3.11) . The underflow bin in QDC channel00 is bin 64 and in QDC channel01 bin59. This means, that channel00 is sensitive to signals with a charge greater than $34.1 \pm 1.9 pC$ and channel01 is sensitive to signals with a charge greater than $39.0 \pm 2.5 pC$. In addition to that, it is recognized, that the different QDC channels are shifted and have a different charge offset (fit parameter A in figure 3.11).

3.4 Scintillators & light guides from Mainz

3.4.1 Functionality of a scintillator

Scintillators produce light, when a charged particle or γs pass the material. There are also neutron scintillators available, but there are preceding reactions, which produce charged particles, so the functionality is basically the same. The number of photons which is produced in a scintillator, depends on the amount of deposit energy. Two types of scintillators with different functionality are available: organic and inorganic scintillators.

Inorganic scintillators are crystals, which are doped with color centers. A charged particle kicks out electrons and leaves ionized atoms in the material. The charge drifts to a color center, where it de-excites by emitting photons. Because the charge has to drift to the color center, the time resolution is worse than in organic scintillators.

Organic scintillators contain three components: The solvent (e.g. polystyrene, acryl glass or plexiglass), which contains the fluorescence material and the wavelength shifter. The fluorescence material (e.g. naphthalene) emits UV light. Because the UV photons can also be absorbed by the fluorescence material, a wavelength shifter is used to transform the UV to visible light, which is not absorbed by the fluorescence material. Organic scintillators are faster than inorganic scintillators. The de-excitation after the charge deposit occurs within nano seconds.

In the setup for the active cosmic ray shield of NERO, organic plastic scintillators are used.

3.4.2 Scintillators from Mainz

Figure 3.12: One of the light guides and scintillators from Mainz. Each scintillator (in the back) is coupled to one light guide (in the front), which guides the light to a photomultiplier.

The scintillators of the active cosmic ray shield must cover a huge area in order to detect a maximum amount of showers passing the detector system.

Scintillators from Institut für Kernchemie, Universität Mainz [Kch08] with an area of $1m^2$ $(100 \cdot 100 \cdot 1.5cm^3)$ are assembled in two wooden boxes. Both scintillators have been part of a detector system (Nuclear Enterprises NE 110) and have been used before to suppress background in experiments [Peu85]. Because of the large width of the scintillators of $1m$, light guides are used to conduct the light to the photomultiplier. Each scintillator is connected to a 5" photomultiplier tube via an adiabatic light guide.

3.4.3 Adiabatic light guide

The profile of each scintillator is 100cm by 1.5cm. Since the photomultiplier tube is sensitive in a 5" circle, the light guide has to change the shape. The idea of an adiabatic light guide is the use of total reflection on the surfaces of the material. According to the index of reflectance of the light guide material and the surrounding medium (air), a maximum angle of total reflectance is given by

$$\alpha = sin^{-1}(\frac{n_2}{n_1})$$

where n_2 is the refractive index of the less dense medium (air) and n_1 of the denser medium (light guide). Obviously, the greater the ratio of n_2 to n_1, the larger the maximum angle of reflectance. According to the maximum angle, the radii of bendings in the light guide are limited, resulting in a minimum of dimensions of the light guide. A second physical requirement for a minimum light loss is the theorem of Liouville. The theorem has to be considered in both dimensions of the profile. The light guide separates the width of 1m in 9 guides, which are smoothly twisted and merged together to a shape, which fits the photomultiplier circle.

3.4.4 Photomultiplier tube (PMT)

The photomultiplier converts the photons to an electrical signal. A photon hits the photo cathode, where several electrons per photon are emitted. An electrical field accelerates the electrons to the first dynode, where multiple electrons are emitted for each incoming electron. An amplification occurs. Multiple serial dynodes provide electrical fields and the process of accelerating and hitting a dynode is repeated. This results in an amplification of the number of electrons. The last dynode has the function of an anode and collects all charge, which can be measured over a resistor. The deposit charge at the anode is proportional to the primary incoming photons. The photons are proportional to the deposit energy of the detected particle in the scintillator. The described process shows the basic idea of a photomultiplier. Dynodes can also be substituted by mashes, which create the same effect of amplification. A scintillator system can be optimized to energy resolution or time resolution (organic / inorganic scintillators). Since the active cosmic ray shield serves only for providing a veto signal, the energy resolution is not important. Two different PMTs are provided by the detector lab. Both units have been in use before.

PMT1 (box1, bottom):	EMI 9791 KB – 9545
PMT2 (box2, top):	Hamamatsu R 1512

3.4.5 Optical coupling of scintillator and light guide:

Scintillator, light guide and photomultiplier are coupled optically. Just because of the dimensions, this is a challenge in the case of an area of $100 \cdot 1.5cm^2$. In cooperation with specialists in the NSCL detector lab, a two-component transparent silicon (RTV-615) is used for the coupling of the scintillator to the light guide. The support structure in the light tight wooden box (see sub chapter 3.4.7) assures the correct alignment in all dimensions. Felt between support structure and bearing areas of scintillator or light guide makes sure, that no damages like scratches happen to the system. The characteristics of the silicon RTV-615 has been tested with smaller scintillators to identify possible issues. Tiny spacers were used to define a gap between the test scintillators, and tape was used to cover one long and both short side slots. RTV was mixed with 10 parts RTV-615 to one part hardener in a beaker and then put into a vacuum chamber to extract bubbles. The bubbles were “cooked out”, but they also shrink because air can diffuse through the silicon. After all bubbles were disappeared, the silicon was filled into a syringe. The syringe is very convenient to inject the silicon into the gap between scintillator and light guide.

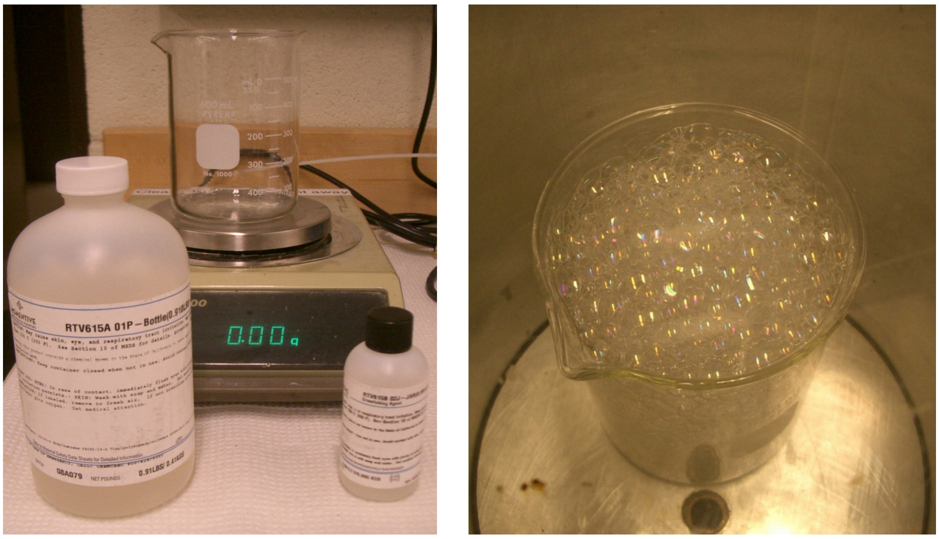

Figure 3.13: RTV-615 preparation: Admeasure RTV-615 (left); remove bubbles in vacuum chamber (right).

Temperature	Cure Time*
25 °C	6-7 days
65 °C	4 h
100 °C	1 h
125 °C	45 min
150 °C	15 min
* Cure times are only approximate.	

Table 3.1: Cure times for RTV-615 silicone rubber compound [Bay08].

Different experiments were performed to figure out, how to handle the RTV silicon.

The final procedure is highlighted in the following.

1. All surfaces are cleaned with ethanol in order to prepare a fat free environment.
2. Two tiny spacer (2mm) are attached with super glue at the left and the right outer corners of the scintillator profile.
3. The long bottom slot and slots to both sides are closed with tape (blue transparent tape – comparable to capton tape)
4. The RTV-615 is mixed with hardener (ratio 1:10) (40mg total per scintillator)
5. The beaker with mixture is put into a vacuum chamber to "cook" bubbles out.
6. The clear mixture is filled into syringes and the silicon is injected into the prepared gap between the light guide and the scintillator.
7. The silicone rubber compound cures within 24 hours sufficiently (at room temperature). After this time, the work can be continued, but exhaustive curing finishes after 6-7 days.
8. The tape can be removed after one week of curing.

3.4.6 Optical coupling of light guide and PMT with grease

The optical coupling of a 5" photomultiplier is a standard procedure. Support and adjustment of PMT and light guide is provided by the support structures in the light tight wooden box. No stress must be born by the coupling connection.

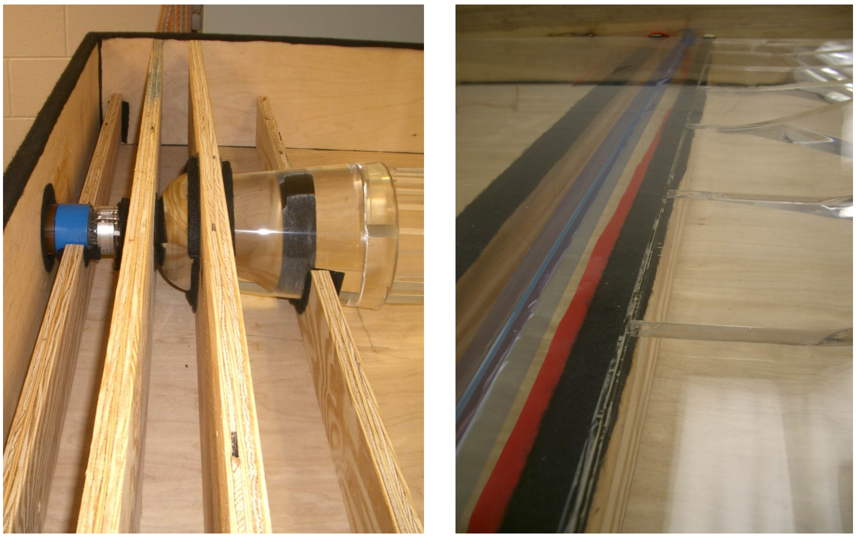

Figure 3.14: Optical coupling between PMT and light guide (left) and light guide and scintillator (right).

1. It has to be assured, that PMT and light guide match perfectly. Stress in the coupling connection will cause de-coupling.

2. All surfaces are cleaned with ethanol

3. Reasonable amount of grease (one spatula) is put in the middle of the PMT surface. PMT and light guide are moved together and the PMT is shifted in concentric circles until the grease fills the whole area between PMT and light guide.

3.4.7 Light-tight wooden boxes

The scintillators and light guides were delivered without a light-tight cover. Because of the mandatory light-tightness and the necessary support structure to hold the scintillator, the bulky light guide and the photomultiplier in position, a wooden box is necessary to guarantee all requirements. In addition to that, the box should be able to be opened and should be robust to hold itself and the inner equipment. A first design of a box with indenting corners to avoid direct light lines in between the contact areas of two boards was discarded, because the boards were too large for the machines of the NSCL machine shop. Because of that, a more simple model was built, but all contact areas, where possible light lines are created, have been sealed with black silicon. The black silicon has been put at the edges like glue, before screwing the boards together. The possibility to open the box is realized with an overlapping top. Basically, the box is similar to a shoe box. The upper edge of the box is covered with felt, so a light tight connection to the lid is assured. Three boards with notches hold the scin-

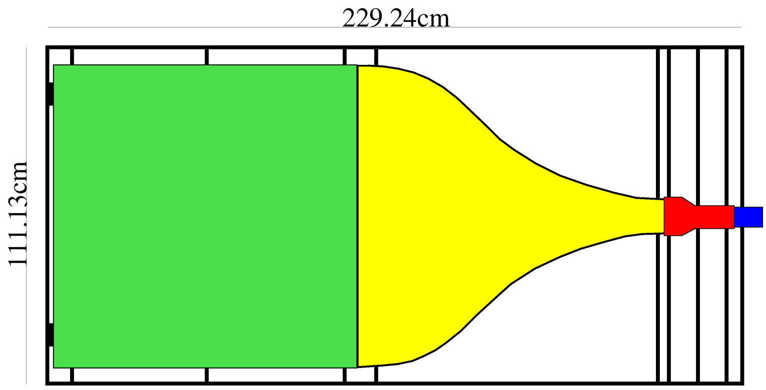

Figure 3.15: Schematic position of support structures (vertical black lines). Scintillator (green), light guide (yellow), PMT (red) and voltage divider (blue).

tillator in position. The light guide is hold by two boards and the PMT is hold by additional three support boards to avoid any stress in the connection to the light guide. Figure 3.15 shows schematically the positions of the support structures. The support boards have rectangle notches to hold the scintillator (green) and the light guide (yellow). The other support boards have semi-circle notches to hold light guide and PMT (red) in position. All boards are covered with felt to adjust height and position and to preserve the equipment. On the PMT side of the box, a hole is sawed into the outwall-board, which provides space for the voltage divider (blue). The gap between voltage divider and board is sealed with felt.

Figure 3.16: Wooden box in construction status.

3.5 Biasing scintillators / energy calibration

The construction of the wooden boxes was finished successively. First, box I is finished and put in the top position above NERO. It is much easier to work on a box in top position, since space in lab 108 is very limited. After optical coupling and satisfying tests about the light tightness of the wooden box, box I was moved to the position below NERO and box II was moved into lab 108 to the top position in order to continue with the work of optical coupling.

Figure 3.17: Active cosmic ray shield - pictures: (left top) Box I in top position for testing. (left bottom) Box I in bottom position. (right) Final assembly - box I in bottom position / box II in top position.

The right picture in figure 3.17 shows the final assembly. The top box II can be opened easily for maintenance. Box I on the floor has to be pulled into the hallway for about one meter, before the box can be opened. The aluminum stair in front of the bottom box I on the floor is to prevent the voltage divider and out-coming cables from accidental damage.

3.5.1 Plateau Characteristics

The gain of the photomultiplier depends on the applied voltage. Plateau characteristics of each photomultiplier has been determined to set the voltage to a value, where the count rate is less sensitive to dark current and varying applied voltage. The thresholds of the discriminators for both channels were set as low as possible (just above the QDC underflow bin) and must not be changed during measurements for the plateau characteristics.

According to the specifications of the photomultiplier, the voltage is increased by $50V$ steps up to $1800V$, starting at $1500V$. The measurements were done separately for both PMTs, so the electronic was triggered only to one tube. Additional information can be found in [Ham08]. For each voltage, a background run (runtime=$15min$) and a run with a ^{22}Na γ source (runtime=$15min$) was made. The energy spectra were subtracted and the integrals plotted in figure 3.18.

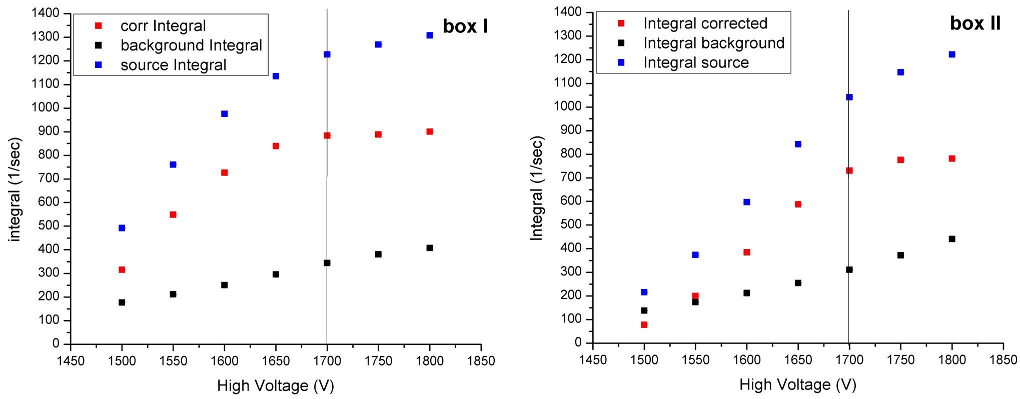

Figure 3.18: HV plateau characteristics for PMT I (left) and PMT II (right).

The rate of the background runs increase with voltage almost linearly, whereas the rate of the source runs increase with greater slope for voltages up to 1650V. With voltages higher than 1700V, the slopes of the background run and the source run converge, and the background corrected rates form a plateau. The requirement to use both photomultipliers with the same HV supply, lead to the choice of $U_{HV-supply} = 1700V$. Of course, the plateau for PMT II just starts around $1700V$, but the spectrum starts to get distorted in the low energy range for higher voltages (see appendix 5.1).

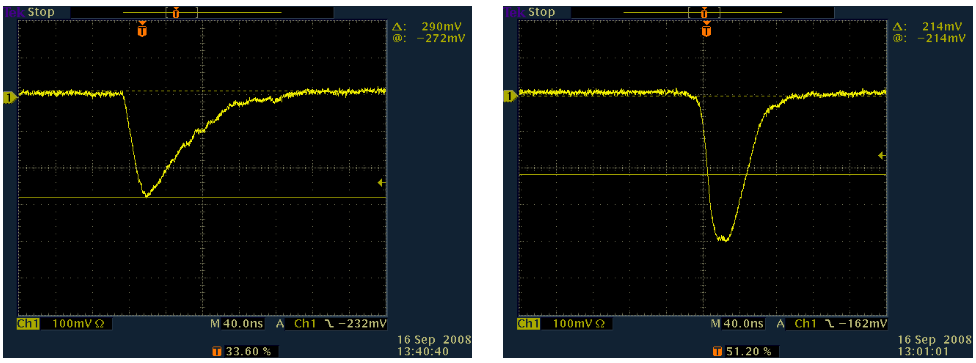

Figure 3.19: Signals from PMT I (left) and PMT II (right)

Figure 3.19 shows the signals of PMT I (box I, top position) and PMT II (box II, bottom position). Overall, the shape of the signals from PMT II look better and the amplitudes are stronger, than the signals from PMT I. The shape is important for the energy information, but since „only“ a veto signal is needed for the active cosmic ray shield, no additional time and resources were spent to optimize that issue.

3.5.2 Energy Calibration

In order to analyze the energy spectrum of cosmic rays, and also to know which energies are cut by thresholds, an energy calibration was done. ^{133}Ba, ^{54}Mn, ^{137}Cs and ^{60}Co γ-sources were used to calibrate the system. ^{133}Ba and ^{60}Co emit γs in multiple discrete energies. Because of that and the fact, that the energy resolution of the scintillators is too low to distinguish multiple Compton edges of different discrete energies, the weighted mean energy was used, as described in [Che89].

source	E_γ [MeV]
^{133}Ba	0.344*
^{137}Cs	0.662
^{54}Mn	0.835
^{60}Co	1.253*

*weighted mean energy

Table 3.2: Sources for γ energy calibration of scintillators and the according γ energies [Che89].

For the energy calibration, an over-night background run was performed. Each source was put in exactly the same position on the box, centered to the scintillator inside. The energy calibration was done separately for each box, because NERO was positioned in between the scintillators and would have absorbed and modified the radiation.

	box I (bottom)		box II (top)	
source	run#	runtime	run#	runtime
background	371	15:49 h	371	15:49 h
^{137}Cs	370	02:00 h	369	02:00 h
(^{133}Ba)	373	02:00 h	372	02:00 h
^{60}Co	375	19:10 h	374	17:52 h
^{54}Mn	386	03:53 h	385	04:10 h

Table 3.3: Runs for energy calibration

The energy spectrum of the background run is subtracted from the spectrum of the source run. The resulting background corrected spectrum shows the energy distribution of the measured source. The spectrum is characterized by the Compton effect. The Compton edge in the energy spectrum is reached, when maximal energy is transferred. Because of the low energy resolution, a weighted mean energy is used for the calibration, quoted in table 3.2.

Identifying the position of the bin of the Compton edge has been difficult, because of the width of the edge. A procedure was applied, which identifies the Compton edge in the QDC bin with 2/3 counts of the bin in the spectrum with the maximum amount of counts [Zeg00]. Probably, it can also be argued, to use $\frac{3}{4}$, or any other ratio, since the slope is is influenced by the properties of the scintillator. As long as it is worked uniformly with all data, this technique should be fine. Different procedures were tried to find the bin with 2/3 of maximum counts.

1. Fitting the falling slope and then use the fit function to get the bin number and error.

2. Read the bin number „by hand“ and estimate a reasonable error.

Both procedures worked out, but since the statistics of the experimental data were quite good, the second procedure was used to do the actual energy calibration. The background corrected energy spectra of the different sources can be found in appendix 5.2.

	according energy	QDC bin Compton edge	
source	[keV]	box I	box II
^{137}Cs	622	860 ± 8	809 ± 20
^{60}Co	835	980 ± 13	913 ± 13
^{54}Mn	1253	1221 ± 8	1054 ± 8

Table 3.4: Scintillator energy calibration: γ energy and located Compton edge bin.

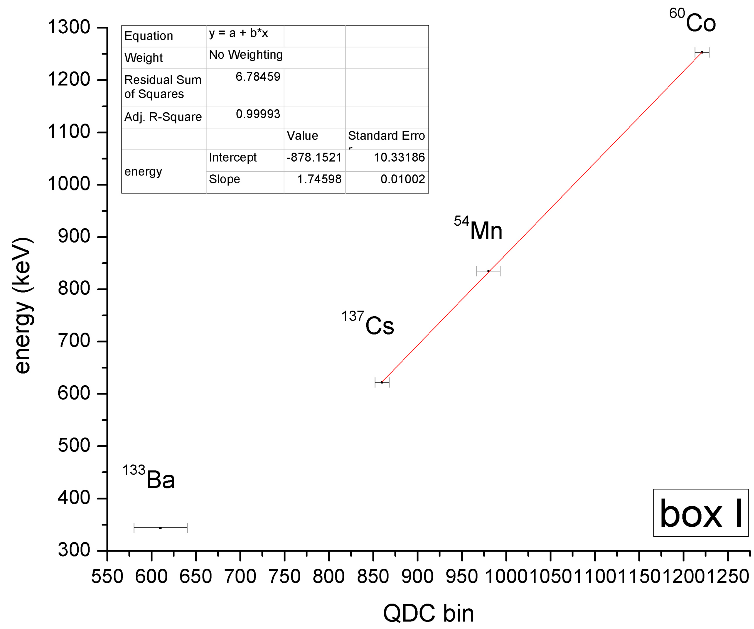

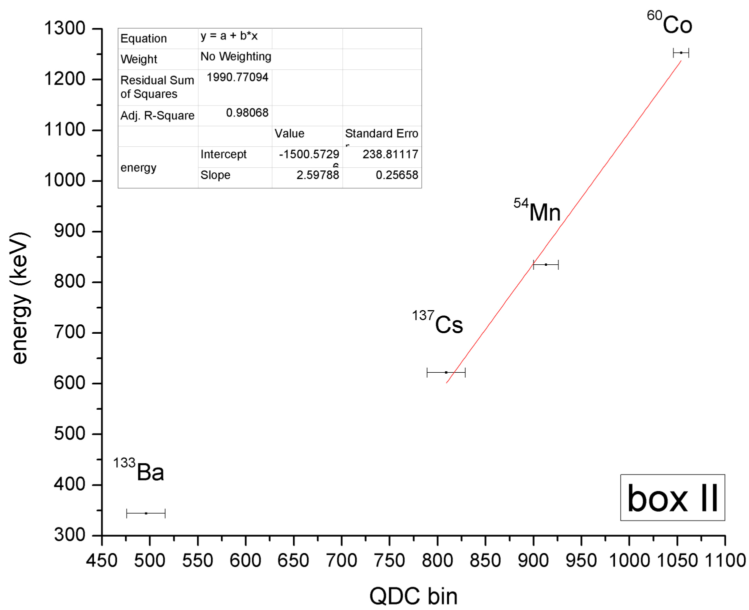

Figure 3.20: Energy calibration fits for the scintillator I in box I (top) and the scintillator II in box II (bottom). Because of the bad statistic of the ^{133}Ba data, it is not considered for the energy calibration.

The energy calibration will provide information about the energies of cosmic radiation. The data were fitted by a linear function. The energy-QDC bin relation is given by:

box I:

$$E_{box\,I} = -878.15\,keV + 1.75\,\frac{keV}{bin} \cdot [QDC\,bin]$$

$$\Delta E_{box\,I} = \sqrt{(10.33\,keV)^2 + (0.01\,\frac{keV}{bin} \cdot [QDC\,bin])^2}$$

box II:

$$E_{box\,II} = -1500.57\,keV + 2.60\,\frac{keV}{bin} \cdot [QDC\,bin]$$

$$\Delta E_{box\,II} = \sqrt{(238.81\,keV)^2 + (0.26\,\frac{keV}{bin} \cdot [QDC\,bin])^2}$$

The energy calibration shows, that an accurate energy measurement with this setup is not possible and can therefore not be recommended. In addition to the statistical error, a large systematic error of about 300 bins in the identification of the Compton edge is caused by the 2/3 method. The slope does not change too much, but the offset is affected significantly. This might explain the huge offset and the resulting „negative energies“ for low QDC bin numbers. Of course negative energies are not physical. The linearity of the QDC is shown in sub chapter 3.3, but the offset cannot be explained. The properties of the scintillator, the light guide and the photomultiplier have not been analyzed. Therefore it is not possible to make a statement about unlinearity or inhomogeneity in light propagation or light output of the system. Since the energy calibration is not satisfying, the following spectra remain in QDC-bin scale. Energies of peaks are estimated with the fit functions, but it is always highlighted, that the values can only provide a relative hint and no absolute energies.

The background energy spectra of each box and the coincidence spectra are shown in figure 5.5 in the appendix.

3.6 Tests of the active cosmic ray shield (CRS)

The easiest way to test the idea of the active cosmic ray shield for NERO is to use different hardware setups and check, if the (neutron) background of NERO can be reduced. The NERO background was estimated with scalers, and also the following tests were analyzed mainly with scaler data. In addition to the scaler information of each proportional counter, the rate of NERO Master Gate, NERO Master Gate Live (see electronic diagram figure 5.6) and CRS hardware coincidences were monitored. The coincidence signal was produced by a hardware AND logic. The CFD signals from PMTs are set to different widths, so the produced AND signal has a defined width. The screen shots of the scope in figure 3.21 show the CFD signals from box I (bottom box) in yellow and box II (top box) in blue. The width is set to 100ns (CFD I / box I) and 180ns (CFD II / box II).

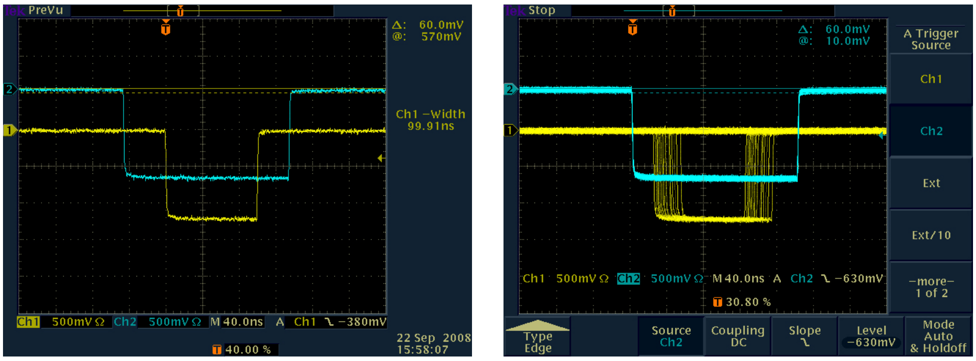

Figure 3.21: Coincidences of NIM signals from CFD I (left) and CFD II (right).

The CFD I signal is delayed for about 40ns to ensure, that in case of coincidences the short CFD I signal is included in the CFD II signal. With this, the logic AND produces signals with a defined width of 100ns (like CFD I). A Gate&Delay generator uses the logic hardware AND of both signals to produce a 200µs gate, which is routed to the NERO MG live AND (see electronic diagram figure 5.6) to produce the Master Gate live. The NERO Master Gate live is blocked for 200µs after a coincidence in the paddles, so that events in NERO within this time slot are neglected. Figure 3.22 shows the situation of the active cosmic ray shield veto signal (yellow) and NERO events (blue) within the veto gate. The NERO event depicted in figure 3.22 is suppressed by the active cosmic ray shield veto.

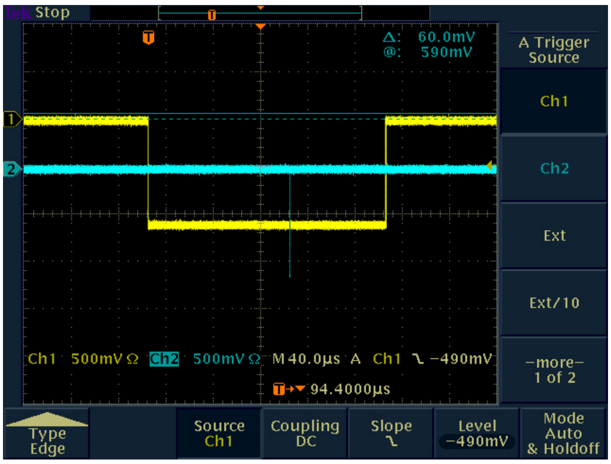

Figure 3.22: Veto gate (yellow, 200µs), produced by G&D generator with CRS coincidences as input and NERO events (blue).

The width of the veto gate is geared to the moderation time of the neutron detector. Assuming that neutrons and charged particles / γs reach the system in coincidence, the length of the veto would be a filter for neutron energies. Neutrons with higher energies need more time and volume to be moderated. The efficiency of NERO drops for neutron energies $> 3MeV$ (see figure 2.5). It is assumed, that the neutron background in NERO is mainly caused by neutrons with energies up to 3 MeV, because NERO is most efficient to neutrons with those energies. Cross sections of high energy neutrons decrease and they probably just pass NERO without any interaction. Considering those effects and the attempt to minimize the dead time of NERO caused by the active cosmic ray shield, support the idea to use a veto gate width similar to the moderation time (see sub chapter 2.7).

Three setups are used to test the idea of the active cosmic ray shield for neutron suppression in NERO.

1. NERO in standalone mode (see sub chapter 2.1.2). No veto by the active cosmic ray shield.

2. NERO in experimental mode (see sub chapter 2.1.2). Coincidences in the scintillators are used to trigger the NERO electronics. The TDC start gate is provided by coincidences in both scintillators, and NERO events are recorded as stop signals.

3. NERO in standalone mode (see sub chapter 2.1.2), but with a hardware veto by the active cosmic ray shield. The actual idea is realized by blocking the NERO Master Gate Live with a Gate & Delay Generator set with a logic AND for coincidences in the scintillators.

The interpretation of the data in test 1 and 3 is similar to the background runs in sub chapter 2.5 - Background NERO. Test 2 is different, because the setup and the readout are changed to experimental mode. The NERO energy information of the different tubes is not provided any longer, because the NERO ADCs are triggered by cosmic coincidences. Basically, the NERO ADCs are only used in standalone mode for setting the CFD thresholds.

As mentioned before, rates of NERO Master Gate, NERO Master Gate Live and CRS coincidences are monitored by scalers. In order to compare the rates from different tests, rates were normalized to the according rate of the NERO Master Gate (OR). The NERO Master Gate (OR) is not affected by the NERO setup mode (experimental / standalone) or by the veto of the active cosmic ray shield.

1. *NERO in standalone mode (run417):* Test 1 will provide a reference measurement.

NERO Master Gate (OR)		NERO Master Gate Live		Integral (Sum TDC) (within200µs)		CRS coincidence	
rate $[\frac{1}{s}]$	Δrate $[\frac{1}{s}]$	rate $[\frac{1}{s}]$	Δrate $[\frac{1}{s}]$	rate $[\frac{1}{s}]$	Δrate $[\frac{1}{s}]$	rate $[\frac{1}{s}]$	Δrate $[\frac{1}{s}]$
7.80	0.01	7.05	0.01	7.43	1.21	45.45	0.02
normalized count rate in %							
100%	0.18%	90.39%	0.17%	95.26%	15.51%	0.91%	<0.01%

Table 3.5: Test1 - run417: For a better comparison between all tests, all rates are normalized to the NERO MG rate. The CRS percent value quotes the possible dead time, if each coincidence blocks NERO for 200µs.

It is difficult to understand the numbers in table 3.5. The NERO Master Gate is the OR of all 60 CFD signals. Since electronics and mode of NERO do not affect the NERO CFDs, the NERO MG rates should be the same in all three tests. Because of fluctuations in between the different runs, all rates are given in percent to the NERO Master Gate rate. After that, relative rates (in percent) can be compared over all individual runs. In standalone mode, the integral over the sum of all TDC channels should give the same number as the NERO Master Gate scaler. The TDC records the delayed start signal (in TDC bin2) and additional events within 200µs. If no TDC start gate is pending, no stop signals can be recorded. This scenario might be possible after the end of 200µs, when the Master Gate Live is still blocked because of the data readout and no new TDC gate can be set. This effect might be an explanation for the missing 4.74% in the TDC rate. The sum of all spectra of TDC channels is characterized by the delayed start signal in TDC bin2 (=0.4µs delay). The sum of bin2 (bin with delayed start-signal events) in all TDC channels should agree with the NERO Master Gate Live, which is indeed true within the errors. The TDC sum spectrum of all channels is shown in figure 3.23.

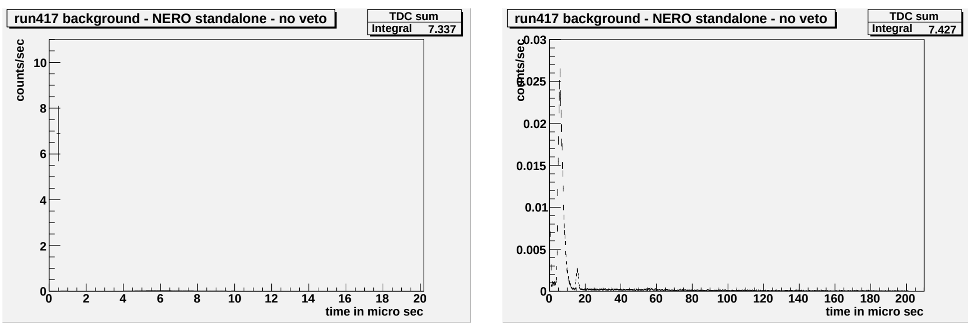

Figure 3.23: Test1 - run417: Sum of all TDC channels. Time range $[0, 20\mu s]$ shows self-trigger bin(left). Time range right is $[0, 200\mu s]$.

The integral values in the TDC time ranges of figure 3.23 are given in the small insert in the upper right of the histograms. Comparing figure 3.23 (left) and (right) highlights, that most of the stops are produced by the delayed start signal. Both histograms show the same data, in different time slots. Additional structure can be observed in the scale of the right spectrum. The maximum of the first peak is at 6µs and the maximum of the second, smaller peak is at 15.8µs. Further investigations are necessary to explain those structures. Neither electronic noise correlated to the start signal, nor a physical reason can be ruled out or established. In any case, the effect is pretty small compared to the number of self-trigger events. The cosmic coincidences do not affect the electronics in test 1. The hardware coincidences of the scintillators are monitored by a scaler. The percent value in table 3.5 shows the theoretical dead time of NERO in %, if each coincidence would block the detector for 200µs.

2. *NERO in Experimental Mode (run412):* The second test is the most interesting one, because it can provide a lot of information about the coincidences of neutrons and charged particles / γs in cosmic showers. Similar to the moderation time measurement, it would be possible to observe a distribution of moderation times, if neutrons are correlated to detected showers. Assuming, that neutrons reach the detector system in coincidence, we expect to record most of the neutrons within a small time window (comparable to the moderation time in sub chapter 2.7) after the coincidence in the scintillators of the active cosmic ray shield. One or multiple neutrons and a bunch of charged particles/γs pass the first scintillator. The ionizing particles are detected in the top scintillator. Some of the ionizing particles pass NERO and produce a second signal in the bottom scintillator. For such events a coincidence of the active cosmic ray shield is created. The neutrons are scattered in NERO and are moderated. The slowed down neutrons react in one of the gas tubes and are detected. Since the TDC gate width is set to 200µs, there is enough time to moderate neutrons, which have the right energy to be detected in NERO. Very high energetic neutrons would need more time and volume to be moderated, but are not detected and can not produce background, because of their low cross section. Unfortunately, test 2 does not support the mentioned scenario.

NERO Master Gate (OR)		NERO Master Gate Live		Sum TDC (within200µs)		CRS coincidence	
rate $[\frac{1}{s}]$	Δrate $[\frac{1}{s}]$	rate $[\frac{1}{s}]$	Δrate $[\frac{1}{s}]$	rate $[\frac{1}{s}]$	Δrate $[\frac{1}{s}]$	rate $[\frac{1}{s}]$	Δrate $[\frac{1}{s}]$
8.73	0.01	0.11	<0.01	0.13	0.03	44.95	0.03
normalized count rate in %							
100%	0.16%	1.26%	0.11%	1.49%	0.34%	0.90%	<0.01%

Table 3.6: Test2 - run412: For better comparison between different tests, all rates are normalized to the NERO MG rate.

The relative TDC integral of all channels (see table 3.6) shows, that only 1.49±0.34% of all NERO background events are registered within 200µs after the detection of a cosmic shower. Because of the experimental mode of NERO, the TDC is sensitive for 44.95·200µ$s = 8.99ms$ per second, which corresponds to $0.90 \pm 0.001\%$ active time. Comparing the relative active time of NERO to the relative rate of the detected events within the active time, makes clear that no distinct correlation between cosmic showers and neutron background in NERO can be observed. If there is a correlation, only very few neutrons come in coincidence with the detected showers. Maybe several neutrons are induced very close to the detector and those are correlated, but the major part of the neutron background is not correlated to the coincidences of the active cosmic ray shield.

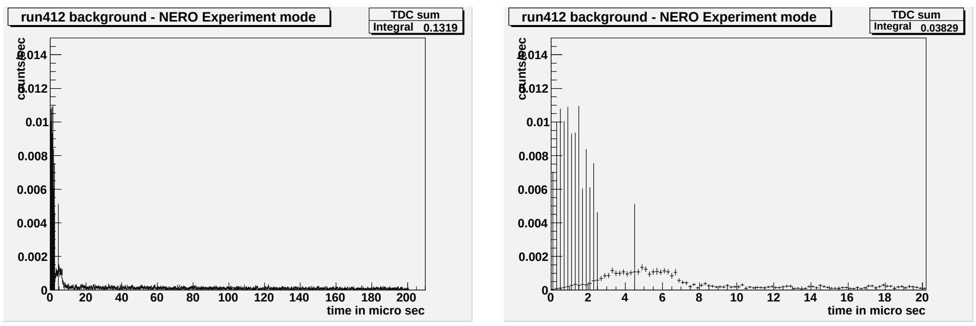

Figure 3.24: Test2 - run412: Sum of all TDC channels. Data of run412 in different scales.

The histogram of the sum of all TDC channels in figure 3.24 has to be analyzed. Up to 2.5µs, the error bars confuse and the actual data is not noticeable. The right histogram in figure 3.24 is zoomed in and shows a small peak. This peak is the only structure in the whole spectrum and might be the small part of shower-correlated neutron events. The integral over the peak [2µs, 8µs] is $0.0257 \pm 0.0134 \frac{events}{sec}$. This corresponds to 0.29±0.15% of all background neutrons. This small amount and the additional fact, that the small peaks in test 1 cannot be explained, lead to the conclusion of test 2, that no reasonable correlation of neutrons and cosmic showers can be found within a time window of 200µs after the detected cosmic showers. It is also questionable, whether neutrons are moderated within $2-8$µs in NERO - only very low energy neutrons would be detected in such a short time. If low energy neutrons are detected, they must be induced very close to or inside of the detector.

3. *NERO in standalone mode, but with veto by the active cosmic ray shield (run420):* The third test uses the scintillator coincidences to block the NERO Master Gate Live for a time period of 200µs. The actual idea of the active cosmic ray shield is realized with a hardware veto.

NERO Master Gate (OR)		NERO Master Gate Live		Sum TDC (within200µs)		CRS coincidence	
rate $[\frac{1}{s}]$	Δrate $[\frac{1}{s}]$	rate $[\frac{1}{s}]$	Δrate $[\frac{1}{s}]$	rate $[\frac{1}{s}]$	Δrate $[\frac{1}{s}]$	rate $[\frac{1}{s}]$	Δrate $[\frac{1}{s}]$
9.37	0.01	8.52	0.01	8.83	2.08	45.45	0.03
normalized count rate in %							
100%	0.15%	90.93%	0.14%	94.24%	22.20%	0.91%	<0.01%

Table 3.7: Test3 - run420: For better comparison between different tests, all rates are normalized to the NERO MG rate.

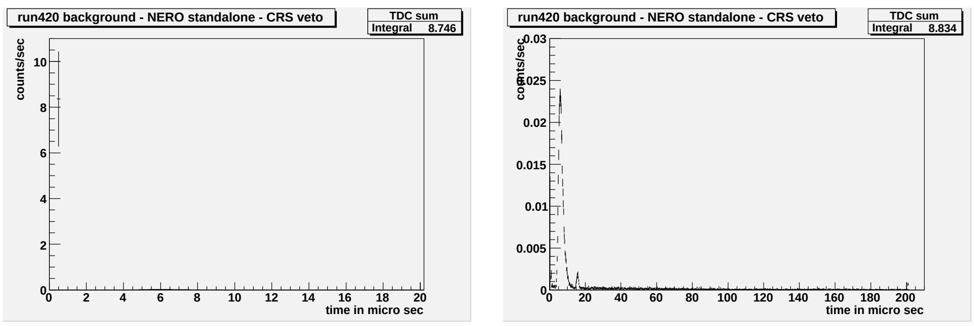

Figure 3.25: Test3 - run420 sum of all TDC channels

The rate of the NERO Master Gate Live should be reduced by the veto gate of the scintillators coincidences, if neutrons are correlated to coincidences. Basically, the veto does not affect the background rate, but produces dead time. Test 2 and test 3 agree with each other. Since the electronic setups are different but the results agree, it can be concluded, that the neutrons are not correlated to the cosmic showers, which are detected with the scintillators of the active cosmic ray shield. The maxima of the structures in the sum spectrum of the TDC channels are located at the same positions as in test 1 (6µs and 15.8µs). The self-trigger bin2 contains most of the neutron events in the TDC sum spectrum ($8.36 \pm 2.08\ \frac{1}{s}$).

Test 1 and test 3 are compared directly.

	test 1 - run417 - no veto		test 3 - run420 - CRS veto	
	rel. rate to MG	Δrel. rate to MG	rel. rate to MG	Δrel. rate to MG
Master Gate	100%	0.17%	100%	0.20%
Master Gate Live	90.48%	0.18%	90.96%	0.19%
Integral TDC sum	95.26%	15.51%	89.24%	22.20%
TDC self-trigger bin2 sum	88.33%	15.51%	89.24%	22.20%
CRS veto time	0.91%	<0.01%	0.91%	<0.01%

Table 3.8: Direct comparison of test 1 and test 2

The effect of the active cosmic ray shield should reduce the relative rate of Master Gate Live, Integral TDC sum and TDC self-trigger bin2 sufficiently. However, no significant changes can be observed. Most of the figures do not change within the errors. A weak effect can be observed but is also not crucial. The error in the TDC self-trigger bin2 highlights, that the error in the TDC sum Integral is dominated by the error of the self-trigger rate.

A logic relation between all three tests is given.

$$SumTDC(test2) + SumTDC(test3) = SumTDC(test1)$$

The relation is true within the large errors.

Additional tests without coincidences in the scintillators have been done. Only the top paddle signal is used instead of coincidences of both paddles.

Test 2b - NERO in Experimental Mode (run413): Only the CFD signal from the top paddle is used to start the TDC gate. Otherwise, the same setup is used like in test 2.

NERO Master		NERO Master		Sum TDC		CRS	
Gate (OR)		Gate Live		(within200µs)		top paddle	
rate $[\frac{1}{s}]$	Δrate $[\frac{1}{s}]$	rate $[\frac{1}{s}]$	Δrate $[\frac{1}{s}]$	rate $[\frac{1}{s}]$	Δrate $[\frac{1}{s}]$	rate $[\frac{1}{s}]$	Δrate $[\frac{1}{s}]$
8.61	0.02	0.71	<0.01	0.78	0.03	464.75	0.12
normalized count rate in %							
100%	0.33%	8.25%	0.12%	9.06%	0.12%	9.23%	<0.01%

Table 3.9: Test 2b - run413 - only scintillator in top position is used. For better comparability over all tests, all rates are transformed to a ratio to the NERO MG rate.

Because the coincidences in the scintillators are not necessary anymore to provide the TDC start gate, the active time of the neutron detector is much higher and more neutron stop signals are recorded. But still, no significant correlation can be observed, since the active time of 9.23% explains a TDC stop rate of 9.06% within the errors.

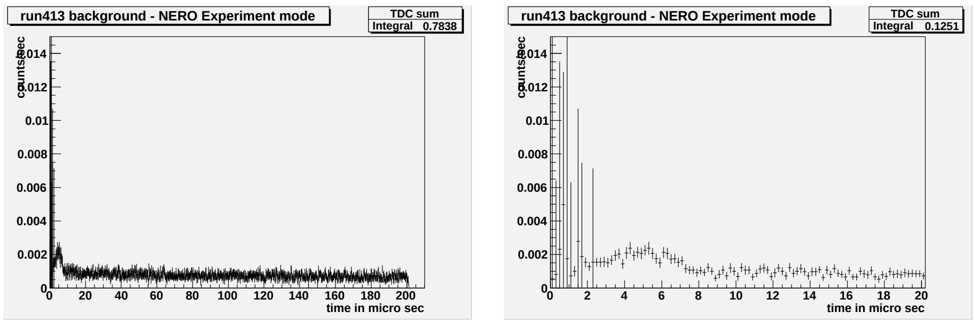

Figure 3.26: Test 2b - run413 - TDC sum spectra with different time ranges.

The TDC sum spectra in figure 3.26 show the constant neutron background within 200µs after the start signal from the top scintillator. The small peak at [2µs, 8µs] is at the same position as observed in test 2 where coincidences of both paddles were used. The large error bars are confusing, but the rates are quite low.

Test 3b - NERO in standalone mode, veto by top paddle (run414): Only the CFD signal from the top paddle is used to block the Master Gate Live for 200µs. Otherwise, the same setup is used like in test 3.

NERO Master Gate (OR)		NERO Master Gate Live		Sum TDC (within200µs)		CRS top paddle	
rate $[\frac{1}{s}]$	Δrate $[\frac{1}{s}]$	rate $[\frac{1}{s}]$	Δrate $[\frac{1}{s}]$	rate $[\frac{1}{s}]$	Δrate $[\frac{1}{s}]$	rate $[\frac{1}{s}]$	Δrate $[\frac{1}{s}]$
8.82	0.01	7.20	0.01	7.55	1.07	470.61	0.10
normalized count rate in %							
100%	0.16%	81.63%	0.15%	85.60%	0.14%	9.41%	<0.01%

Table 3.10: Test 3b - run414 - Only top paddle is used for veto signal. No coincidence of top and bottom scintillator are necessary for a veto signal.

The veto reduces the neutron background for about 8.4% (comparing TDC sum integral between test 3b and test 1), but this value is still within the errors of both relative rates. Neglecting the statistical uncertainty, this 8.4% background suppression is obtained at the expense of 9.41% dead time, where the neutron detector is blocked by the veto gate.

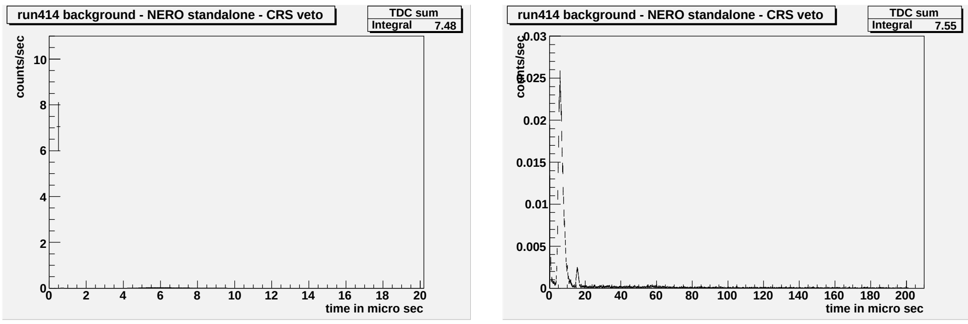

Figure 3.27: Test3b - run414 - TDC sum spectrum

The self-trigger bin in the sum spectrum of all TDC channels still dominates the rate and the error. Figure 3.27 (right) shows the same structure like in the previous runs. The positions of the peaks are the same at 6µs and 15.8µs.

Conclusion of all tests:

No significant effect to the neutron background in NERO has been observed when using the active cosmic ray shield. No coincidences of neutrons and detected showers could be observed. The left histogram of figure 3.26 shows the constant neutron background after a detected particle in the top paddle.

The explanation of the non-correlation of neutrons and ionizing particles of cosmic showers might be due to different runtimes in the atmosphere and the different lateral propagation. Neutrons which are induced by cosmic showers close to or in NERO might be correlated, but if a neutron is induced in a height of 20km, the correlation at ground level might be lost because of different reactions and runtimes. Neutrons can be induced in all materials in the room, the walls and the ceiling or the floor. Because of the trajectories of those neutrons and their runtime until they reach the detector vary, the correlation to the detected shower is not given, anymore.

Chapter 4

Conclusion and Outlook

4.1 NERO and active cosmic ray shield

- The Neutron Emission Ratio Observer has been completed in its missing electronics and biased after a period, where it has not been used. After this work, NERO is in a state where it can be used for the next experiments. Background and efficiency have been monitored and different attempts were performed to improve NERO's properties. In order to lower the background of the detector system, the preamplifier box A should be checked again, since the event rate for quad A is almost as high as the sum of events in quad B, C and D (see sub chapter 2.5). The additional events in quad A seem to be no neutrons, but electronic noise. The background in quad B, C and D is mainly caused by neutrons.

- An active cosmic ray shield has been assembled of two scintillators ($1 \cdot 1m^2$). Light-tight wooden boxes have been designed and manufactured, which protect and provide support structure to the detectors. Two working scintillators with electronics do exist now, which can easily be used as an active cosmic ray shield for experiments. The failure of the active cosmic ray shield for NERO is due to the fact, that neutrons are not significantly correlated to the detected showers of charged particles - *not*, because the scintillators do not detect the ionizing particles of a shower. The use of the active cosmic ray shield for NERO might be useful in experiments with very low event rates.

- Passive shielding of NERO against neutrons should be considered. As described in sub chapter 1.5, two component moderation/absorption materials can be used to slow down neutrons and capture them. Maybe, the experiment can be done in an experimental vault with additional shielding by the building like thicker ceilings. The advantage of passive shielding is, that no dead time in the detector system is created.

4.2 Future experiments with NERO

In 2006, an experiment has been proposed to GSI by Fernando Montes et al. [Mon06]. The experiment is expected to provide data of β half-lives and P_n values of the very neutron rich nuclei ^{125}Ag – ^{129}Ag (re-measurement), ^{124}Pd – ^{128}Pd, ^{121}Rh – ^{125}Rh . Results of this experiment may show further evidence for the strength of shell closure of magic $N = 82$. A ^{238}U beam will hit a lead target and produce a secondary ^{132}Sn beam. The secondary beam will be focused on a beryllium target where the next interaction will provide the neutron rich nuclei. The experimental setup will be similar to Paul Hosmer's experiment in 2002 [Hos05-1]. The nuclei will be slowed down and implanted in a stack of silicon detectors, where time of implantation is recorded. The following β decay will be detected and correlated with the implementation. The β decay triggers a time window of acceptance in a neutron detector for the possibly β- delayed neutron emission. In order to avoid multiple implementations, an implementation rate of $10\frac{1}{s}$ will be used.

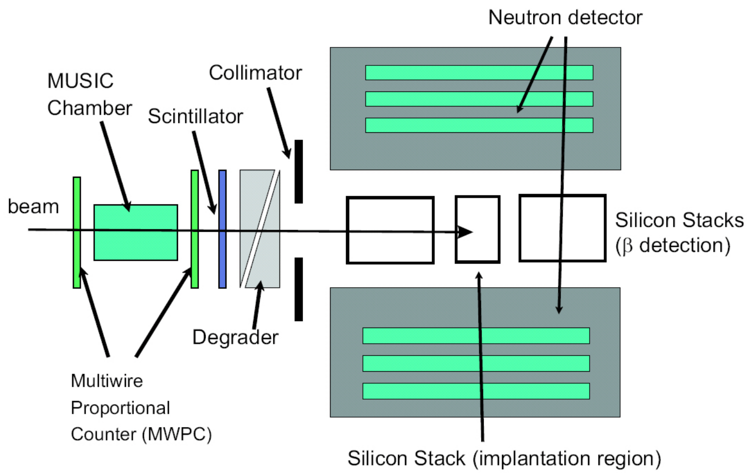

Figure 4.1: Experimental setup for the proposed experiment at GSI. [Mon06]

4.3 Acknowledgments

I especially would like to thank Prof. K.-L. Kratz, Prof. K. Wendt, Prof. H. Schatz and Ph.D. Fernando Montes - my supervisors and advisers at Johannes Gutenberg Universität Mainz and National Superconducting Cyclotron Laboratory. The mentoring was very good, and I never found closed doors, when I had a problem. Also Giuseppe Lorusso should be mentioned, who showed me how to work with NERO at the beginning of my work.

I want to thank all members of the NSCL Nuclear Astrophysics Group for making me feel welcome in the group and at the NSCL.

I would like to thank the NSCL and all its staff and faculties; explicitly John Yurkon in the detector lab and the machine shop staff.

I would like to thank my friends at Michigan State University for the nice time besides physics. Regular happy hours, BBQs and bicycle tours have been highlights for my stay in East Lansing and I will keep all the nice experiences in mind.

Thanks to Christoph Caesar for sharing the apartment and my/our first "own" car.

Thanks to my friends and my family in Germany for supporting me.

Chapter 5

Appendix

5.1 HV characteristic

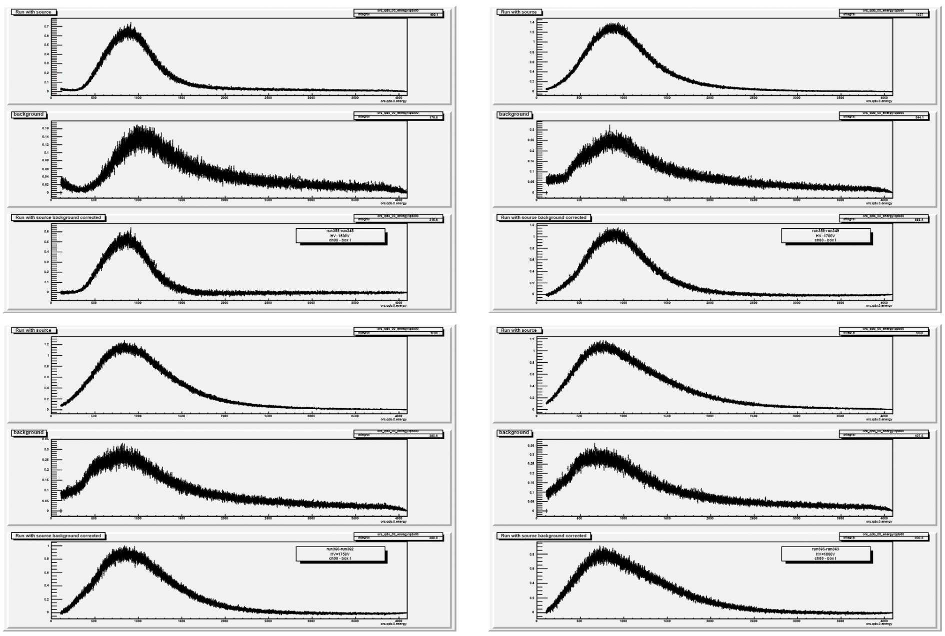

Figure 5.1: HV- characteristic box I: (top left) - 1500V, (top right) - 1700V, (bottom left) - 1750V, (bottom right) 1800V

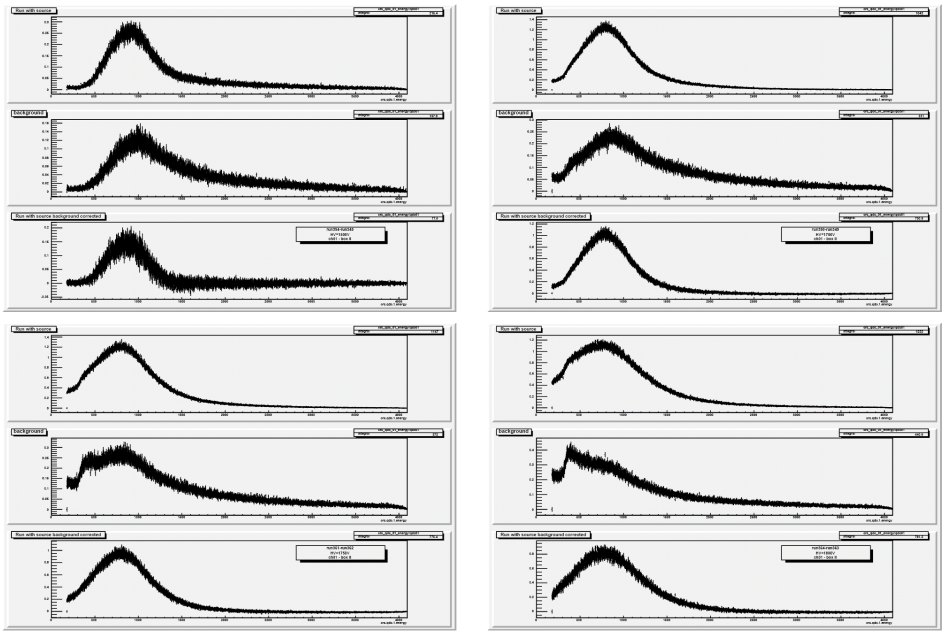

Figure 5.2: HV- characteristic box II: (top left) - 1500V, (top right) - 1700V, (bottom left) - 1750V, (bottom right) 1800V

5.2 Scintillator energy calibration

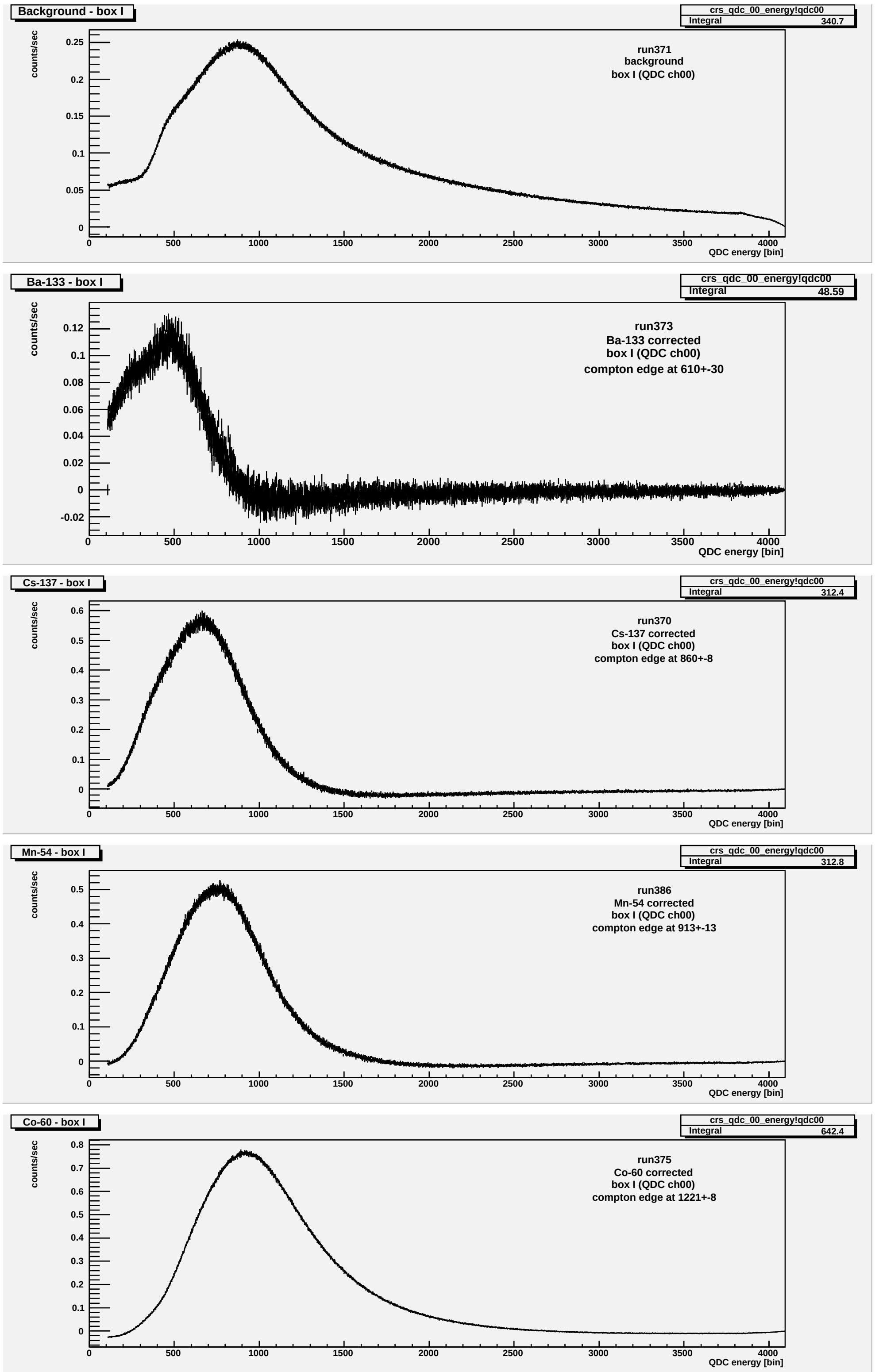

Figure 5.3: Energy calibration box I

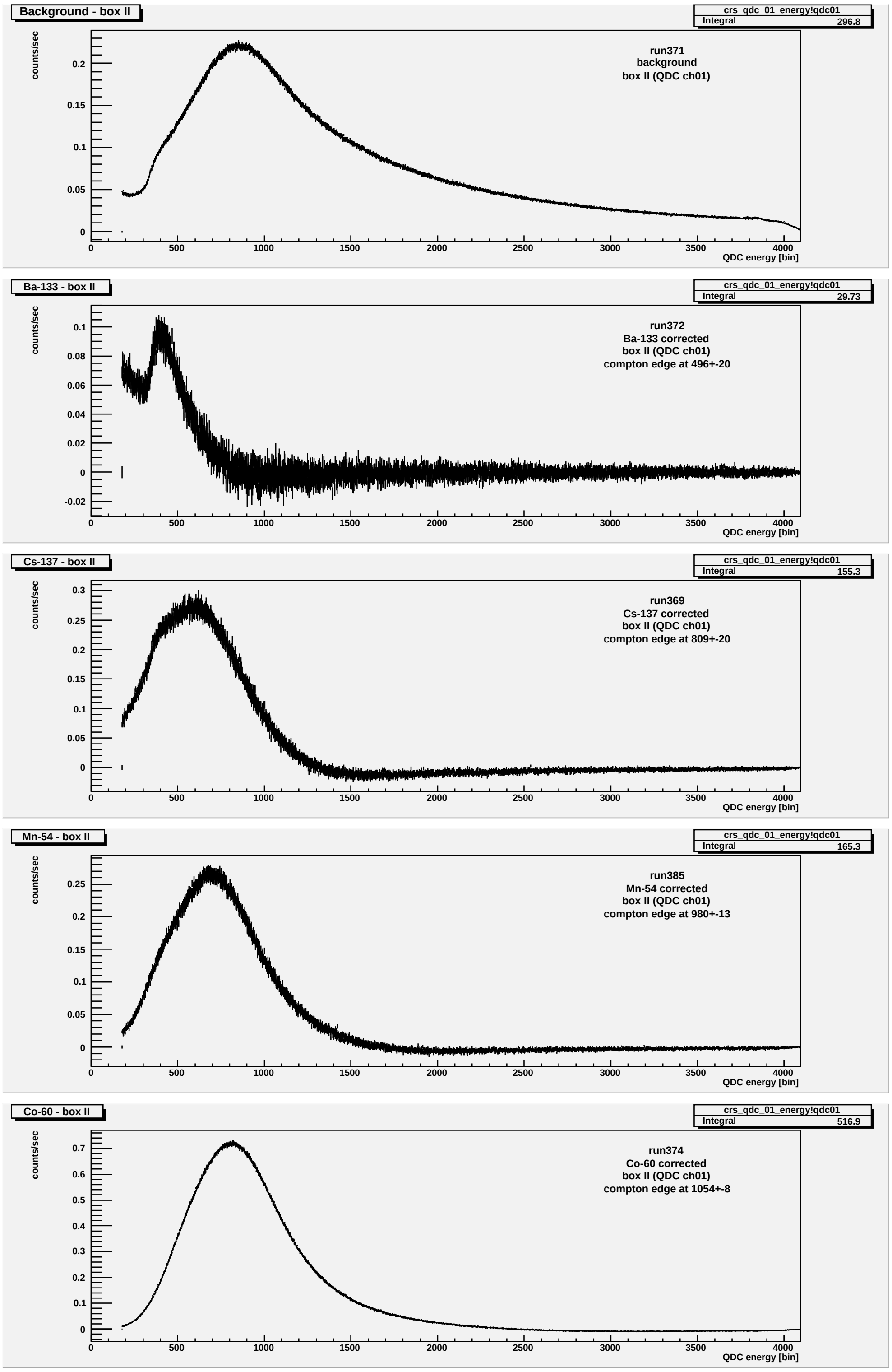

Figure 5.4: Energy calibration box II

5.3 Energy spectra of cosmic rays

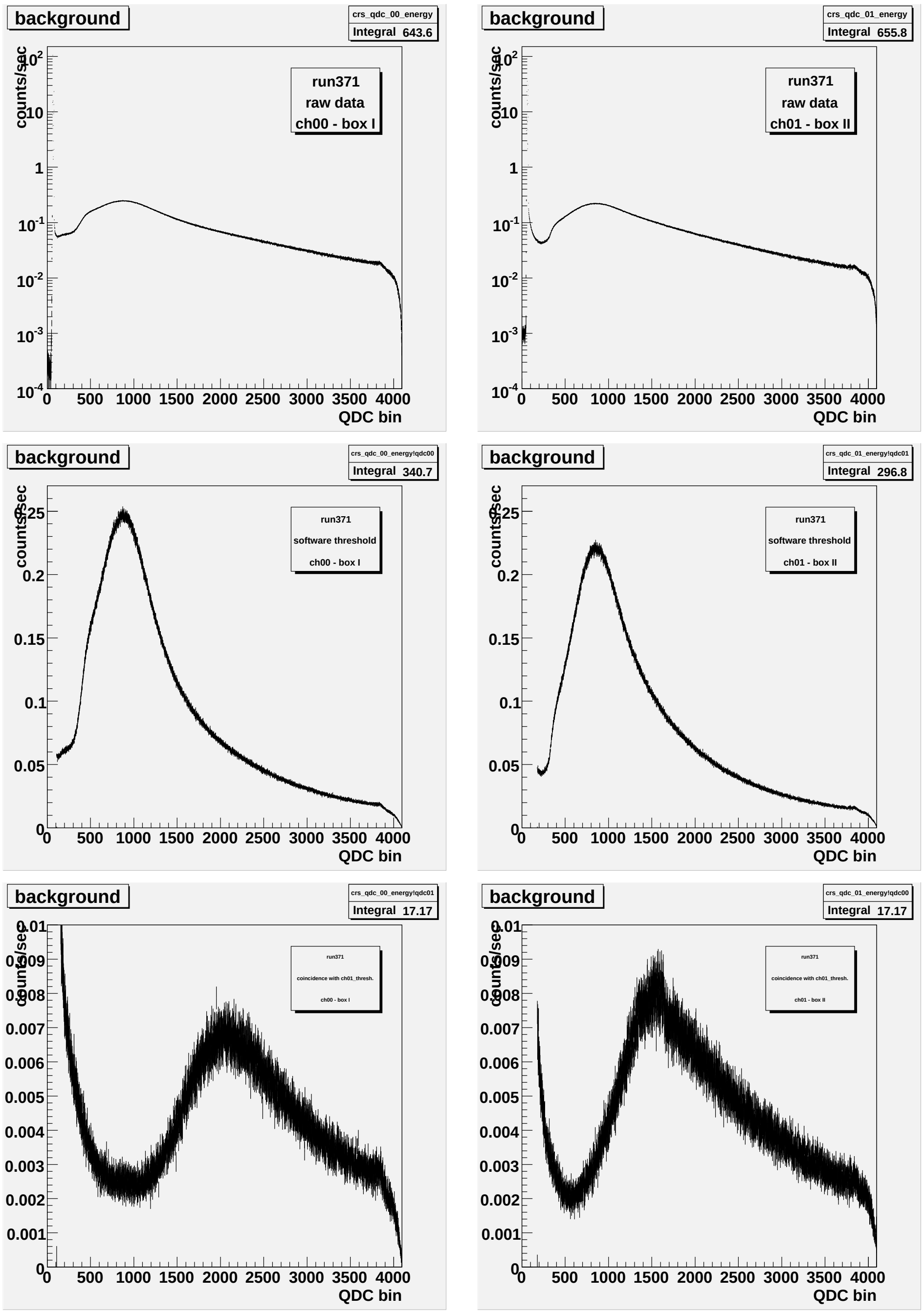

Figure 5.5: Energy spectra of box I (left column) and box II (right column). Histograms in the first row display the raw spectra. Because of the trigger, there is a huge peak for low energy below CFD threshold. In the energy spectra of the second row, the low energy peak is cut by software and the axis are linear. The last row displays the energy spectrum from row 2 gated on events in the other channel. Coincidences of events with energies above software threshold are displayed. The peaks of the spectra in the last row are higher than the background peaks of the spectra in the second row. This shows, that coincidence events have energies in MeV range.

5.4 Electronic diagram

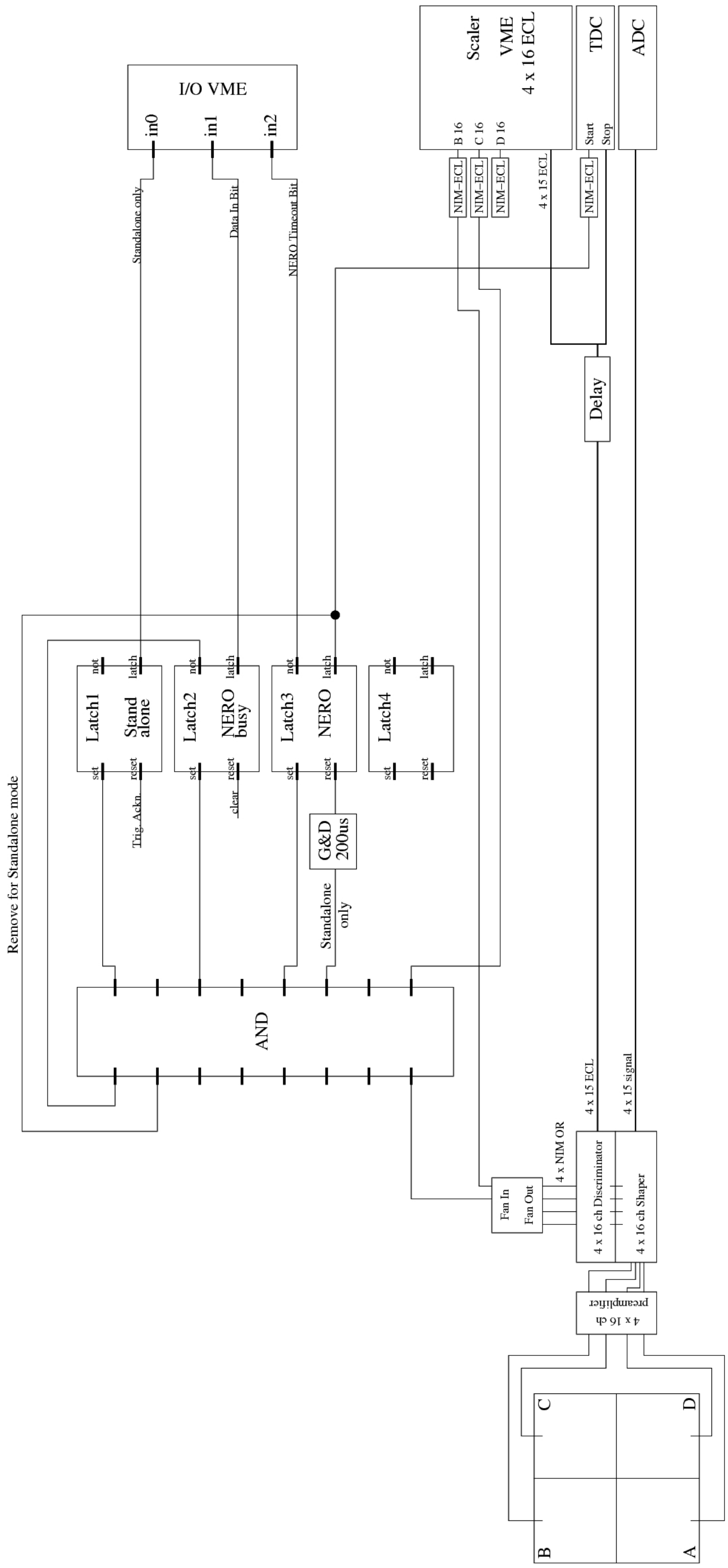

Figure 5.6: NERO electronic diagram: standalone mode

Bibliography

[Ahm03] I. Ahmada et al., Nucl. Instr. and Meth. A505 389-392, "Quantitative determination of Cf-252" (2003)

[Arn03] M. Arnould et al., "The p-process of stellar nucleosynthesis: Astrophysics and nuclear physics status"

[Asp05] Asplund et al. (2005)

[Atn08] Figure: http://outreach.atnf.csiro.au/education/senior/ (2008)

[Bah03] J.N. Bahcall et al., Phys. Rev. 90 (2003)

[Bau01] Thomas Baumann, "Neutron detection & spectroscopy: Minicourse on experimental techniques at the NSCL" (2001)

[Bay08] GE Bayer Silicones - Product information of RTV615

[Blu08] NSCL bluebook, http://docs.nscl.msu.edu/daq/bluebook/html/

[Buf08] NSCL bufdump, http://docs.nscl.msu.edu/daq/bufdump/index.html

[Bur57] E.M. Burbidge, G.R. Burbidge, W.A. Fowler, F. Hoyle, Rev. Mod. Phys. Vol. 29(4) (1957)

[Cae08] C.A.E.N. ADC Mod. V785 user manual

[Cae08-1] C.A.E.N. TDC Mod V767a user manual

[Cae08-2] C.A.E.N. QDC V792 user manual

[Che89] Cherubini et al., Nucl. Instr. and Meth. A281 349-352 , "Gamma calibration of organic scintillators" (1989)

[Cow91] J.J. Cowan et al., Phys. Rep. 208,267-394 (1991)

[Gal98] R. Gallino, C. Arlandini, M. Busso, The Astrophysical Journal 497:388–403 (1998)

[Gru00] C. Grupen, "Astroteilchenphysik: Das Universum im Licht der kosmischen Strahlung" (2000)

[Gsi08] Figure: http://www.gsi.de/fair/overview/research/ (2008)

[Ham08] Hamamatsu, “Photomultiplier handbook - basics and applications”

[Hos05] P. Hosmer, Ph.D. Thesis, “beta-decay studies of ^{78}Ni and other neutron-rich nuclei in the astrophysical r-process” (2005)

[Hos05-1] P.T. Hosmer et. al., PRL 94, 0112501, “Half-Life of the Double Magic r-Process Nucleus ^{78}Ni” (2005)

[Hoy53] F. Hoyle, Astophys. J. Suppl, 1 121 (1954)

[Kee57] G.R. Keepin et al. , Phys. Rev. 107, 01044 (1957)

[Kch08] Institut für Kernchemie, Johannes Gutenberg Universität Mainz, Germany

[Kno00] G.F. Knoll, “Radiation Detection and Measurement” (2000)

[Kra79] K.-L. Kratz, Review of Delayed Neutron Energy Spectra, IAEA Vienna, INDC(NDS)-107/G+Sp (1979) p.103

[Kra82] K.-L. Kratz et al. Z. Phys. A - Atomic and Nuclei 306,0 239-257 (1982)

[Kra84] Kratz K.-L. Nucl.Phys. A417, 447 (1984)

[Kap89] F. Käppeler et al. , Rep. Prog. Phys. 52 945-1013 , “s-process nucleosynthesis-nuclear physics and the classical model” (1989)

[Kra93] K.-L. Kratz, et al., Ap.J.403,216-238 (1993)

[Kra06] K.-L. Kratz, “Einführung in die Astrophysik” (lecture) (2006)

[Lan03] K. Langanke and G. Martinez-Pinedo, Rev. Mod. Phys. Vol. 75 819-862 „Nuclear weak-interaction processes in stars“ (2003)

[Lor08] Giuseppe Lorusso, NSCL

[Mar99] R. C. Martin, J. B. Knauer, and P. A. Balo, “Production, Distribution, and Applications of Californium-252 Neutron Sources” (1999)

[Mon05] F. Montes, Ph.D. Thesis, “Beta decay studies in neutron rich Tc, Ru, Rh and Pd isotopes and the weak r-process“ (2005)

[Mon06] F. Montes et al., proposal, “β-decay of very neutron-rich Rh, Pd, Ag nuclei including the r-process waiting point 128Pd” (2006)

[Ner60] W.E. Nervik, Phys. Rev. Vol. 119(5), “Spontaneous Fission Yields of Cf-252” (1960)

[Nsc08] NSCL website www.nscl.msu.edu

[Nsc08-1] NSCL hardware control: http://docs.nscl.msu.edu/daq/modules/alldoxy/

[NSC08-2] NSCL hardware tag, http://groups.nscl.msu.edu/userinfo/daq/nscltags.html

[Ohm87] H. Ohm et al., Nucl. Instr. Meth. A257,076 (1987)

[Peu85] P. Peuser et al., Nucl. Instr. and Meth. A239 529-535, (1985)

[Pfe01] B. Pfeiffer, K.-L. Kratz, “Status of delayed-neutron precursor data: half-lives and neutron emission probabilities” (2001)

[Pic08] Pico Systems, Shaper/Discriminator, http://pico-systems.com/shapdisc.html

[Rei08] C.W. Reich, W Mannhart, T Englad., evaluation Cf-252 http://t2.lanl.gov/cgi-bin/decay?200,9861 (1990)

[Rol88] C. E. Rolfs and W. S. Rodney, “Cauldrons in the Cosmos” (1988)

[Roo08] CERN, root, http://root.cern.ch/root/Mission.html

[Roo08-1] root tutorials: http://www.slac.stanford.edu/BFROOT

[Sal99] E.E Salpeter, Rev. Mod. Phys. 71, “Stellar Nucleosynthesis” (1999)

[Sch98] H. Schatz et al. , Phys. Rep. Vol. 294(4), 167-263 (1998)

[Sch03] Ralf Schuh, “Höhenstrahlung - Ein neues Experiment im Physikalischen Praktikum für Fortgeschreittene an der TU Darmstadt” (2003)

[Sis08] SIS 3820 VME scaler user manual

[Sne08] C. Sneden, J.J. Cowan, R. Gallino Annu. Rev. Astrophys. 46:241-88 (2008)

[Sol08] Figure: http://www.solstation.com/x-objects/xte-bh.htm (2008)

[Spe08] SpecTcl, http://docs.nscl.msu.edu/daq/spectcl/

[Tay66] R. J. Tayler, Origin of the Elements (1966)

[Val99] T. E. Valentine, US DOE evaluation, “Evaluation of prompt fission gamma rays for use in simulating nuclear safeguard measurements” (1999)

[Wei04] A. Weiss, “Nukleosynthese” (2004)

[Woo94] S.E. Woosley et al., Ap.J. 433,229-246, (1994)

[Zeg00] R. Zegers, Ph.D. Thesis, „Search for isovector giant monopole resonances“